Analysis and assessment of uncertainties in coastal morphodynamic modelling

Dissertation

in fulfilment of the requirements for the doctor's degree

of the Faculty of Mathematics and Natural Sciences

at Kiel University

Guilherme Luiz Dalledonne

Kiel, 2017

First referee: Prof. Dr. Roberto Mayerle
Second referee: Prof. Dr. Gerd Bruss

Date of the oral examination: 21.07.2017
Approved for publication: 21.07.2017

Signed: Prof. Dr. Natascha Oppelt, Dean

No man ever steps in the same river twice.
HERACLITUS

Acknowledgements

After walking the path, one realizes the true obstacles and challenges that lie in it. This is probably true for every experience in life and it definitely holds true for mine during my doctorate. Actually, for me crossing the finish line was as important as learning the lessons along the way. Fortunately, along my path I had the pleasure of having people by my side that gave me strength to keep going.

During my academic life in Kiel, the first person I need to thank is Prof. Mayerle. He made possible for me to come to Germany and start my doctoral studies, and for that I am very grateful. I would like to acknowledge the Research and Technology Centre West Coast (FTZ), University of Kiel, for providing the necessary funding and structure for my work.

My time as part of the Coastal Research Laboratory (CORELAB) team would not be the same without some dear colleagues, with whom I did not only share hard times dealing with models, field measurements and reports, but also good relaxing times doing barbecues and kayak tours, manufacturing and flying kites, or just enjoying the (short) summer in a *Biergarten*. Daniela, Fawaz, Gerd, Joaquim, José, Kadir, Katharina and Simon, Marcos, Natacha, Peter, Song and Xiang, thank you CORE-gang! A special thanks to Kalle, who has always been ready to help us and teach us hands-on lessons about the Wadden Sea, the German culture or simply to talk about some interesting topic.

After five years living in Kiel, I made some good friends that I would like to thank: Angela, Benedetta, Karlos and Debora, Dilshod and Edita, Franciane, Fernando, Guilherme, Jaime, Katja and Daniel, Maysa, Monique, Sara and many other great people.

Family is the side of the equation that balances the system as a whole.

Without them there would be no *thesis*.

Without them there would be no *will*.

Without them there would be no *sense*.

I would like to thank first my grandparents Clarice, Dirceu (in memoriam), Glacy and Reynaldo. With simplicity and kindness they have always shown me that books are not the only path to wisdom. I also thank my dear uncle, godfather and good friend Marcus, an example for me as engineer and person, with whom I can talk and ask about anything. Last but not least, I thank my parents and my brother. They have been by my side in every important moment of my life, pulling me out of difficult times and carrying me on their shoulders to celebrate my achievements. Celso, Márcia and Henrique, thank you for your unconditional love and support, always.

Abstract

During the last decades numerical models have become a powerful tool to investigate hydrodynamics and sediment dynamics. However, many key parameters and decisive numerical formulations of morphodynamic processes are bound to assumptions, estimations and uncertainties, which proceed to model results. The study aims to contribute to identify and take uncertainty of results in morphodynamic simulations into account. This is done by means of statistical analysis of key model parameters, and by the application of the *ensemble forecasting method*, based on Monte Carlo Simulations.

The procedure is developed and applied to simulate the morphodynamic processes in the tidal flats of the Dithmarschen Bight, North Sea, Germany. Focus is placed on the migration of a tidal channel system, a physical process still poorly clarified, over observation periods of two years. Based on available data and extensive measurements of bathymetric evolution, water level, current, wave and sediment concentration, process-based models for flow, waves, sediment transport and morphodynamics are developed.

Comparisons of bathymetric data with model results show that the model is capable to meet well the direction of the channel migration while the extent of migration is underestimated. Nevertheless, morphodynamic processes in tidal channels have been better resolved than those on tidal flats. Ranges of uncertainties are revealed. Analysis of model confidence showed that storm events have a significant relevance on morphodynamic results. Overall, the ensemble forecasting method proves to be a useful tool to account for uncertainties in morphodynamic modelling, to provide ranges of probability and, thus, increase the reliability of morphodynamic modelling results.

Zusammenfassung

In den letzten Jahrzehnten wurden numerische Modelle zu einem leistungsfähigen Werkzeug für die Untersuchung von Hydrodynamik und Sedimentdynamik. Allerdings sind viele Schlüsselparameter und entscheidende numerische Formulierungen von morphodynamischen Prozessen an Annahmen, Schätzungen und Unsicherheiten gebunden, die zu Modellresultaten weiterführen. Die Studie soll dazu beitragen, die Unsicherheit der Ergebnisse in morphodynamischen Simulationen zu identifizieren und zu berücksichtigen. Dies geschieht mittels statistischer Analyse von Schlüsselmodellparametern und durch die Anwendung der Ensemblevorhersagemethode auf Basis von Monte-Carlo-Simulationen.

Das Verfahren wird entwickelt und angewendet, um die morphodynamischen Prozesse in den Wattflächen der Dithmarschen Bucht, Nordsee, zu simulieren. Der Schwerpunkt liegt auf der Migration eines Priels - ein physikalischer Prozess, der noch wenig erklärt ist - über Beobachtungszeiträume von zwei Jahren. Basierend auf den verfügbaren Daten und umfangreichen Messungen der Bathymetrie-Entwicklung, des Wasserstands, von Strömung, Seegang und Sedimentkonzentration werden prozessbasierte Modelle für Strömung, Seegang, Sedimenttransport und Morphodynamik entwickelt.

Vergleiche von Bathymetrie-Daten mit Modellergebnissen zeigen, dass das Modell in der Lage ist, die Richtung der Prielmigration gut zu erreichen. Das Ausmaß der Migration wird dagegen unterschätzt. Trotzdem sind morphodynamische Prozesse in den Prielen besser gelöst als jene auf Tideflächen. Unsicherheiten werden aufgedeckt. Eine Analyse des Modellvertrauens zeigt, dass Sturmereignisse eine signifikante Relevanz für Ergebnisse zur Morphodynamik haben. Insgesamt erweist sich die Ensemblevorhersagemethode als ein nützliches Instrument, um Unsicherheiten in der morphodynamischen Modellierung zu berücksichtigen, um Wahrscheinlichkeitsbereiche zu zeigen und damit die Zuverlässigkeit der Ergebnisse der morphodynamischen Modellierung zu erhöhen.

Contents

List of Figures

List of Tables

List of Symbols

C	Chézy roughness coefficient [$\mathrm{m}^{0.5}\mathrm{s}^{-1}$]
D	erosion flux [$\mathrm{kg\,m^{-2}\,s^{-1}}$]
E	deposition flux [$\mathrm{kg\,m^{-2}\,s^{-1}}$]
H	wave height [m]
L	wavelength of tide *or* wave [m]
N	wave action density spectrum [$\mathrm{m^2\,Hz^{-1}}$]
S	bed slope [-]
S_b	bedload transport [$\mathrm{kg\,m^{-1}\,s^{-1}}$]
S_s	suspended load transport [$\mathrm{kg\,m^{-1}\,s^{-1}}$]
T	wave period *or* tidal period [s]
U	velocity magnitude [$\mathrm{m\,s^{-1}}$]
Re	Reynolds number [-]
ℓ	sediment fraction [-]
η	water level w.r.t. horizontal reference [m]
κ	constant of von Karman (=0.4) [-]
$\overline{\mathbf{x}}$	ensemble mean [m]
$\mathbf{s}$	ensemble standard deviation [m]
μ	dynamic viscosity coefficient [$\mathrm{kg\,m^{-1}\,s^{-1}}$]
ν	kinematic viscosity coefficient [$\mathrm{m^2\,s^{-1}}$]
ω	wave frequency [$\mathrm{rad\,s^{-1}}$]
ϕ	velocity potential [$\mathrm{m^2\,s^{-1}}$]
ρ	density of water [$\mathrm{kg\,m^{-3}}$]
ρ_s	density of sediment [$\mathrm{kg\,m^{-3}}$]
σ	relative wave frequency [-]
τ	shear stress [$\mathrm{N\,m^{-2}}$]
θ	Shields parameter *or* wave direction [rad]
ξ	wave energy density spectrum (source term) [$\mathrm{m^2\,Hz^{-1}}$]
a	wave amplitude *or* tidal amplitude [m]
c	celerity, phase velocity [$\mathrm{m\,s^{-1}}$] *or* concentration of constituent [$\mathrm{kg\,m^{-3}}$]
d_s	sieve diameter [m]
d_{50}	median grain size diameter [m]
g	gravitational acceleration (≈9.81) [$\mathrm{m\,s^{-2}}$]
h	water depth [m]
k	wave number [$\mathrm{m^{-1}}$]
k_s	roughness of Nikuradse [m]
p	pressure [$\mathrm{N\,m^{-2}}$]
s	relative density [-]

u, v, w	flow velocities in x-, y- and z-direction, resp. [$\mathrm{m\,s^{-1}}$]
u_*	shear or friction velocity [$\mathrm{m\,s^{-1}}$]
w_s	settling *or* fall velocity [$\mathrm{m\,s^{-1}}$]
z	elevation above the bed [m]
ADCP	Acoustic Doppler Current Profiler
BSS	Brier Skill Score
CI	Confidence Index
CSM	Continental Shelf Model
DEA	Deutsche Erdoel AG (former RWE Dea AG)
DWD	Deutscher Wetterdienst (German Weather Service)
GBM	German Bight Model
MCS	Monte Carlo Simulation
MDPI	Mittelplate Drilling and Production Island
MDPIM	Mittelplate Drilling and Production Island Model
NF	Neufahrwasser
NHN	Normalhöhennull (German standard reference level)
RMAE	Relative Mean Absolute Error
RMSE	Relative Mean Square Error
SI	Skill Index
SSC	Suspended Sediment Concentration
SWAN	Simulating WAves Nearshore
TF	Trischenflinge

Chapter 1

Introduction

Morphodynamic modelling enables bathymetric evolution to be investigated and understood under controlled conditions. This can be achieved via physical scale models in a laboratory flume or via numerical models using the virtual laboratory of a computer, for example. Physical scale models have been first applied to estuarine morphodynamics by Reynolds (1887, 1889, 1890, 1891), in which tests were carried out in a laboratory flume to investigate the action of waves and currents. For the current study however, a process-based numerical modelling approach was chosen, which is based on a detailed mathematical description of the underlying physical processes. Process-based models consist of sets of discretized equations which describe processes such as hydrodynamics (water level variations, currents and waves) and sediment transport in a water body. These models need a careful selection of the physical processes to be simulated. Each of the relevant processes should be modelled adequately, not only in the sense of process description, but also the combination of the modules, which forms the model as a whole (de Vriend and Ribbernik, 1996).

Traditional numerical modelling of ocean and coastal systems has its origins in the physical sciences and it is built around the simulation of physical processes such as hydrodynamics, sediment dynamics and morphodynamics. The modelling of an estuary, for instance, starts with some approximations to the Navier-Stokes equations - they describe how the velocity, pressure, temperature, and density of a moving fluid are related. This model contains parameters whose values must be estimated, thus a process of calibration against measured data is needed. The outcomes of such models are used to drive sediment dynamics and morphodynamics. They also require data, assumption and estimations of complex processes, some of which are not sufficiently understood. According to the error propagation involved, the final model results must be evaluated with care due to the embedded uncertainties.

Moreover, the application of a model always implies a trade-off between complexity and speed. The physical system must be simplified in such a way that no relevant processes are neglected, while simultaneously computational time is kept within acceptable limits. The application of a morphological scaling factor is often chosen as a model reduction approach in order to speed up the simulation of morphodynamic developments. As a matter of fact, terms as *input reduction* and *model reduction* have become a common practice in the scientific community. The main assumption behind the *input reduction* hypothesis is that hydrodynamic processes take place on a much smaller time scale than morphological developments. *Model reduction* refers to models that use only key processes to describe the most important physical processes. In most cases both *input reduction* and *model reduction* concepts are applied. This allows modellers to experiment with morphological evolution under basically any condition and to understand long-term sediment transport processes in a better way. Nevertheless, the input reduction approach always ends up with an additional uncertainty related to the reduction method applied.

Despite such techniques showing good performance for qualitative evaluation, the results from quantitative methods of comparison are not so satisfactory, as reported by Lesser (2009). Dastgheib (2012) also stated that models which perform well for small-scale phenomena do not necessarily perform adequately on larger scales and vice versa. Furthermore, Fortunato et al. (2009) argued that the limits of predictability of morphodynamic model applications are higher for slowly varying systems. Their attempts to reduce uncertainty by aggregating model results at larger spatial scales produced limited success. They suggested ensemble simulations as a possible avenue to investigate the long-term evolution of tidal inlets using process-based models. This approach could provide not only a prediction, but also a measure of its reliability.

Morphodynamic modelling methods based on dynamic equations are called *deterministic*, because from known initial conditions the simulated variable may be found exactly in terms of the numerical solution. However, the large range of time scales over which different processes occur leads to substantial computational difficulties for longer-term predictions. Furthermore, results of non-linear deterministic models for meteorological forecasting over long periods have proven that even very small perturbations in the model boundary conditions can lead to highly divergent predictions (Palmer et al., 1990). This behaviour is sometimes referred as "chaotic". It is therefore reasonable to expect that the non-linear deterministic process equations used for morphological prediction may also exhibit such behaviour. Thus, there may be an inherent limit to the period of time over which they may provide acceptable results.

One alternative to the deterministic modelling approach is to employ stochastic forecasting methods. They are more rigorous versions of the sensitivity analysis undertaken in engineering design, which involve repeating the forecast while systematically perturbing the input variables. A set of simulation results is thus generated and the sensitivity of the forecast to individual variables may be assessed. These methods are called *stochastic* or *probabilistic*, because the statistics of the variables of interest are forecast, rather than the variables themselves. One of the most widely known stochastic techniques is the Monte Carlo Simulation (MCS).

1.1 Motivation

Instead of applying a model with reduced inputs to simulate morphological evolution, the present study will emphasize non-reduced morphodynamic modelling in order to focus on the intrinsic uncertainties of morphodynamic modelling itself, and avoid extra sources of uncertainty in model results. A probabilistic approach will be considered together with a deterministic model. With the help of the MCS method, a process-based model for estimating morphological evolution can be used to generate a set of predictions from which statistics are derived.

The study area embeds a tidal channel system located in the Dithmarschen Bight, on the German North Sea coast. It has been extensively studied and previous works have provided large quantities of measured data (Mayerle and Zielke, 2005), expertise on modelling the local sediment dynamics (Poerbandono, 2003; Pramono, 2005; Escobar Sierra, 2007) and morphodynamics (Etri, 2007; Nguyen, 2015). Additionally, due to the construction of an oil platform on the tidal flats twenty-five years ago, high-resolution bathymetric measurements of its surroundings are available. The high amount and quality of measurements available in this area enables the investigation of complex morphological processes, such as the migration of tidal channels.

The combination of all the elements presented provide an optimal situation to investigate the migration of tidal channels, the limits of morphodynamic models, and also an opportunity to improve them.

1.2 Objectives

The overall goal of the proposed study is to investigate the governing processes responsible for the morphodynamic migration of a tidal channel system in the Dithmarschen Bight, by means of a process-based numerical model. A probabilistic approach will be used to describe the range of uncertainties in sedi-

ment transport modelling. Once uncertainties are taken into consideration, this approach will be applied to a morphodynamic model to generate an ensemble. Results from the ensemble members will be then analysed and assessed through statistics.

In order to achieve this goal, the following objectives shall be pursued:

- A probabilistic method will be adapted to a deterministic model, in which sediment transport uncertainties are taken into account. This will enable to address morphodynamic model results in terms of derived statistics.

- The relevance of sediment transport parameters will be investigated so that the ones significantly affecting sediment dynamics can be identified and their ranges of influence accordingly defined. This sensitivity analysis will determine how much each model parameter can be perturbed and, therefore, how much they might contribute to sediment transport uncertainty.

- The probabilistic method taking sediment transport uncertainties into account will be applied to a process-based morphodynamic model. This final step will make use of the Monte Carlo Simulation method to generate and simulate a morphodynamic ensemble, which will be the base for all model evaluation.

Chapter 2

Literature review

This chapter introduces basic concepts and processes related to significant physical processes to hydrodynamics and sediment transport. First basic definitions and mathematical concepts about tides and waves are introduced. Then, sediment transport concepts are given followed by a brief discussion on uncertainties related to sediment characterization. At last, an overview of processes taking place on the tidal flats is presented.

2.1 Hydrodynamic processes

2.1.1 Tides and water levels

Tides are long waves generally with semi diurnal ($T \approx 12\,\mathrm{h}$) or diurnal period ($T \approx 24\,\mathrm{h}$). Tidal waves are driven by the gravitational pull of the Moon and the Sun. The Moon remains in orbit around the Earth because the gravitational attraction is equal to the centrifugal force. The water in the oceans is therefore pulled towards the Moon. The gravitational attraction is greater than the centrifugal force on the side of the Earth closer to the Moon, while the opposite occurs on the side further away. The same principle is true for the gravitational pull of the Sun, except that its gravitational influence is less than half of the influence of the Moon. The combination of bulges associated with the Moon and the Sun depends on their relative positions to the Earth. When they act in the same direction (i.e. full moon and new moon), the bulges are added up causing spring tides, whereas when the Moon and the Sun are at right angles (i.e. first and last quarters), the bulge effects partially cancel each other causing neap tides (see Figure 2.1).

The dynamic theory of tides, developed by Laplace in 1775, describes the ocean's real reaction to tidal forces. In the 1860s William Thomson improved Laplace's theory by the application of Fourier analysis to the tidal motions as

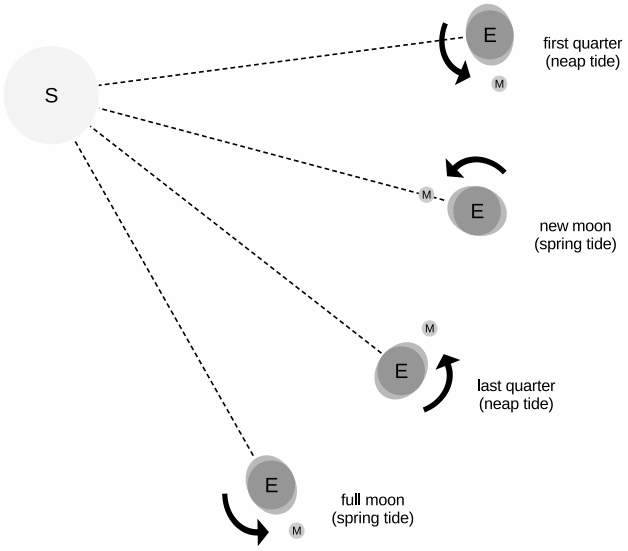

Figure 2.1: Bulge generation in relation to Moon and Sun's position.

harmonic analysis, which considers the tide as a superposition of hundreds of tidal constituents (harmonics). If the ocean surface is in equilibrium with the tidal potential, which means we ignore inertia and currents and assume no land, the principal tidal constituents would have amplitudes given in Table 2.1 (Apel, 1987).

Table 2.1: Principal tidal constituents

tidal specie	symbol	a [m]	T [h]
semidiurnal			
principal lunar	M_2	0.2423	12.4206
principal solar	S_2	0.1128	12.0000
lunar elliptic	N_2	0.0464	12.6584
lunisolar	K_2	0.0307	11.9673
diurnal			
lunisolar	K_1	0.1416	23.9344
principal lunar	O_1	0.1005	25.8194
principal solar	P_1	0.0468	24.0659
lunar elliptic	Q_1	0.0193	26.8684
long period			
fortnightly	M_f	0.0417	327.8599
monthly	M_m	0.0220	661.3111
semi-annual	S_{sa}	0.0194	4383.0763

The Coriolis force (due to the Earth's rotation) causes tidal waves to rotate counter-clockwise in the northern hemisphere and clockwise in the southern hemisphere. The standing tide rotates around a node, called amphidromic point. The

tide has no amplitude at amphidromic points; however, amplitude increases away from them, and can reach several meters on the margin of wide oceans. Magnitudes of tide-generating forces can be precisely resolved to give tidal predictions. Nevertheless, the height of the water is also subject to atmospheric and meteorological factors, and tidal predictions are only an approximation for actual water levels.

When tides approach shallow water regions of continental shelves, tidal range is increased while tidal wave velocity is decreased. Tidal range is related to the broad distribution of coastal landforms. Tidal current magnitude depends on tidal range and coastal topography. Tidal currents can be dominant in embayments, estuaries, straits and tidal creeks, resulting in distinctive tide-dominated landforms.

The most important phenomena of water level fluctuations concerning design is storm surge, which is an increase in water level resulting from shear stress by onshore wind over the water surface. This temporary water level increase occurs at the same time as major wave action, and it is the main cause of flooding and coastal damage.

During storm surges the water level at a downwind shore will be raised until gravity counteracts the shear stress from the wind. For simple problems in which the wind-generated shear stress is taken as the main driving force, the storm surge can be reduced to a one-dimensional computation

$$\frac{dh_s}{dx} = \frac{c_D(U\cos\psi)^2}{g(h+h_s)} \tag{2.1}$$

where h_s is the storm surge, x is the distance over which the storm surge is calculated, c_D is a constant, U is the wind speed, ψ is the angle between the wind direction and the x-axis, and h is the initial water depth.

In addition to the water level difference caused by the wind shear stress, there is also the barometric surge. Since strong winds are the result of large pressure fluctuations, a barometric surge will happen together with a storm surge. Given a difference in barometric pressure of Δp between the sea and the shore, the additional water level rise Δh is given by

$$\Delta h = \frac{\Delta p}{\rho g} \tag{2.2}$$

where ρ is the density of water. This roughly results in about 0.1 m per kPa of pressure difference. Large pressure systems in the atmosphere can easily generate 5 kPa of pressure difference, meaning about 0.5 m barometric surge.

2.1.2 Waves

Waves are undulations that move across a medium transferring energy, but generally not resulting in a net transfer of mass. Those on the ocean surface can be generated from several sources, but all of them consist of successive crests and troughs, as shown in Figure 2.2a.

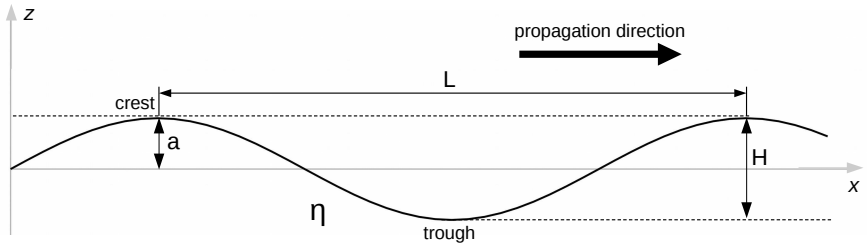

(a) definition of terms

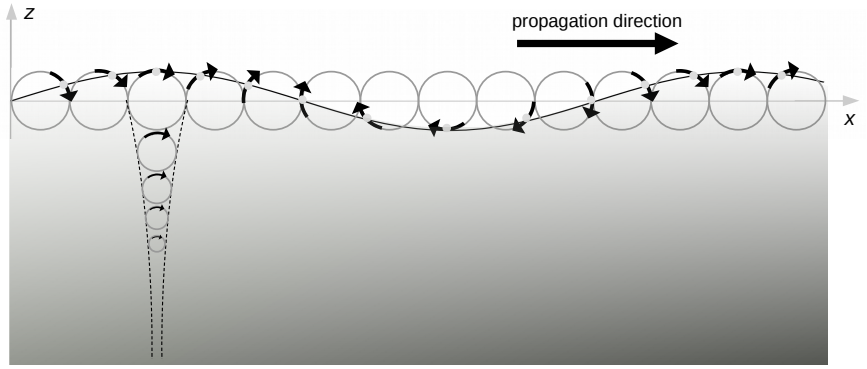

(b) wave propagation

Figure 2.2: Linear wave theory.

Wave height H is a measure of the difference between a wave crest and the adjacent wave trough, and according to linear wave theory it is equal to twice the wave amplitude a. Based on the linear wave theory assumptions, the sea surface elevation η of a wave travelling in x direction is given by

$$\eta = a\sin(\omega t - kx) \tag{2.3}$$

$$\omega = \frac{2\pi}{T} \qquad k = \frac{2\pi}{L} \tag{2.4}$$

where ω is the wave frequency, k is the wave number, L is the wave length and T is the wave period. The wave period T is the time taken for two successive wave crests or troughs to pass a fixed point, and the wavelength L is the distance between two successive wave crests or troughs at a fixed time. The wave frequency

ω is related to the wave number k by the *dispersion relation*

$$\omega^2 = gk \tanh(kh) \tag{2.5}$$

where g is the gravitational acceleration and h is the water depth. The phase velocity or celerity c is the speed at which a particular phase of the wave propagates, e.g. the speed of the wave crest propagation. Thus, the definition of phase velocity c is

$$c \equiv \frac{\omega}{k} = \frac{L}{T} \tag{2.6}$$

The velocity potential ϕ is defined as a function of which the spatial derivatives are equal to the water particles velocities, given by

$$u = \frac{\partial \phi}{\partial x} \qquad w = \frac{\partial \phi}{\partial z} \tag{2.7}$$

The expression for the function ϕ can be determined by applying boundary conditions to Equation (2.3),

$$\frac{\partial \phi}{\partial z} = \left.\frac{\partial \eta}{\partial t}\right|_{z=0} \tag{2.8}$$

$$\phi = \frac{\omega a}{k} \frac{\cosh[k(h+z)]}{\sinh(kh)} \cos(\omega t - kx) \tag{2.9}$$

The particle velocities u and w are therefore obtained by substituting Equation (2.9) in (2.7):

$$\begin{aligned} u &= \omega a \frac{\cosh[k(h+z)]}{\sinh(kh)} \sin(\omega t - kx) \\ w &= \omega a \frac{\sinh[k(h+z)]}{\sinh(kh)} \cos(\omega t - kx) \end{aligned} \tag{2.10}$$

These velocities are called *orbital velocities*, because they correspond to motion of the particles in circular or elliptical orbits, as shown in Figure 2.2b.

The linear wave theory matches the spectral description of ocean waves perfectly, since the spectral description is based on the assumption that wave components are harmonic and independent. However, when the waves are too steep or the water is too shallow, linear wave theory is no longer valid and the spectrum no longer provides a complete statistical and physical description of the waves.

When non-linear effects are to be considered on a small scale (e.g. wave forces on a marine structure), the waves need to be considered locally with a non-linear theory. A conventional approach usually applied is to treat each wave individually

and independently. The wave characteristics are computed on a wave-by-wave basis with a non-linear theory and the computational results for a large number of individual waves are analysed statistically to provide average characteristics.

In the wave generation area the sea surface becomes very agitated as waves with a full range of heights and frequencies superimpose each other. The height of wind-generated waves depends on the wind speed, the fetch[1], and the duration of the wind event. When fetch length is sufficient or a storm blows for a sufficient period of time, the agitation reaches a state called *fully developed sea*. After this state is reached, the size and characteristics of the waves do not change.

Only the wave form, and not the water mass, travels out of the area of generation, and is then called *swell*. In the wave generation area there is a broad spectrum of wave periods from 0.1 s ripples to 15 s large waves. However, the smallest waves disappear over short distances and usually only a limited range of wave periods reaches the shore.

Waves entering shallow water are likely to refract. Their propagation slowly changes towards the coastline due to the friction between the wave and the sea floor. Wave crests become increasingly parallel to seabed contours until they are almost parallel to the shore. This occurs because water depth varies along a wave crest that approaches the shore at an oblique angle. Wave speed in shallow water is related to water depth, and therefore, those parts of a wave entering shallow water move forward more slowly than those parts in deeper water.

Once the waves reach the surf zone, they may generate three types of currents: undertow, rip and longshore currents. Undertow currents occur as part of the balance of stresses and represent a transfer of water seaward along the bed. Rip currents are observed in many beaches, and are generally part of a cell circulation. Their occurrence is indicated by an increase in turbulence and flow velocities greater than $1\,\mathrm{m\,s^{-1}}$. A circulation develops with water flow seaward of the breaker zone. Rip currents occur when the angle of waves approaching the shore is small. If the angle is large, rip circulations are more likely to be replaced by longshore currents. Longshore currents are responsible for the longshore sediment transport, also called littoral drift.

2.2 Sediment transport

Sediment that is moved by tides, currents, waves and wind may be divided into cross-shore and alongshore sediment transport. The sediment movement, or sediment transport, can result in erosion or deposition of material. Erosion normally results in shoreline recession (movement of the shoreline inland), whereas

[1] The distance along which the wind is affecting the sea surface.

deposition causes the shoreline to move out to sea.

Considering only the cross-shore sediment movement, a seabed profile responds to storm-calm cycles by shifting sand in the cross-shore direction, forming a dynamic equilibrium. But any coastal area will need additional material during times of high stress, such as during the combination of high wave action and storm surge. Nature stocks large quantities of sand in dunes for such emergencies. Dunes are a long-term protection against coastal erosion, because they provide adequate elevation of the land contours to prevent flooding and form emergency reservoirs of sand.

Under rough conditions, such as major storms and storm surges, bed material on shallower areas is moved offshore. This allows waves to come further into shore and to attack the base of the dunes. This process removes material from the dunes and deposits large amounts of sand close to the shore, compensating for the sand moved offshore by storm waves. When weather conditions go back to normal, most or all of the sediment moved offshore will normally return onshore forming beaches. Winds will then blow dry sand inland to replenish the dunes. Ideally, a dune-beach system can thus take care of extreme weather events in the long term. In practice, the situation is complicated by alongshore transport, offshore bar formations, canyons, etc. Such complexities may prevent some of the sediment from moving back onshore after a storm.

The sediment transported by water depends on the properties of sediment (i.e. density, porosity, shape and size) and on the properties of water (i.e. density and viscosity), besides hydrodynamic conditions. Finally, the application of fluid dynamics principles to the transport of sediment involves high degree of mathematical simplification in relation to how idealized grains might act under steady flow of incompressible fluids.

The most usual and convenient method for the analysis of particle size distribution is the sieve analysis, which is applicable for particle sizes larger than 63 µm. The result of such analysis is a frequency curve or a cumulative frequency curve (grain-size distribution curve). In the frequency curve the abscissa represents the sieve diameter d_s. Very often the distribution curve can be approximated by a normal distribution and its median d_{50} represents the diameter of which 50% of the grains by weight are finer (and 50% are coarser).

The density of grains ρ_s is the parameter which exhibits the smallest variation under natural conditions. The relative density s is given by

$$s = \rho_s/\rho \tag{2.11}$$

in which ρ denotes the density of water. For natural sediments s is usually very

close to 2.65.

The settling or fall velocity w_s of a grain is defined as the terminal velocity attained when grain is settling in a fluid under the action of gravity. It depends on several parameters, the most important being grain size, density, shape and the drag coefficient (c_D), which is related to the fluid dynamic viscosity by the Reynolds number (Re).

$$w_s = \sqrt{\frac{4(s-1)gd_s}{3c_D}}, \qquad Re = \frac{w_s d_s}{\nu} \tag{2.12}$$

The bottom or bed shear stress τ_b is defined as the force per unit area parallel to the bed that exerts fluid drag across the projected area of the bed material in the flow direction. The overall time-averaged bed shear stress is defined as

$$\tau_b = \rho g h S \tag{2.13}$$

where S is the bed slope. By definition,

$$\tau_b = \rho u_*^2 \quad \therefore \quad u_* = \sqrt{ghS} \tag{2.14}$$

where u_* is called shear or friction velocity.

The Chézy roughness coefficient (C) can be calculated by combining the expression for the vertical velocity distribution (u) and the empirical equation for the depth-averaged velocity ($\overline{u}$) proposed by Chézy himself:

$$u = \frac{u_*}{\kappa} \ln\left(\frac{z}{z_0}\right), \qquad \overline{u} = C\sqrt{hS} \tag{2.15}$$

which for turbulent flow yields

$$C = 18 \log\left(\frac{12h}{k_s}\right) \tag{2.16}$$

where κ is the constant of von Karman, z_0 is the height from the bed when $u = 0$, and k_s is the Nikuradse roughness. The latter can be approximated by $k_s = 3d_{90}$ (van Rijn, 1993). Finally, the bed shear stress in a 2-D depth-averaged flow is given by

$$\tau_b = \rho g \frac{\overline{u}^2}{C^2} \tag{2.17}$$

Assuming a steady flow over a bed of non-cohesive material, this material will only move when the flow velocity becomes large enough so that the driving forces on the sediment particles will exceed the stabilizing forces. This flow velocity is called the critical flow velocity.

A classical solution to the problem was given by Shields (1936). The threshold of particle motion is supposed to be related to a given ratio between driving and stabilizing forces. The driving forces on a sediment particle resting on other particles on an originally plane horizontal bed are the drag (horizontal) and the lift (vertical) forces. The horizontal drag force F_D, generated by the flow, consists of skin friction acting on the surface of the grain. It generates drag due to a pressure difference on the up- and downstream sides of the grain due to flow separation. From the drag theory it is known that

$$F_D = \frac{1}{2}\rho c_D \frac{\pi}{4} d_s^2 u_*^2. \tag{2.18}$$

If the critical friction velocity ($u_{*,c}$) denotes the situation where the grain is about to move, then the drag force is equal to the friction force. This gives a relation between friction velocity and sediment characteristics

$$\theta = \frac{u_*}{(s-1)gd_s} \tag{2.19}$$

and θ is called the Shields parameter. Shields (1936) presented the relation of θ and Reynolds number based on experimental observations. His diagram (Figure 2.3) is the most used groundwork for studies on initiation of sediment motion.

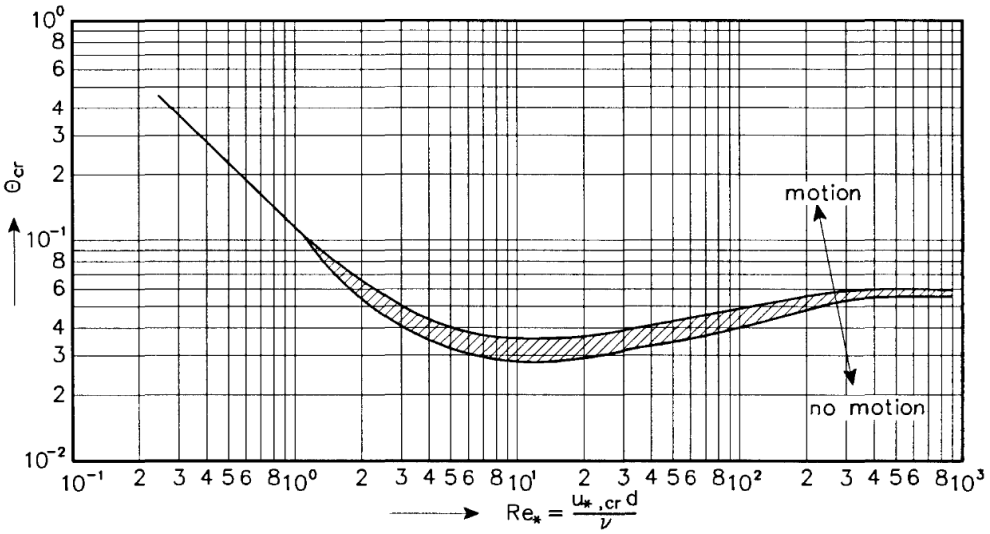

Figure 2.3: Initiation of motion on a plane bed (modified from Shields (1936)).

Sediment transport can be classified into three parts: bedload, suspended load and wash load. The *wash load* consists of very fine particles which are transported by the water and which normally are not represented in the bed. Therefore, the knowledge of bed material composition does not permit any prediction of the rate of wash load transport. Hence, when the term "total sediment discharge" is applied, the wash load is neglected.

Of the total sediment load a distinction between two categories is made: the bedload and the suspended load. The *bedload* is defined as the part of the total load which is more or less in continuous contact with the bed during the transport. It primarily includes grains that roll, slide or jump on the bed. Thus, the bedload must be determined almost exclusively by the effective bottom shear acting directly on the sediment surface. The *suspended load* is the part of the total load that is moving without continuous contact with the bed as a result of the agitation of fluid turbulence.

These categories of the sediment load exist in order to simplify the study of sediment transport in water, but sediment movement is actually one whole process. The effort of determining whether a sediment particle is moving or not by means of a threshold value improved our knowledge about this process; however, it does not explain all of it. The bedload is still far from being well represented by sediment transport formulas, because its exact measurement is still a difficult task. If we summarize the whole process of sediment motion, we could say that the suspended load is the part of the sediment in which the flow shear stresses overcome the critical value of the sediment shear stress; the material lying on the bed is the part of the sediment which has a much larger critical shear stress than the flow shear stress; and, the bedload is the transition between the two described states.

2.2.1 Uncertainties in sediment characterization

Processes that involve sediment movement are not simple to be directly measured and, therefore, quantified. Specially close to the seabed, several factors may contribute to their uncertainty estimation. Many of these factors cannot be fully explained by mathematical equations, such as the Shields parameter presented in Equation (2.19). These equations are mainly based on empirical formulations of sediment properties (e.g. median grain size) and depend on coefficients in order to fit observations (e.g. drag, roughness coefficient), apart from flow properties (e.g. current velocity).

Sediment transport rates are also known to strongly fluctuate even under steady flow conditions (Turowski, 2010). Additionally, the presence of very fine sediment particles ($d < 63\,\mu m$) adds another complication: cohesion. Cohesive sediment, commonly referred to as mud, is typically composed of mineral grains which originate from both fluvial and marine sources, together with biological matter. The primary mineral component of cohesive mud is clay, which has a plate-like structure and a diameter of a few micrometers. Cohesion arises through the electrostatic charging of the clay minerals as they pass through saline water.

The attraction of several electrostatic charged particles leads to the formation of aggregates/flocs, which significantly affects sediment settling velocity. In addition to that, seabed sediment properties are usually poorly known due to the amount of available measurements. Another complication is that these sediment measurements are usually carried out with grab samplers (e.g. van Veen), which only sample up to 20 cm into the seabed. Thus, the information about the sediment underlayers remains unknown.

Problems related to sediment transport uncertainty have been studied for more than 50 years. One of the first investigations on this topic addresses the fluctuations present in bedload transport (Hamamori, 1962). In a numerical sediment transport model, most part of basic hydraulic and sediment transport theories are included. However, the actual interactions between flow and bed are much more complex, and a fully numerical description of those processes is still not possible. Despite the fact that deterministic relationships are used in most sediment transport models, the outputs are subject to uncertainty due to the uncertain and stochastic nature of the input parameters.

For instance, Schmelter et al. (2012) applied a probabilistic approach to fluvial sediment transport in order to overcome the large measurement uncertainties. They showed how uncertainty propagates in the calculation of cumulative sediment transport. Turowski (2010) derived probability distributions of bedload transport rates and compared with high-resolution bed load transport data set from the Pitze stream (Austria). Even though measured bedload volumes varied up to four orders of magnitude at a given discharge, he showed that the gamma distribution performs best.

According to Yen (1986), uncertainties in hydraulic/hydrological analysis and modelling can be related (not only) to the following sources:

- Inherent uncertainties associated with the randomness of natural processes;
- Model uncertainty reflecting the inability of a simulation or design technique to represent the system's true physical behaviour;
- Parameter uncertainties resulting from an inability to accurately quantify the model input parameters;
- Data uncertainties including measurement errors, inconsistency, nonhomogeneity of data, data handling and transcription errors;
- Operational uncertainties, including those associated with construction, manufacturing, deterioration, maintenance, and other human factors not accounted for in the modelling or design procedures.

All these uncertainties may contribute to the stochasticity of the input parameters of a sediment transport model which, in turn, result in the output uncertainty. Next, studies related to sediment parameters that have a significant effect in model accuracy are cited. The information presented will be used as reference for model applications in the current work.

Grain size

According to van Vuren (2005), the uncertainty in specifying the grain size is inherent to the complexity of the morphodynamic systems, comprising the strong spatial and temporal variation of the bed material. In a simplified case study of the Waal River (Netherlands), she assumed a uniform grain size described by a log-normal probability distribution with a mean value of 1 mm and a standard deviation of 0.5 mm. Pinto et al. (2006) addressed current velocity and sediment median grain size as being the main physical properties that control the errors in transport of non-cohesive sediment evaluations. According to the authors, bedload estimates are mainly affected by current velocity and tests suggested that hydrodynamic simulations should be calibrated to within 10% errors in this property. Transport formulas turned out to be less sensitive to sediment grain size, although d_{50} values between 200 and 600 µm produced standard deviations an order of magnitude higher than their mean.

Shear stress

Darby and Sear (2008) presented a study case for the estimation of sediment discharge in the Goulburn River (Australia). They analysed the sources of uncertainty based on the consideration of sample uncertainty, measurement error and model error. Results of Monte Carlo analysis for the critical bed shear stress indicated deviations of 18% from the mean value with a 90% confidence interval. The variation of bed shear stress in swash flows has been investigated by Barnes and Baldock (2007) and Barnes et al. (2009), using a novel shear plate instrument. From maximum measured shear stress in the inner surf and swash zone, they presented errors up to ca. 25% from the mean value.

Settling velocity

Winterwerp et al. (2006) proposed an heuristic formula for describing settling velocity of cohesive sediment in estuaries and coastal seas. From measurements available in the Lower Sea Scheldt (Belgium) and in the Tamar River estuary (UK), they reported values of measured settling velocity in a wide range, varying between 0.5 and 5 mm s^{-1}. Model performance indicated standard deviations of

0.50 mm s^{-1} (Lower Sea Scheldt) and 0.69 mm s^{-1} (Tamar River estuary) between predictions and measurements. Soulsby et al. (2013) presented new formulations for the settling velocity of estuarine sediments. They came up with slightly better performance than Winterwerp et al. (2006), with a standard deviation of 0.49 mm s^{-1} instead of 0.69 mm s^{-1} calculated by the latter authors. For other data sets they found deviations of 0.40 and 0.59 mm s^{-1}. Fettweis (2008) related uncertainties in measurements of settling velocity to lack of accuracy of the measuring instruments and to the probabilistic nature of particle size distributions in the suspended matter. He underlined that the statistical nature of flocculation processes and settling velocity must be taken into account when modelling cohesive sediment transport. He suggested to consider at least one standard deviation of settling velocity based on measurements, or to introduce a floc size (and settling velocity) distribution in the transport model.

2.3 Dynamics of tidal flats

Tidal flats can be defined generally as level sediment surfaces bordering an estuary, alternately submerged and exposed by changing tidal levels. Tidal waters enter and leave a tidal flat through fairly straight major channels, with minor channels serving as tributaries as well as distributaries. The minor channels meander and migrate considerably over periods of several years. Tidal current velocity is an important parameter and usually in muddy coasts it shows an asymmetry, which is highly related to the local morphology. Flow is often defined in terms of peak velocity and hence the capacity to move sediment, although flow duration varies and can also determine net fluxes. Tidal flow can be either flood-dominated, when usually there is a net influx of sediment, or ebb-dominated with a tendency for net outflux. A muddy coast usually presents a typical progression: sandy channels in the lowest part of the tidal range; transition from sand flats replaced by mudflats in the upper intertidal; and, salt-marsh or mangrove wetlands in the highest part of the tidal range. Figure 2.4 shows two examples of typical tidal flat environments.

The source of fine sediment in tidal flats can be from a catchment, cliff erosion or a seaward source, and it varies between different systems. Usually muddy coasts are associated with major river deltas and often contain mud banks composed of sediment carried as suspended load from the river catchment. In some cases, however, there may be more mud than rivers can supply. Around the North Sea, input from rivers is insufficient to account for the volume of mud. According to Beets and van der Spek (2000), in the Netherlands only about 10% of the Holocene sediment budget has been derived from river input, and the majority

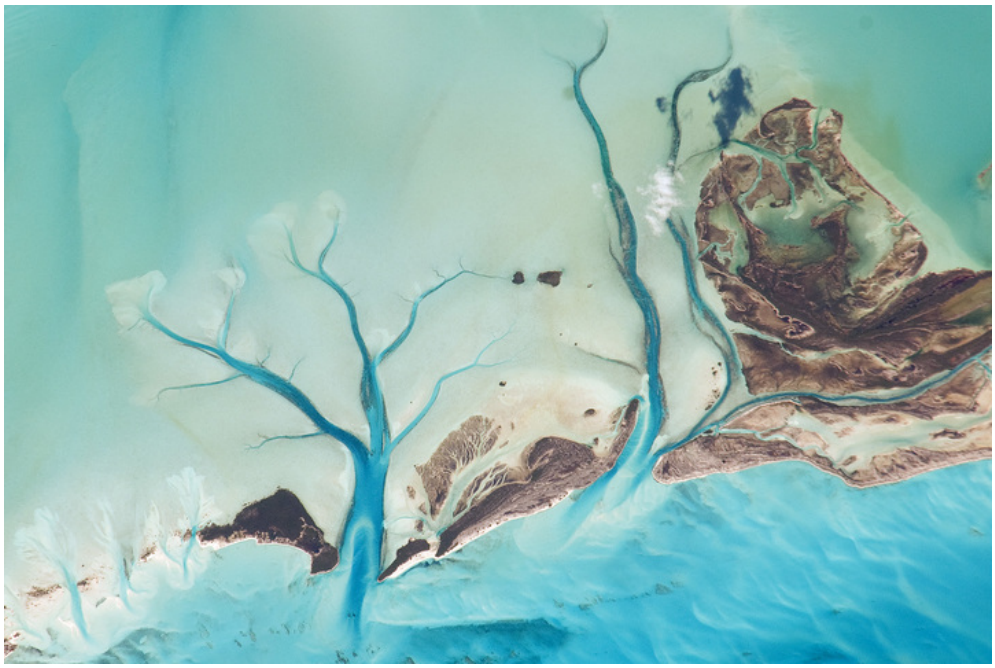

(a) sandy flat

(b) muddy flat

Figure 2.4: Examples of tidal flats: (a) Bahamas and (b) Wadden Sea.

Source: (a) NASA (2010); (b) Kaja (2011).

appears to be from offshore.

Coastal landforms tend to adjust towards, or oscillate around, an equilibrium particularly by negative feedback between variables. The concept of morphological equilibrium is a very useful generalization, because it provides insight into the future changes, but rarely it is possible to identify exactly how equilibrium is

achieved or what variables to measure. In some cases there is a simple equilibrium that changes little over time, and in other cases the coast adopts a dynamic equilibrium.

Le Hir et al. (2000) describes schematically a possible tidal equilibrium profile development as follows:

> "...tidal asymmetry induces onshore sediment transport, then generates accretion on the upper flat leading to a convex bottom profile, which in turn favours an ebb dominance that enhances the seawards sediment transport etc. Finally a tidal equilibrium is likely to occur, with a resulting slope and convexity. Such an equilibrium can be upset by wavy episodes that erode the flat, prevent deposition on the upper flat and favour offshore transport."

Although both sand and mud occur in varying proportions in most flats, muddy tidal flats can be differentiated from sandy tidal flats primarily on hydrodynamic conditions. Whereas sand is moved across the shore mainly as bedload, mud is moved in suspension and can continue to be transported even when flow velocities reduce below threshold values. Mud is more difficult than sand to erode once deposited, because stability is increased as a result of flooding, drying, and changed sediment properties. The greater the cohesion of muddy sediments, the greater the entrainment velocities to erode it. Therefore, the greater the critical bed shear stresses, according to Hjulström (1935) and Shields (1936).

In a study about the geometry of tidal-channel systems, Cleveringa and Oost (1999) stated that "(tidal-)channel systems can be regarded as *self-similar fractal* networks". They concluded that, although such systems are strongly self-organising, they might be influenced by hydrodynamic processes and strong morphological feedbacks.

Although tide appears to be the most important force, waves also play an important role shaping tidal flats. Even small-amplitude waves can produce a higher bed shear stress than tides because of the back and forth motion, and because they can be accentuated under storm conditions. Mainly on mudflats, wind generated waves enhance sediment suspension during flood tide, and under strong wind conditions the suspended sediment concentration is significantly increased.

According to Dalrymple et al. (1992), relative importance of river outflow, waves and tidal currents may be represented by a triangle (Figure 2.5). Deltas are positioned at the apex because fluvial sediment source dominates, while non-deltaic coasts (strand plains and tidal flats) are located along the opposite, wave-tide side because sediment is moved onshore by waves and/or tides.

A vertical section through this prism can be used to classify coastal deposi-

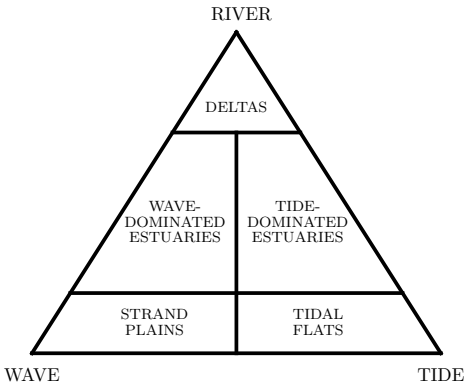

Figure 2.5: Ternary classification of coastal systems (Dalrymple et al., 1992).

tional systems. The upper triangle is equivalent to the delta triangle, whereas the narrow band at the base is conceptually similar to the bi-variate (wave/tide) classification of barrier coasts (Hayes, 1979). The trapezoidal area in the center provides a framework for the classification of estuaries.

Chapter 3

Study area

The current chapter describes specific aspects from the study area. First, the geographic location is presented in detail. Then, an overview on the hydrodynamics followed by the meteorology of the region is given. Finally, a description of the available measurements (e.g. hydrodynamics, sediment properties, bathymetry) in the area is presented.

3.1 Introduction

The channels formed in the tidal flats are main pathways responsible for bringing water from offshore into the tidal basin during flood tide, and for taking it back during ebb tide. A tidal channel system is very similar to a river catchment in terms of structure, in which a major channel coming from offshore is divided into smaller ones when approaching the tidal flats. Tidal channels might meander, just like rivers on a plain, and even migrate over several years. This behaviour is mostly not easy to predict, because of the long-term processes involved and the number of driving factors such as climate, sediment properties and anthropogenic impact. Nevertheless, changes in tidal flats can be identified by analysing a sequence of bathymetric measurements over enough time (usually from months to years).

A specific area in the middle of the German Wadden Sea was selected for understanding tidal channel migration processes (Figure 3.1), where not only several seabed surveys (bathymetry, surface and subsurface sediment) have been carried out in the last years, but also measurements of hydrodynamic conditions (water level, currents and waves). It is important to emphasize that the available bathymetric measurements should have a sufficient resolution in space and time, otherwise relevant morphological features cannot be identified nor tracked. The combination of these factors, seldom available elsewhere, provides an optimum situation for studying and better understanding such a complex process.

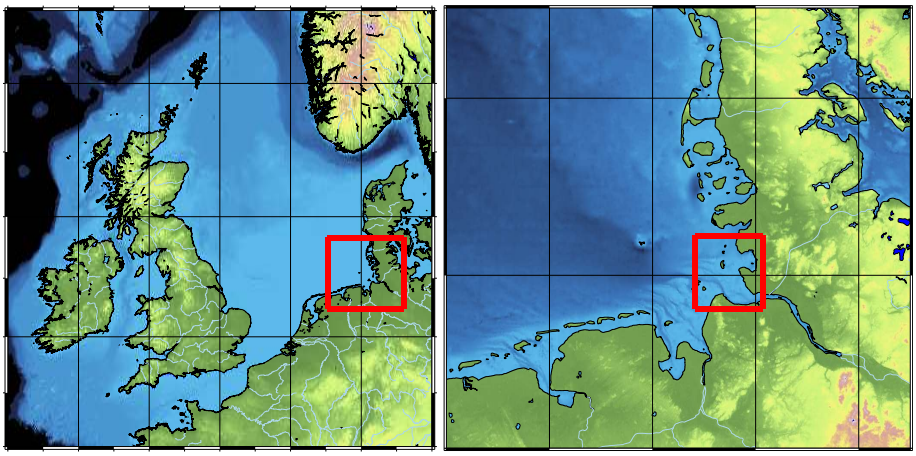

(a) North Sea (b) German Bight

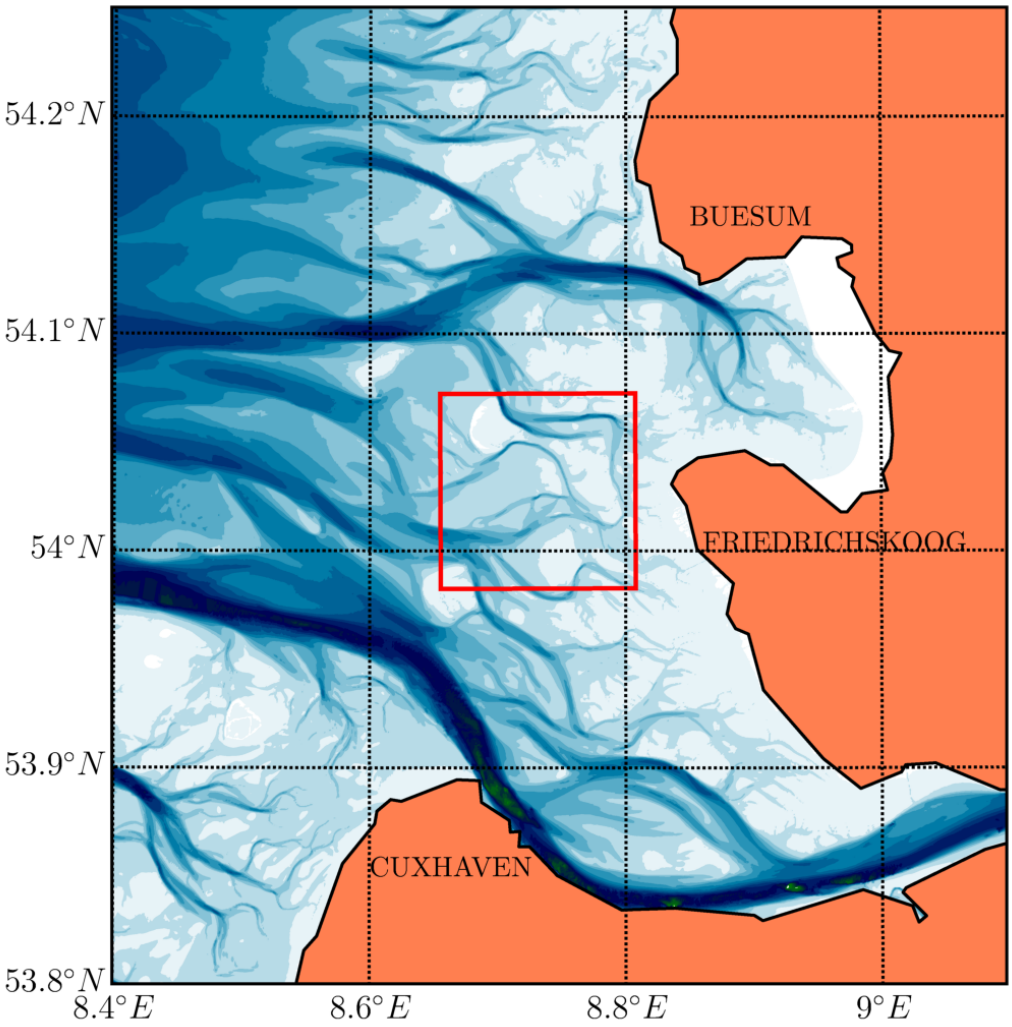

(c) Dithmarschen Bight

Figure 3.1: Study area located in the German Wadden Sea.

In the middle of the Dithmarschen Bight (red rectangle in Figure 3.1c) bathymetric surveys have been carried out in the last twenty years, and for the last ten years these surveys are available with a higher frequency (four to six times per year). The reason for such an effort is the presence of an oil platform in the middle of the tidal flats. Since the late 1980s, RWE Dea AG and Wintershall Holding AG open up oil reserves in that area. This oil platform, the *Mittelplate Drilling and Production Island* (MDPI), is located in the southern part of the Schleswig-Holstein's Wadden Sea. The tidal area, on which the MDPI is located, is bordered by the *Neufahrwasser* (NF) and the *Trischenflinge* (TF) tidal channels. Figure 3.2 shows the position of the MDPI on the tidal flat and its surroundings, while Figure 3.3 shows the area inside the red rectangle in more detail. The MDPI was built in 1985, and since the beginning of the 2000s the migration of the TF toward the platform became a major concern.

Figure 3.2: Aerial photograph taken from the Wadden area nearby the MDPI. (RWE Dea, 2006)

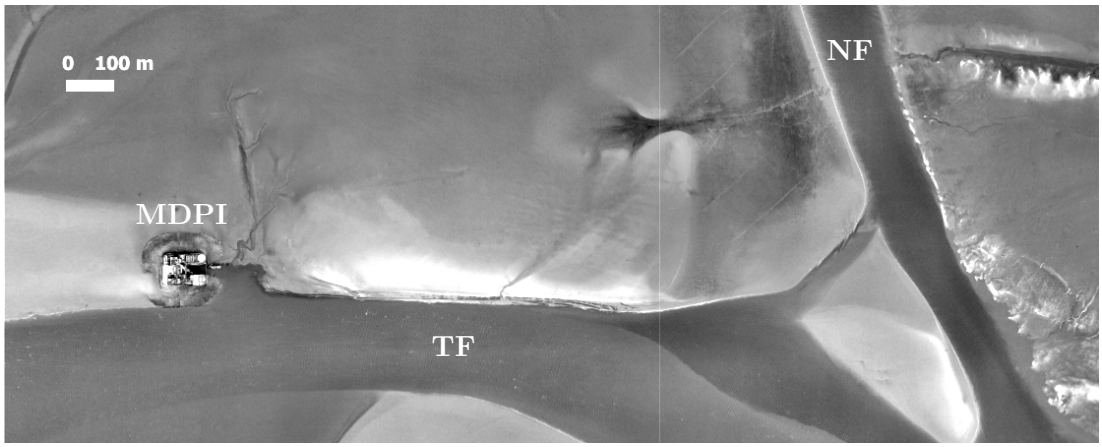

Figure 3.3: Aerial photograph zoomed in. (RWE Dea, 2006)

3.2 Hydrodynamics

Tidal oscillations in the North Sea are determined by its size and progressive semi-diurnal tides entering from the Atlantic Ocean. Tidal flow is deflected by the Coriolis force, resulting in three amphidromic points.

The investigation area Dithmarschen Bight is located between the Eiderstedt Peninsula in the north and the Elbe Estuary in the south. According to Toro et al. (2005), tidal conditions in the central Dithmarschen Bight depend primarily on the rotation of the semi-diurnal tidal wave around the amphidromic point in the south eastern part of the North Sea. The area is characterized by a semi-diurnal tide with a tidal period of 12 h and 24 min, and a mean tidal range between 3.1 m and 3.4 m. With reference to NHN (German standard reference level), the mean high and low water levels close to the coastline are +1.6 m and −1.6 m, respectively. Analysis of a long time series of water level measurements reveals that the mean tidal range in the study area is 3.2 m, with neap and spring tidal range of 2.8 m and 3.5 m, respectively.

Wave conditions in the study area are based on swell and wind-generated waves. Swell originates from the open North Sea, whereas wind-generated waves are created by local weather conditions. Wilkens (2004) presented a detailed analysis of wave measurements and concluded that in the Dithmarschen Bight the mean wave height is approx. 1 m outside of the Wadden Sea area and smaller than 0.3 m in the tidal flat area. A detailed investigation on the hydrodynamics of the Dithmarschen Bight is given in Mayerle and Zielke (2005).

By applying the classification of Hayes (1979) (Figure 3.4), the offshore part of the study area may be characterized as tide-dominated (black square), whereas the tidal flat sheltered areas as highly tide-dominated (grey square).

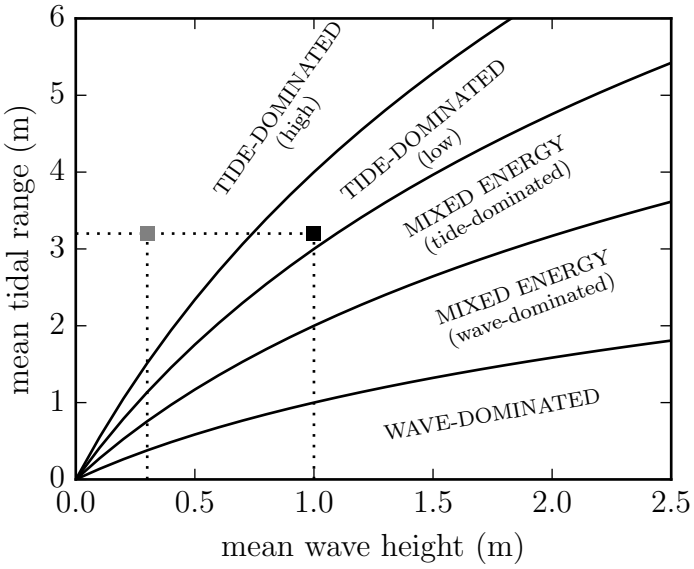

Figure 3.4: Classification of tidal areas according to Hayes (1979).

3.3 Meteorology

One important component in hydrodynamic modelling is the meteorological forcing. Although in some studies the effect of air pressure and wind fields can be neglected, usually that is not the case for coastal areas, where water set-up, wind-generated waves and storms play major roles in shaping the coast. However, neither wind and pressure fields can be assumed uniform for large areas such as the Wadden Sea, nor meteorological stations along the coast are sufficient able to determine the dynamics of the atmosphere. Instead, meteorological models are used to deliver high-resolution data in space and time that can be imposed to hydrodynamic models.

A meteorological model was evaluated by comparing time series of air pressure, wind magnitude and direction at three stations. In Table 3.1 the names of the stations and their coordinates are presented.

Table 3.1: DWD meteorological stations.

station	Helgoland	Norderney	Sylt
latitude (°N)	54.1750	53.7123	55.0110
longitude (°E)	7.8920	7.1519	8.4125

An overview of the dominant wind speed and direction is given next. The wind roses from three meteorological stations of the German Weather Service (DWD) are presented in Figure 3.5, which summarizes more than 55 years of available measurements at these stations.

At Helgoland and Sylt, islands directly exposed to the North Sea climate, a

dominance of winds from the west quadrant can be identified (frequency above 40%). At Norderney, westerly winds still occur in a higher frequency than other directions, except from south (weaker). This is probably a consequence of the station's location (East Frisian Islands), where land wind might have a stronger effect on the local weather.

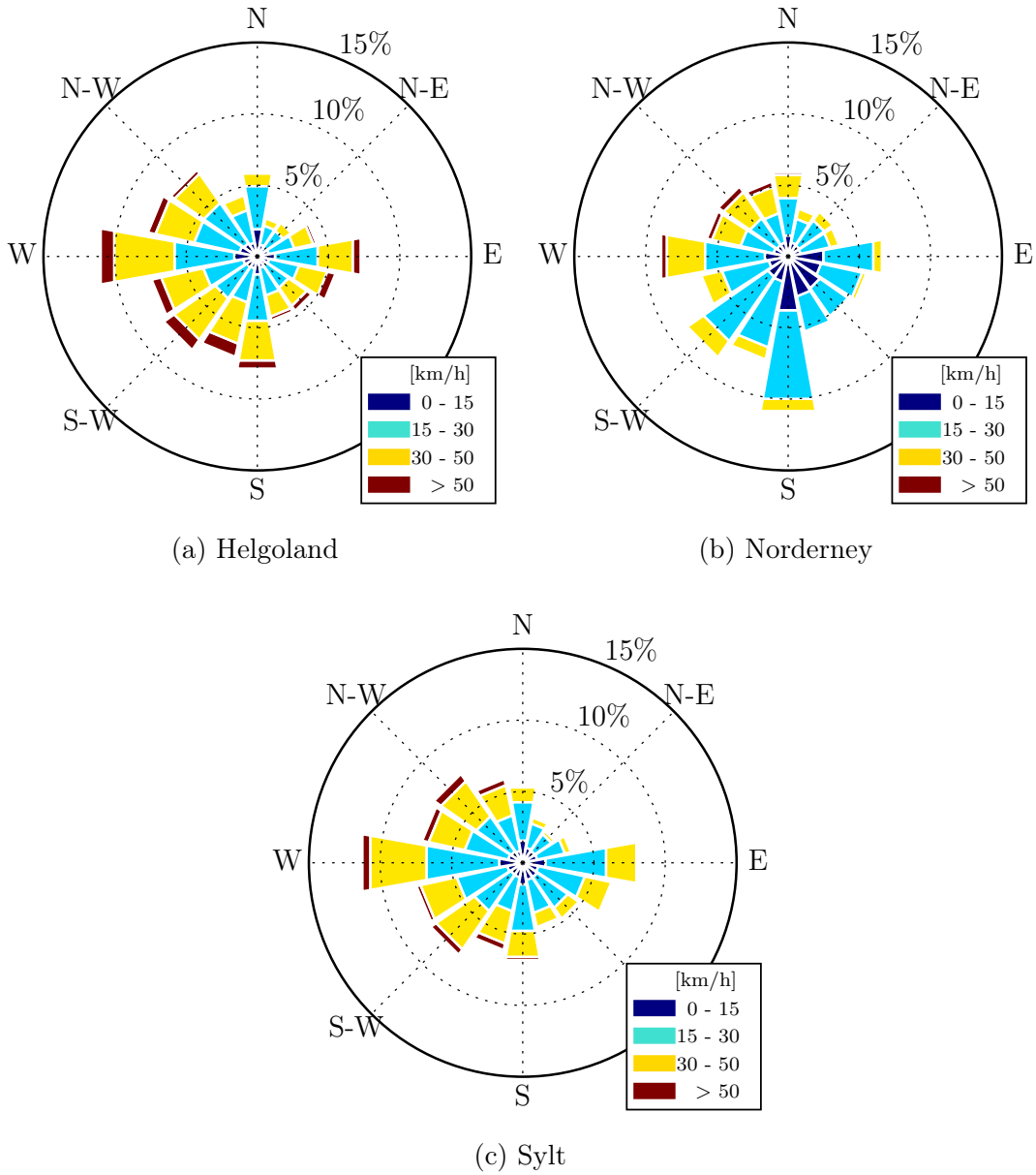

(a) Helgoland

(b) Norderney

(c) Sylt

Figure 3.5: Wind roses of the last 55 years from DWD meteorological stations.

3.4 Available data

In this section an overview of the available data used for the set-up and calibration of models are presented. First the measurements related to hydrodynamics

are described. After that, the sediment concentration measurements are introduced. Finally, the bathymetric dataset available at the study area is presented. In Figure 3.6 an overview of all the referred measuring locations is presented.

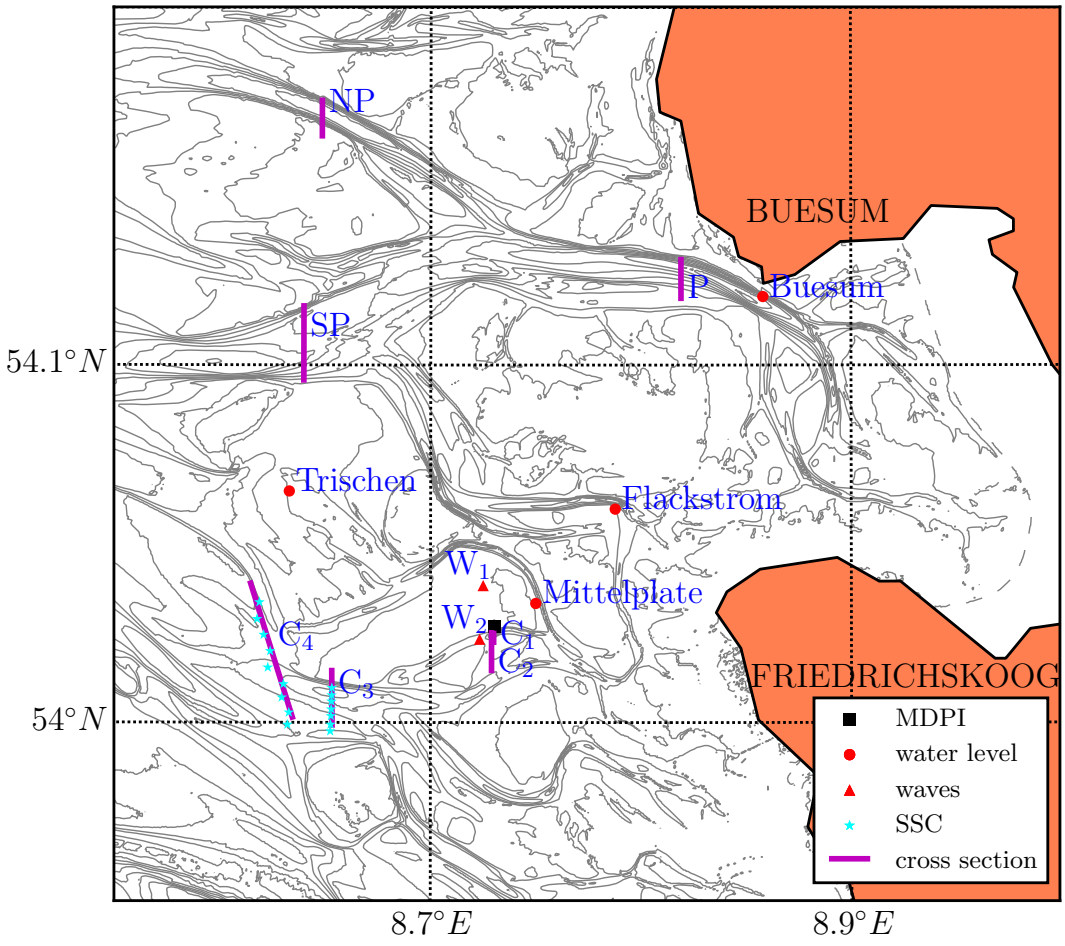

Figure 3.6: Overview of all measurement locations used in the present study.

3.4.1 Hydrodynamics

Hydrodynamic measurements provide the basic information needed for understanding the motion of a water body. Water level, flow velocity (currents) and wave characteristics (wave height, period and direction) are the most common measured parameters.

Water level

Water level measurements are available usually from tidal gauges, but sometimes also from deployed devices able to measure water pressure (e.g. stationary acoustic Doppler device, wave gauge, pressure sensor). The tidal gauges Büsum, Flackstrom, Mittelplate and Trischen have been used in this study (see Figure

3.6). The available data comes from the state enterprise for coastal protection, national park and marine protection from Schleswig-Holstein (LKN-SH). In the current study water level measurements from the following periods have been used: 06.2000, 10.2006, 02.2007 and 06.2009.

Currents

The measurement of flow velocity is carried out with an Acoustic Doppler Current Profiler (ADCP), which provides current magnitude and direction along the water column. Thanks to the Doppler principle, ADCP devices are able to measure over the entire water column indirect and non-intrusive current velocity along the three axis directions. Also, the ability of ADCP to detect the sea bottom provides a correction for measurement from a moving vessel as well as a good estimate of water depth.

The current velocity measurements available in the study area are coming from ADCP devices. Defined cross sections were measured during one or more tidal cycles. Velocities at the cross-sections Norderpiep (NP), Piep (P), Süderpiep (SP), C_2, C_3 and C_4 have been used. The location of the measured cross sections can be seen in Figure 3.6. Measured data has been made available from the framework of the project PROMORPH (Mayerle and Zielke, 2005) by the Research and Technology Centre West Coast, University of Kiel, as well as data from DEA (Deutsche Erdoel AG). The current study made use of current velocity measurements from the following periods: 06.2000, 02.2007 and 06.2009.

Waves

Measurements of wave characteristics are usually provided by buoys at a fixed position. The wave spectrum (i.e. wave energies with their associated frequencies) is estimated from the vertical displacement of the free water surface. From that, parameters such as significant wave height and wave period can be derived.

The available wave measurements used in the study come from two different devices (stationary ADCP and directional wave gauge) attached to the seabed. Both devices measure hydrostatic pressure with a high frequency, from which wave characteristics can be calculated.

Wave measurements at W_1 and W_2 are available from the Research and Technology Centre West Coast, University of Kiel (see Figure 3.6, red triangles). In the current study wave measurements from 05.2009 and 07.2009 have been used. A directional wave gauge has been deployed on a tidal flat (W_1), while a stationary ADCP has been deployed in a tidal channel (W_2). Thus, the comparison between deeper and shallower locations could also be analysed.

3.4.2 Sediment properties

The measurement of sediment concentration is crucial to understand sediment transport. As mentioned in Section 2.2, the total sediment load is divided into suspended load and bedload. In order to quantify each of them, different approaches are necessary, as described in the following.

Suspended load concentration

There are several measurement techniques of suspended sediment concentration. Devices for measuring sediment concentration in suspension can be based on mechanical, optical or acoustical principles. Further discussion on field techniques for suspended sediment concentration measurement is given in Wren et al. (2000).

The mechanical and the optical methods have been used for the available measurements of suspended sediment concentration in the study area. An optical transmissometer, a water sampler and a pressure sensor are mounted together for measuring simultaneously optical transmission, sediment concentration and water depth, respectively. This is often achieved by combining the optical transmissometer with a CTD device, an instrument used to determine the conductivity, temperature, and depth of the ocean.

An optical transmissometer consists of a light transmitter and receiver, separated by a known distance. The transmitter emits a light beam of known wavelength while the receiver detects how much of the beam is scattered back. The sediment particles in the measuring volume are responsible for reducing the detected signal by the receiver. The relationship between the detector signal (I) and the sediment concentration (c) is (van Rijn, 1993):

$$I = k_1 e^{-k_2 c} \tag{3.1}$$

in which k_1 is a calibration constant depending on instrument characteristics, fluid properties and travel distance; and, k_2 is a calibration constant depending on particle properties, wave length of light and travel distance.

Water sampler (e.g. Niskin Bottle) is a mechanical device, which is able to sample water at a certain depth. The water sample, after filtered, provides the sediment concentration, which is related to the respective transmissometer measurement. Several water samples over depth are necessary for defining the calibration constants from Equation (3.1) in order to relate sediment concentration to optical transmission, and so a calibration curve is constructed. With the calibration curve it is possible to estimate the sediment concentration profile over the entire water column based on measured optical transmission.

In the present work suspended sediment concentrations (SSC) have been calculated from transmissometer and water sample measurements at cross-sections C_3 and C_4 (see Figure 3.6). Measurements used have been carried out during the following days: 17.06.2009, 24.06.2009, 30.06.2009 and 01.07.2009.

Consolidated sediment layer

In the Dithmarschen region, a widely spread clay deposit has been formed under permanent submarine conditions around 5,000 years ago. This layer, known as *Dithmarschen clay*, reaches a thickness of up to 10 m and is usually found in depths of 15 to 24 m. The erosion resistance of such a cohesive sediment layer is high according to the consolidation level. According to Neto (2004), the Dithmarschen clay represents an effective limitation for the depths of tidal channels.

If tidal channels are considered depth-limited, the way sediment dynamics is evaluated changes drastically. Instead of further deepening when erosion would take place in the channel bed, equilibrium must be achieved by lateral erosion (channel widening) or even by creating a secondary channel somewhere near the primary one.

In the underground of the MDPI, a consolidated cohesive sediment layer with similar properties from the Dithmarschen clay has been identified in depths of 6.5 to 8 m by means of borehole logs. Studies showed that the presence of this layer plays a major role in the tidal channel migration process (Mayerle et al., 2010; Nguyen et al., 2010; Nguyen, 2015).

Figure 3.7 presents schematically the consolidated layer position along a cross-section in the TF channel. On the right hand-side of the figure, it is shown the borehole log of resistance (MN m^{-2}) from the tip of the drilling, nearby the MDPI. At depths where muddy layers are present, the resistance decreases.

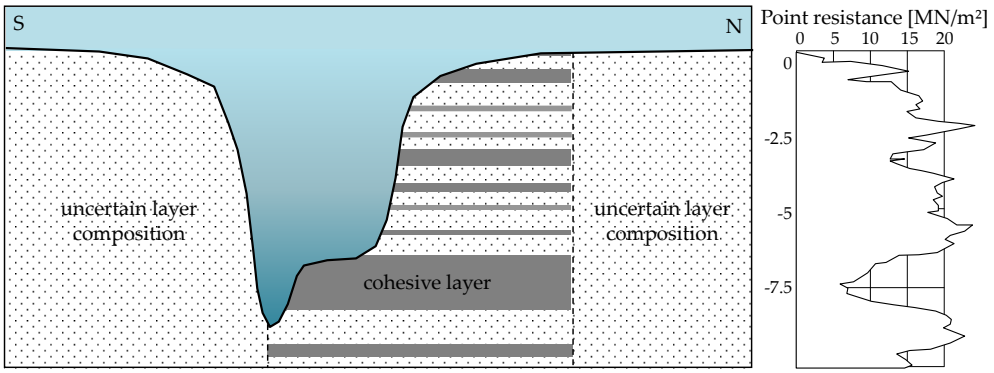

Figure 3.7: Sediment layer representation for the Trischenflinge central cross-section.

Source: Modified from Mayerle et al. (2010)

3.4.3 Bathymetry

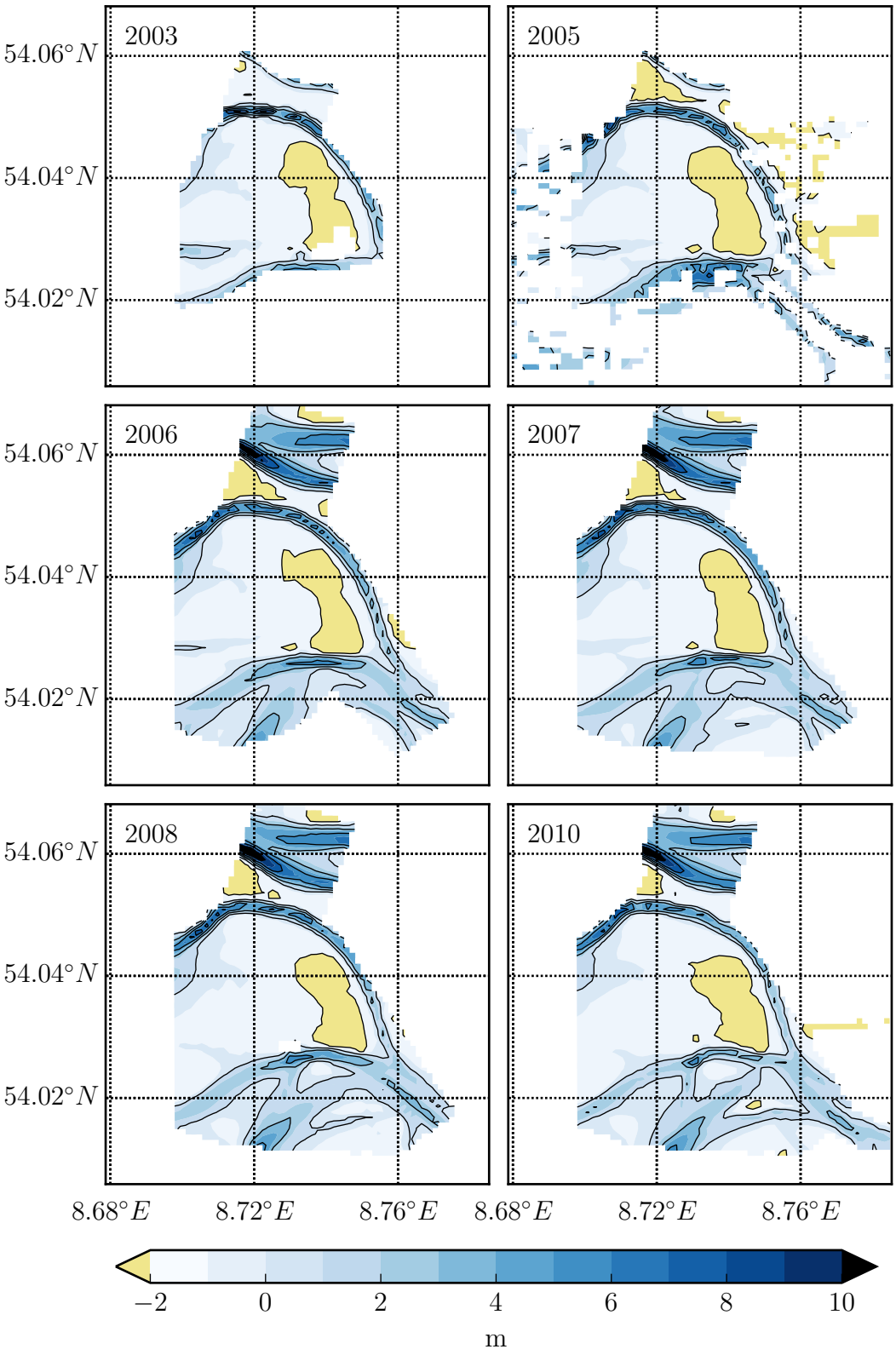

Figure 3.8: Bathymetric measurements in the MDPI surroundings [I] (positive values indicate deeper areas).

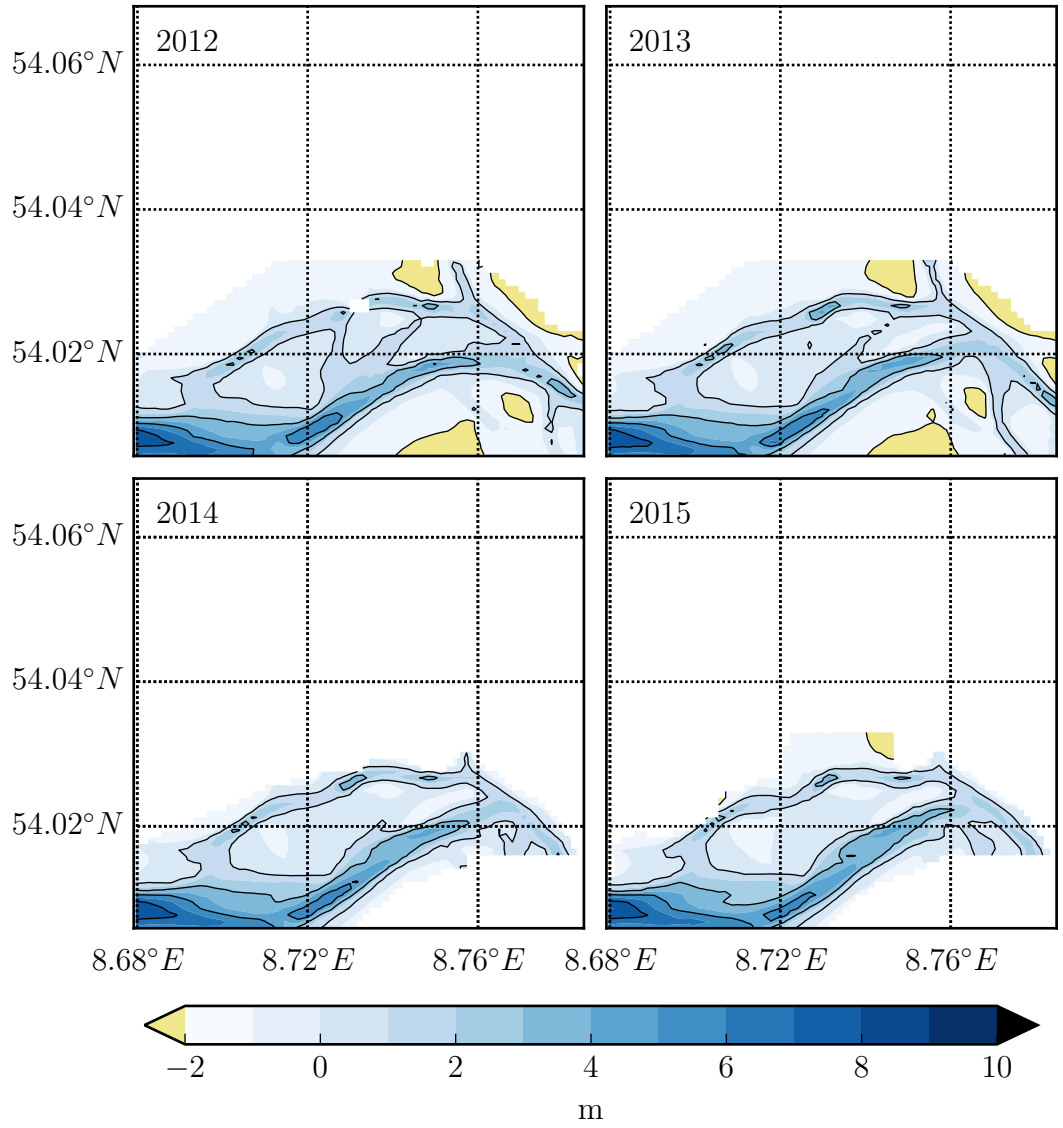

Figure 3.9: Bathymetric measurements in the MDPI surroundings [II] (positive values indicate deeper areas).

Bathymetric measurements are the most important source of information for understanding the morphodynamics of a region. In the MDPI area the dataset covers more than ten years of high-resolution surveys with several measurements per year depending on the location.

In the German Bight measurements are available from the German Federal Maritime and Hydrographic Agency and from the German Federal Waterway and Shipping Administration (WSV) for the period from 1969 to 2009. Bathymetric surveys of the TF tidal channel and the adjacent tidal flat were provided by DEA from 2006 to 2016. A visual analysis can already provide a good picture of which changes have taken place. Figures 3.8 and 3.9 present the interpolated bathymetric measurements from 2003 to 2015, when large areas in the MDPI vicinity were surveyed.

In the bathymetric maps some important changes in the xy-plane can be identified. The most important ones are:

- Retreat of a channel westward from the MDPI between 2003 and 2008;
- More pronounced sedimentation of the NF eastwards from the MDPI between 2003 and 2010;
- Advance of the TF toward the MDPI mainly between 2003 and 2010;
- Formation of a tidal channel parallel to the TF since 2007 and further development into a main channel.

In order to analyse changes in tidal channels several cross-sections along the channels are considered. Figure 3.10 shows the location of the cross-sections.

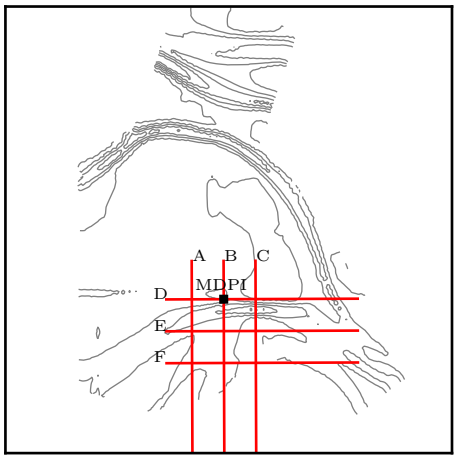

Figure 3.10: Location of bathymetric cross-sections.

In Figure 3.11 (S-N cross-sections), the development of a southern channel (left side) is represented. The Trischenflinge channel migration is represented on the right side of the figure. Its migration on the west (A) is southward, whereas on the east (C) is northward. In the middle at the MDPI (B), the migration is slightly northward, but it is stopped by the oil platform's protection structure. Although its migration towards the MDPI is observed until the year 2010, afterwards a decrease on its depth and a retreat to the south has been registered until 2015.

In Figure 3.12 (W-E cross-sections), the first cross-section at the MDPI (D), it is shown how far the Trischenflinge channel deepens itself, east from the platform. Around longitude 8.74° the bed level is subjected to ca. 5 m of erosion, from 2006 to 2008. In cross-section E, a general sedimentation is observed. In cross-section F, the east part presents sedimentation from 2003 to 2010. Two years later, the same section became a tidal channel with ca. 6 m depth, and in 2015 the channel migrated westward.

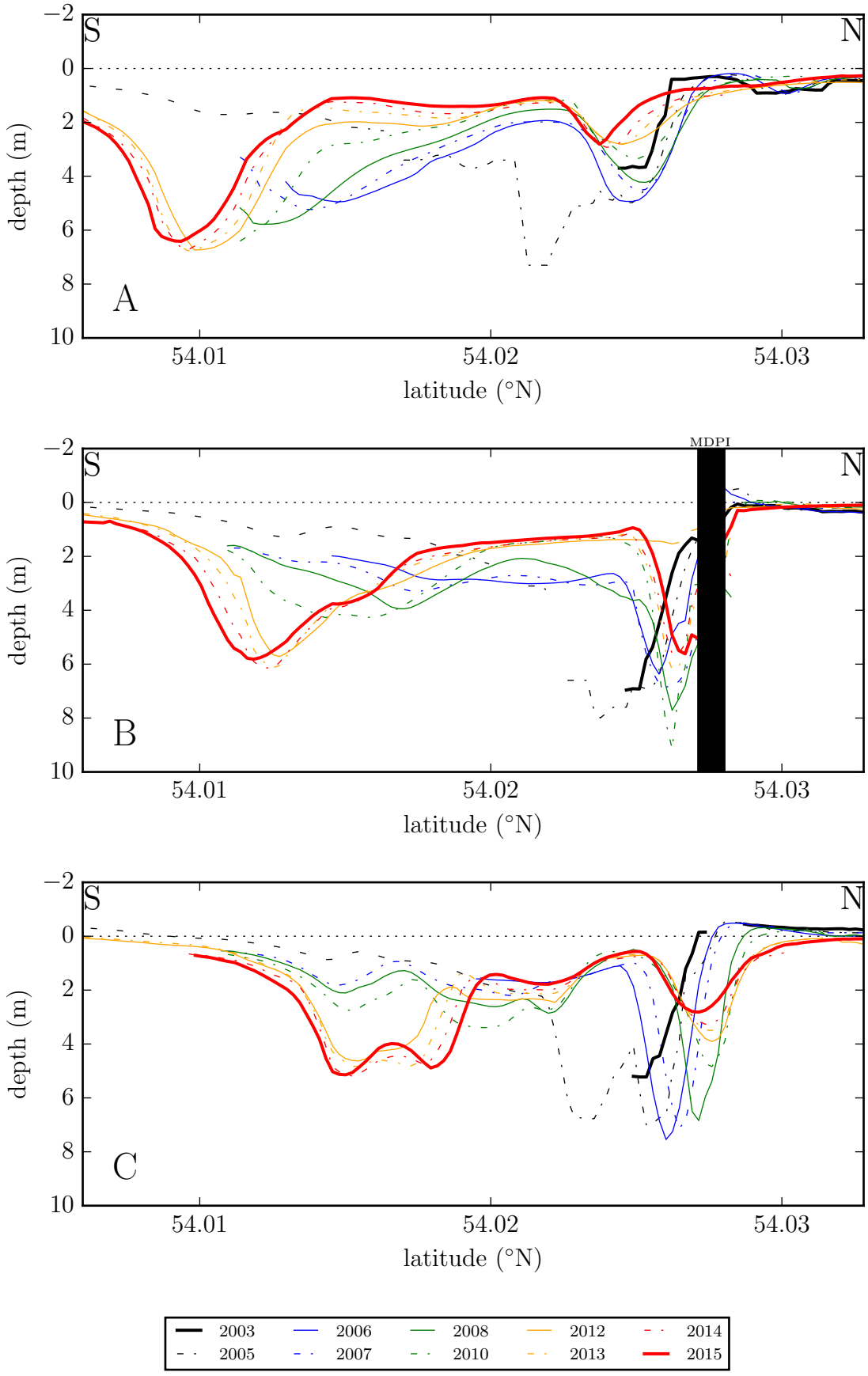

Figure 3.11: S-N cross-sections in the MDPI surroundings.

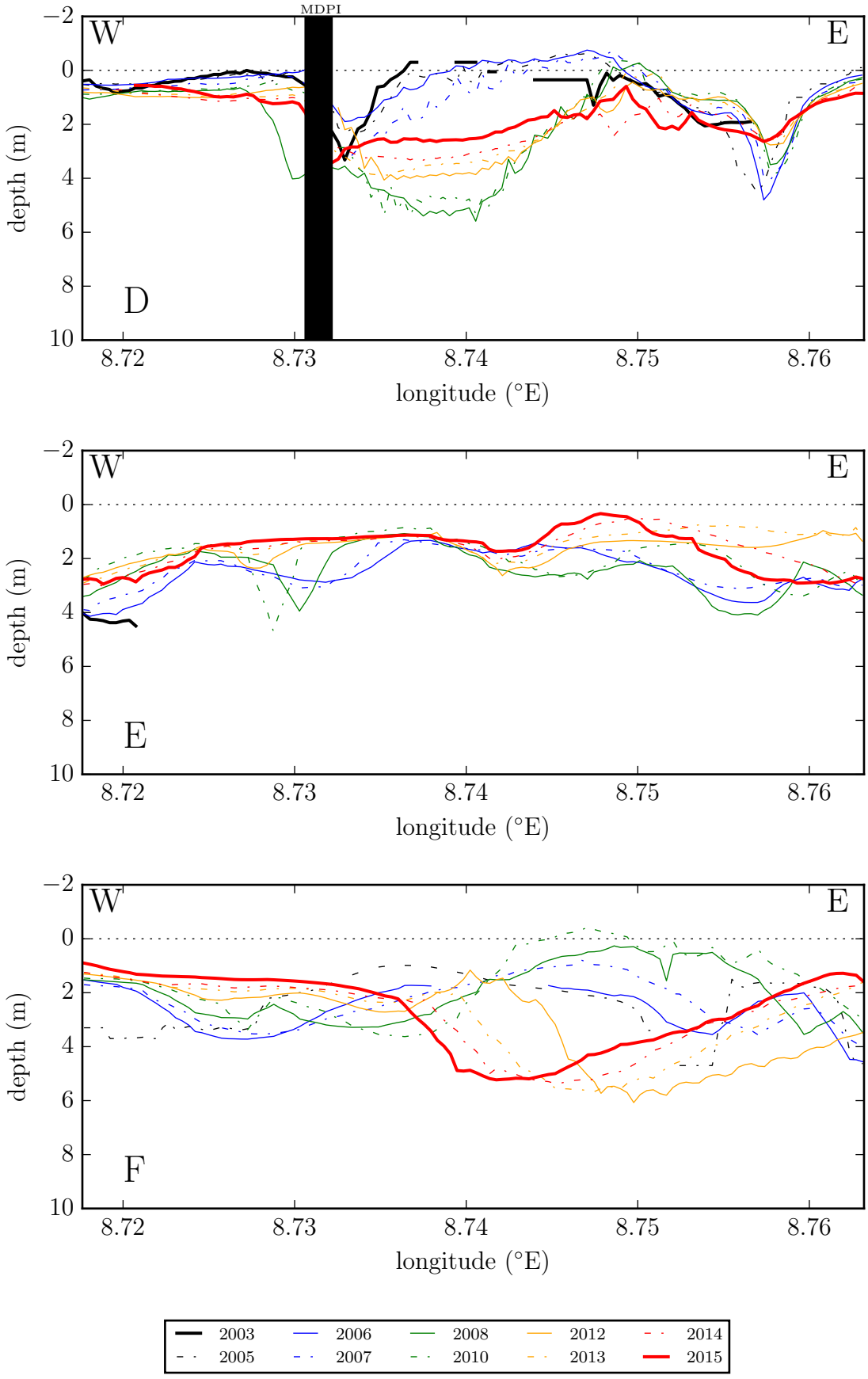

Figure 3.12: W-E cross-sections in the MDPI surroundings.

Chapter 4

Methods

The methods used for calculating and evaluating morphodynamic evolution are presented in this chapter. First, a detailed description of the process-based numerical model is given. Then, a method for assessing energy transferred from meteorological input to the model is presented. After that, the concepts of ensemble simulations applied to morphodynamics are explained. At last, statistical tools used for model analysis are introduced.

4.1 Process-based numerical model

The description of how the velocity, pressure, temperature, and density of a moving fluid are related is given by a set of differential equations called the Navier-Stokes equations. For an incompressible fluid (such as water[1]) they consist of a time-dependent continuity equation for conservation of mass and three time-dependent conservation of momentum equations (one for each spatial dimension). The solution of the Navier-Stokes equations is a flow velocity field for a given time point. Once the velocity field is calculated, other quantities of interest, such as pressure or temperature, may be found.

The Delft3D modelling system, developed by Deltares (Deltares, 2016), consists of a hydrodynamic module that solves the Navier-Stokes equations and a wave module that solves the discrete spectral action balance equation, under the shallow water assumption. The interaction between these two modules takes into account the effect of waves on current (via forcing, enhanced turbulence and bed shear stress) and the effect of currents on waves (via set-up, current refraction and enhanced bottom friction). Sediment transport and morphological update formulations, predominantly based on the formulations of van Rijn (1993), are added directly into the hydrodynamic solver, thereby closely coupling hydro-

[1]Water is a fluid with low compressibility under standard temperature and pressure conditions ($\approx 0.5\,\mathrm{GPa}^{-1}$) and can be assumed as incompressible.

dynamic, sediment transport, and morphodynamic computations. In the next sections, the description of the main processes included in the numerical models are presented. Additionally, for a more detailed description and for practical use, reference is made to the user manuals of Delft3D-FLOW and Delft3D-WAVE (Deltares, 2014a,b).

4.1.1 Staggered grid

The numerical method of Delft3D-FLOW is based on finite differences, and the discretization of the shallow water equations in space is done through a curvilinear grid assumed to be orthogonal and well-structured. The primitive variables, water level (η) and velocity (u, v, w), describe the flow. To discretize the three-dimensional equations, the variables are arranged in a special way on the grid known as staggered grid, see Figure 4.1. This particular arrangement of the variables is called the Arakawa C-grid, in which the water level points are defined in the centre of a cell and the velocity components are perpendicular to the grid cell faces where they are situated.

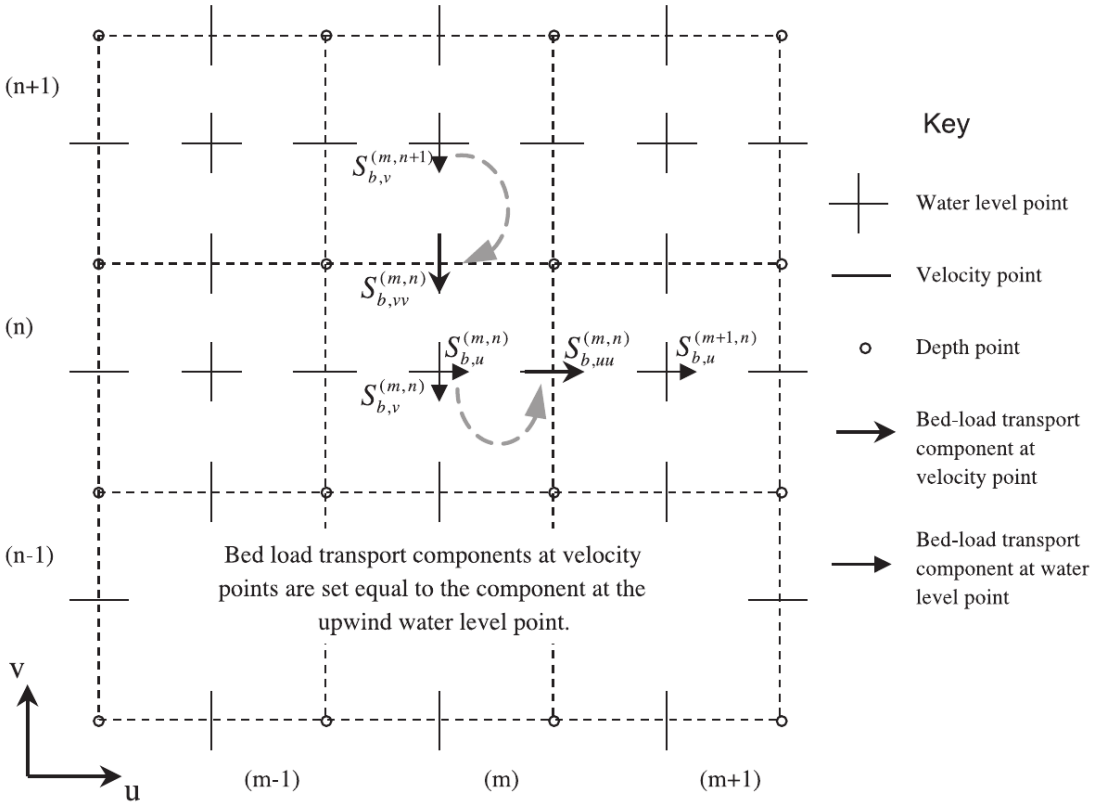

Figure 4.1: Transport vectors in staggered grid in Delft3D. (Lesser et al., 2004)

4.1.2 Hydrodynamics

The Delft3D-FLOW module solves the unsteady shallow-water equations in two (depth-averaged) or three dimensions. The system of equations consists of the horizontal momentum equations, the continuity equation, the transport equation and a turbulence closure model (3-D only). The vertical momentum equation is reduced to the hydrostatic pressure relation as vertical accelerations are assumed to be small compared to gravitational acceleration and are not taken into account. This makes Delft3D-FLOW model suitable for modelling hydrodynamics in shallow seas, coastal areas, estuaries, lagoons, rivers, and lakes. It aims to model flow phenomena of which the horizontal length and time scales are significantly larger than the vertical scales.

Continuity equation

The depth-averaged continuity equation is given by the continuity equation for incompressible fluids ($\nabla \cdot \vec{u} = 0$) integrated over the total depth,

$$\frac{\partial \eta}{\partial t} + h\left(\frac{\partial \bar{u}}{\partial x} + \frac{\partial \bar{v}}{\partial y}\right) = Q \tag{4.1}$$

in which η is the water level, h is the mean water depth, $\bar{u}$ and $\bar{v}$ are the depth-averaged velocity components, and Q represents the contributions per unit area due to the discharge or withdrawal of water, evaporation, and precipitation.

Horizontal momentum equations

The horizontal momentum equations are

$$\begin{aligned}
&\frac{\partial u}{\partial t} + u\frac{\partial u}{\partial x} + v\frac{\partial u}{\partial y} + \frac{w}{h}\frac{\partial u}{\partial \sigma} - fv = -\frac{1}{\rho}p_x + F_x + M_x + \frac{1}{h^2}\frac{\partial}{\partial \sigma}\left(\nu_V \frac{\partial u}{\partial \sigma}\right) \\
&\frac{\partial v}{\partial t} + u\frac{\partial v}{\partial x} + v\frac{\partial v}{\partial y} + \frac{w}{h}\frac{\partial v}{\partial \sigma} - fu = -\frac{1}{\rho}p_y + F_y + M_y + \frac{1}{h^2}\frac{\partial}{\partial \sigma}\left(\nu_V \frac{\partial v}{\partial \sigma}\right)
\end{aligned} \tag{4.2}$$

in which u, v and w are the velocity components (in x, y and z directions, resp.), f is the Coriolis parameter, ρ is the density of water, p_x and p_y are the horizontal pressure terms, F_x and F_y are the horizontal Reynolds stresses, M_x and M_y represent the contributions due to external sources or sinks of momentum, and ν_V is the vertical eddy viscosity.

The Reynolds stresses are modelled using the eddy viscosity concept. For large-scale simulations (when shear stresses along closed boundaries may be ne-

glected) the forces F_x and F_y reduce to the simplified formulations

$$F_x = \nu_H \left(\frac{\partial^2 u}{\partial x^2} + \frac{\partial^2 u}{\partial y^2} \right) \qquad F_y = \nu_H \left(\frac{\partial^2 v}{\partial x^2} + \frac{\partial^2 v}{\partial y^2} \right) \tag{4.3}$$

in which ν_H is the horizontal eddy viscosity.

Hydrostatic pressure

Under the shallow water assumption, the vertical momentum equation is reduced to the hydrostatic pressure equation. Vertical accelerations due to buoyancy effects or sudden variations in the bottom topography are assumed negligible compared to gravitational acceleration and are not taken into account. The hydrostatic pressure equation is given by

$$\frac{\partial p}{\partial z} = -\rho g \tag{4.4}$$

The gradients of the free surface level are called barotropic pressure gradients. The atmospheric pressure is included in the system for storm surge simulations. The atmospheric pressure gradients dominate the external forcing at peak winds during storm events. For water of constant density and taking into account the atmospheric pressure, the pressure gradients are

$$\frac{1}{\rho} p_x = g \frac{\partial \eta}{\partial x} + \frac{1}{\rho} \frac{\partial p_{atm}}{\partial x} \qquad \frac{1}{\rho} p_y = g \frac{\partial \eta}{\partial y} + \frac{1}{\rho} \frac{\partial p_{atm}}{\partial y} \tag{4.5}$$

Transport equation

The flows in rivers, estuaries, and coastal seas often transport dissolved substances, salinity and/or heat. In Delft3D-FLOW, the transport of matter and heat is modelled by an advection-diffusion equation in three co-ordinate directions. Source and sink terms are included to simulate discharges and withdrawals. Also first-order decay processes may be taken into account.

The advection-diffusion equation is given by

$$\begin{aligned} &h \left(\frac{\partial c}{\partial t} + \frac{\partial uc}{\partial x} + \frac{\partial vc}{\partial y} \right) + \frac{\partial wc}{\partial z} = \\ &h \left[\frac{\partial}{\partial x} \left(D_H \frac{\partial c}{\partial x} \right) + \frac{\partial}{\partial y} \left(D_H \frac{\partial c}{\partial y} \right) \right] + \frac{1}{h} \frac{\partial}{\partial z} \left(D_V \frac{\partial c}{\partial z} \right) + hQ \end{aligned} \tag{4.6}$$

in which c is the constituent's concentration, D_H and D_V are the horizontal and vertical eddy diffusivity, and Q represents source and sink terms per unit area. In order to solve these equations, the horizontal and vertical viscosity (ν_H and ν_V) and diffusivity (D_H and D_V) need to be prescribed.

Boundary conditions

At the seabed, the boundary conditions for the momentum equations are

$$\frac{\nu_V}{h}\frac{\partial u}{\partial \sigma} = \frac{1}{\rho_0}\tau_{bx} \qquad \frac{\nu_V}{h}\frac{\partial v}{\partial \sigma} = \frac{1}{\rho_0}\tau_{by} \tag{4.7}$$

with τ_{bx} and τ_{by} the components of the bed stress. For 2-D depth-averaged flow the shear-stress at the bed induced by a turbulent flow is assumed to be given by a quadratic friction law

$$\overrightarrow{\tau_b} = \frac{\rho g \overrightarrow{U}|\overrightarrow{U}|}{C^2} \tag{4.8}$$

where $\overrightarrow{U}$ is the magnitude of the depth-averaged horizontal velocity and C is the Chézy roughness coefficient.

At the free surface the boundary conditions for the momentum equations are

$$\frac{\nu_V}{h}\frac{\partial u}{\partial \sigma} = \frac{1}{\rho_0}|\overrightarrow{\tau_s}|\cos\theta \qquad \frac{\nu_V}{h}\frac{\partial v}{\partial \sigma} = \frac{1}{\rho_0}|\overrightarrow{\tau_s}|\sin\theta \tag{4.9}$$

where θ is the angle between the wind stress vector and the local direction of the grid-line. Without wind, the stress at the free surface is zero. The magnitude of the wind shear-stress is defined as

$$|\overrightarrow{\tau_s}| = \rho_a c_D U_{10}^2 \tag{4.10}$$

where ρ_a is the density of air, c_D is the wind drag coefficient and U_{10} is the wind speed 10 meters above the free surface.

Waves

In relatively shallow areas ($L/T = \sqrt{gh}$) wave action becomes important because of several processes: (1) the vertical mixing processes are enhanced due to turbulence generated near the surface by whitecapping and wave breaking, and near the bottom due to energy dissipation in the bottom layer; (2) a net mass flux is generated, which has some effect on the current profile, especially in cross-shore direction; (3) in the surf zone long-shore currents and a cross-shore set-up is generated due to variations in the wave-induced momentum flux (radiation stress); (4) in case of an irregular surf zone, strong circulations may be generated due to bathymetry (rip currents); and, (5) the bed shear stress is enhanced, which affects the stirring up of sediments and increases the bed friction.

In Delft3D, wave simulations are performed using the 3$^{\text{rd}}$ generation SWAN[2] model (Holthuijsen et al., 1993). In SWAN, the waves are described by a two-

[2] SWAN is an acronym for Simulating WAves Nearshore

dimensional wave action density spectrum (N). The independent variables of the spectrum are the relative frequency σ (as observed in a frame of reference moving with the current velocity) and the wave direction θ (the direction normal to the wave crest of each spectral component). The spectrum may vary in space and time.

The evolution of the wave spectrum is described by the spectral action balance equation, which for Cartesian co-ordinates is

$$\frac{\partial}{\partial t}N + \frac{\partial}{\partial x}c_x N + \frac{\partial}{\partial y}c_y N + \frac{\partial}{\partial \sigma}c_\sigma N + \frac{\partial}{\partial \theta}c_\theta N = \frac{\xi}{\sigma} \tag{4.11}$$

The first term in the left-hand side of this equation represents the local rate of change of action density in time. The second and third terms represent the propagation of action in geographical space (with propagation velocities c_x and c_y in x- and y-space, respectively). The fourth term represents shifting of the relative frequency due to variations in depths and currents (with propagation velocity c_σ in σ-space), and the fifth term represents depth-induced and current-induced refraction (with propagation velocity c_θ in θ-space). The expressions for these propagation speeds are taken from linear wave theory. The term ξ at the right-hand side of the action balance equation, also function of σ and θ, is the source term in terms of energy density representing the effects of generation, dissipation and non-linear wave-wave interactions.

The effect of waves can be included in a Delft3D-FLOW simulation by running the Delft3D-WAVE module alongside. A call to the Delft3D-WAVE module must be made prior to running the FLOW module. This will result in a communication file being stored which contains the results of the wave simulation (e.g. RMS wave height, peak spectral period, wave direction, mass fluxes) on the same computational grid as is used by the FLOW module. The FLOW module can then read the wave results and include them in flow calculations. The simulation of wave-current interactions is referred to as *coupling*.

4.1.3 Suspended sediment transport

The transport of suspended sediment is calculated by solving the advection-diffusion equation. The local flow velocity and eddy diffusivity are based on the results of the hydrodynamic computations. The transport of sediment is computed in exactly the same way as the transport of any other conservative constituent, such as salinity, heat, and constituents. There are, however, a number of important differences between sediment and other constituents. For example, the exchange of sediment between the bed and the flow, and the settling velocity of sediment under the action of gravity. These additional processes for sediment are

obviously of critical importance. Other processes such as the effect that sediment has on the local mixture density, and hence on turbulence damping, can also be taken into account. In addition, if a net flux between sediment from the bed and the flow occurs, then the resulting change in the bathymetry should influence subsequent hydrodynamic calculations.

Density effects

The empirical relation formulated by UNESCO (1981) to adjust the density of water is used by default in Delft3D-FLOW in order to take varying temperature and salinity into account. For sediment transport this relation is extended to include the density effect of sediment fractions in the fluid mixture. This is achieved by adding (per unit volume) the mass of all sediment fractions, and subtracting the mass of the displaced water. As a mathematical statement this translates as

$$\rho_{mix}(sal, c^{(\ell)}) = \rho(sal) + \sum_{\ell=1}^{lsed} c^{(\ell)} \left(1 - \frac{\rho(sal)}{\rho_s^{(\ell)}}\right) \tag{4.12}$$

in which $\rho(sal)$ is the specific density of water with salinity concentration sal, $c^{(\ell)}$ is the mass concentration of sediment fraction (ℓ), $\rho_s^{(\ell)}$ is the specific density of sediment fraction (ℓ), and $lsed$ is the number of sediment fractions.

Settling velocity

The settling velocity for cohesive and non-cohesive sediment are strongly different in formulation. In salt water cohesive sediment tends to flocculate to form sediment "flocs", with the degree of flocculation depending on the salinity of the water. These flocs are much larger than the individual sediment particles and settle at a faster rate. In order to model this salinity dependency two settling velocities and a maximum salinity must be supplied.

Therefore, the settling velocity of a **cohesive sediment** fraction is calculated as

$$w_{s,0}^{(\ell)} = \begin{cases} \frac{w_{s,max}^{(\ell)}}{2}\left(1 - \cos(\frac{\pi sal}{sal_{max}})\right) + \frac{w_{s,f}^{(\ell)}}{2}\left(1 + \cos(\frac{\pi sal}{sal_{max}})\right) & \text{if } sal \leqslant sal_{max} \\ w_{s,max}^{(\ell)} & \text{if } sal > sal_{max} \end{cases} \tag{4.13}$$

in which $w_{s,0}^{(\ell)}$ is the (non-hindered) settling velocity of sediment fraction (ℓ), $w_{s,max}^{(\ell)}$ is the settling velocity of sediment fraction (ℓ) at maximal salinity concentration sal_{max}, and $w_{s,f}$ is the fresh water settling velocity of sediment fraction (ℓ).

The settling velocity of a **non-cohesive sediment** fraction is computed following the method of van Rijn (1993). This formulation depends on the diameter of the sediment in suspension

$$w_{s,0}^{(\ell)} = \begin{cases} \dfrac{(s^{(\ell)}-1)gd_s^{(\ell)2}}{18\nu} & \text{if } 65\mu m < d_s \leqslant 100\mu m \\ \dfrac{10\nu}{d_s}\left[\sqrt{1+\dfrac{0.01(s^{(\ell)}-1)gd_s^{(\ell)3}}{\nu^2}}-1\right] & \text{if } 100\mu m < d_s \leqslant 1000\mu m \\ 1.1\sqrt{(s^{(\ell)}-1)gd_s} & \text{if } d_s > 1000\mu m \end{cases} \tag{4.14}$$

in which $s^{(\ell)}$ is the relative density of sediment fraction (ℓ), $d_s^{(\ell)}$ is the representative diameter of sediment fraction (ℓ), and ν is the kinematic viscosity coefficient of water.

In high concentration mixtures, the settling velocity of a single particle is reduced due to the presence of other particles. In order to account for this hindered settling effect, the settling velocity in a fluid-sediment mixture as a function of the sediment concentration and the non-hindered settling fall velocity is determined according to Richardson and Zaki (1954)

$$w_s^{(\ell)} = \left(1 - \frac{\sum c_s^{(\ell)}}{\rho_{s,ref}}\right)^5 w_{s,0}^{(\ell)} \tag{4.15}$$

in which $\sum c_s^{(\ell)}$ is the sum of the mass concentrations of all sediment fractions, $\rho_{s,ref}$ is the reference density of sediment, and $w_{s,0}$ is the original sediment fraction settling velocity.

Dispersive transport

The sediment mixing coefficients $\varepsilon_{s,x}^{(\ell)}$, $\varepsilon_{s,y}^{(\ell)}$ and $\varepsilon_{s,z}^{(\ell)}$ depend on the flow characteristics (turbulence level, taking into account the effect of high sediment concentrations on damping turbulent exchange processes) and the influence of waves (due to wave induced currents and enhanced bed shear stresses).

Several *turbulence closure models* are available in Delft3D for three-dimensional models and their output is the eddy viscosity at each layer interface. For two-dimensional models the sediment mixing coefficients are represented by the horizontal eddy diffusivity (D_H).

Erosion and deposition

For **cohesive sediment** fractions, the fluxes between the water phase and the bed are calculated with the well-known Partheniades-Krone formulations (Parthe-

niades, 1965)

$$E^{(\ell)} = M^{(\ell)} F\left(\tau_{cw}, \tau_{cr,e}^{(\ell)}\right) \tag{4.16}$$

$$D^{(\ell)} = w_s^{(\ell)} c_b^{(\ell)} F\left(\tau_{cw}, \tau_{cr,d}^{(\ell)}\right) \tag{4.17}$$

in which $E^{(\ell)}$ is the erosion flux, $M^{(\ell)}$ is the user-defined erosion parameter, $D^{(\ell)}$ is the deposition flux, $w_s^{(\ell)}$ is the hindered settling velocity, $c_b^{(\ell)}$ is the average sediment concentration in the near bottom computational layer, τ_{cw} is the maximum bed shear stress due to currents and waves, $\tau_{cr,e}^{(\ell)}$ is the user-defined critical erosion shear stress, and $\tau_{cr,d}^{(\ell)}$ is the user-defined critical deposition shear stress. $F(\tau_{cw}, \tau_{cr,e}^{(\ell)})$ and $F(\tau_{cw}, \tau_{cr,d}^{(\ell)})$ are the erosion and deposition step functions, respectively, as follows

$$F(\tau_{cw}, \tau_{cr,e}^{(\ell)}) = \begin{cases} \left(\dfrac{\tau_{cw}}{\tau_{cr,e}^{(\ell)}} - 1\right) & \text{if } \tau_{cw} > \tau_{cr,e}^{(\ell)} \\ 0 & \text{if } \tau_{cw} \leqslant \tau_{cr,e}^{(\ell)} \end{cases} \tag{4.18}$$

$$F(\tau_{cw}, \tau_{cr,d}^{(\ell)}) = \begin{cases} \left(1 - \dfrac{\tau_{cw}}{\tau_{cr,d}^{(\ell)}}\right) & \text{if } \tau_{cw} < \tau_{cr,d}^{(\ell)} \\ 0 & \text{if } \tau_{cw} \geqslant \tau_{cr,d}^{(\ell)} \end{cases} \tag{4.19}$$

The calculated erosion or deposition flux is then applied to the near bottom computational cell by setting the appropriate sink and source terms for that cell.

For **non-cohesive sediment** fractions, sediment is incorporated in the water column by imposing a reference concentration at the reference height (van Rijn, 1993). The transfer of sediment between the bed and the flow is modelled using sink and source terms acting on the near-bottom layer that is entirely above Van Rijn's reference height, which is treated as suspended load. This layer is identified as the reference layer and referred to as the *kmx*-layer. Its height is given by

$$\delta_a = \min\left[\max\left(\alpha K_s, \frac{\Delta r}{2}, 0.01h\right), 0.2h\right] \tag{4.20}$$

in which δ_a is the van Rijn's reference height, α is the user-defined proportionality factor, K_s is the user-defined current-related effective roughness height, Δr is the wave-induced ripple height, and h is the water depth.

The sediment concentrations in the layers that lie below the *kmx*-layer are assumed to rapidly adjust to the same concentration as the reference layer. Each half time-step the source and sink terms model the quantity of sediment entering the flow due to upward diffusion from the reference layer and the quantity of sediment dropping out of the flow due to sediment settling. A sink term is

solved implicitly in the advection-diffusion equation, whereas a source term is solved explicitly. In order to determine the required sink and source terms for the *kmx*-layer, the concentration and concentration gradient at the bottom of the *kmx*-layer need to be approximated. A standard Rouse profile is assumed between the reference level δ_a and the centre of the *kmx*-layer

$$c^{(\ell)} = c_a^{(\ell)} \left[\frac{\delta_a (h - z)}{z(h - \delta_a)} \right]^{A^{(\ell)}} \tag{4.21}$$

in which $c^{(\ell)}$ is the concentration of sediment fraction (ℓ), $c_a^{(\ell)}$ is the reference concentration of sediment fraction (ℓ), z is the elevation above the bed, and $A^{(\ell)}$ is the Rouse number.

The reference concentration is calculated according to van Rijn et al. (2000) as

$$c_a^{(\ell)} = 0.015 \rho_s^{(\ell)} \frac{d_{50}^{(\ell)} {\tau_{*a}^{(\ell)}}^{1.5}}{\delta_a {d_*^{(\ell)}}^{0.3}} \tag{4.22}$$

where τ_{*a} is the non-dimensional bed shear stress and d_* is the non-dimensional particle diameter. The formula for each one of them is given as it follows:

$$\tau_{*a}^{(\ell)} = \frac{f_c^{(\ell)} \tau_{b,cw} + f_w^{(\ell)} \tau_{b,w} - \tau_{cr}^{(\ell)}}{\tau_{cr}^{(\ell)}} \tag{4.23}$$

$$d_*^{(\ell)} = d_{50}^{(\ell)} \left[\frac{(s^{(\ell)} - 1) g}{\nu^2} \right]^{1/3} \tag{4.24}$$

where f_c, f_w are friction factors due to currents and waves respectively, $\tau_{b,cw}$ is the bed shear stress due to current in the presence of waves, $\tau_{b,w}$ is the bed shear stress due to waves, and τ_{cr} is the critical bed shear stress. The three bed shear stresses are defined as

$$\tau_{b,cw} = \rho u_*^2 \tag{4.25}$$

$$\tau_{b,w} = \frac{1}{2} \rho f_w U_{orb}^2 \tag{4.26}$$

$$\tau_{cr} = (\rho_s - \rho) g d_{50} \theta_{cr} \tag{4.27}$$

$$U_{orb} = \frac{1}{2} \frac{\pi^{1.5} H_{rms}}{T \sinh(2kh)} \tag{4.28}$$

where θ_{cr} is the critical Shields parameter, U_{orb} is the near-bed orbital velocity and H_{rms} is the root-mean-square wave height.

The erosive and deposition fluxes of sediment through the bottom of the *kmx*-

layer are given by

$$E^{(\ell)} = \left\langle \varepsilon_s^{(\ell)} \frac{\partial c^{(\ell)}}{\partial z} \right\rangle_{bottom} \approx \varepsilon_s^{(\ell)} \frac{\alpha_1^{(\ell)} (c_a^{(\ell)} - c_{kmx}^{(\ell)})}{\Delta z} \tag{4.29}$$

$$D^{(\ell)} = \left\langle w_s^{(\ell)} c_{kmx}^{(\ell)} \right\rangle_{bottom} \approx w_s^{(\ell)} \alpha_2^{(\ell)} c_{kmx}^{(\ell)} \tag{4.30}$$

where the equations are evaluated at the bottom of the kmx-layer and approximated as the average concentration of the kmx-cell (c_{kmx}) by a correction factor (α).

For the work to be presented in the next chapters, a 2-DH model has been applied, which means that $z_{kmx} = h/2$ in Equation (4.21). According to Equation (4.20), δ_a cannot be larger than $0.2h$; therefore, c_{kmx} can be taken as

$$c_{kmx} \leqslant c_a 0.25^A \tag{4.31}$$

Typical values for the Rouse number (A) are given in Table 4.1 (after van Rijn (1993)), and therefore Equation (4.31) becomes

$$c_{kmx} \leqslant 0.0625 c_a \tag{4.32}$$

Table 4.1: Typical Rouse number values in sediment transport.

A	sediment transport mode
5	bedload ($z < 0.1h$)
2	suspended load ($z < 0.5h$)
1	suspended load ($z < h$)
0.1	wash load

4.1.4 Bedload sediment transport

Bedload transport is calculated for all non-cohesive sediment fractions according to the following approach: (1) the magnitude and direction of the bedload transport at the cell centres are computed using a transport formula; (2) the transport rates at the cell interfaces are determined and corrected for bed-slope effect, bed composition and sediment availability. In this work, a formula that includes the effect of waves in the bedload transport was used (van Rijn, 1993). The sediment transport below the reference height δ_a is treated as bedload transport.

For simulations including waves the magnitude and direction of the bedload transport on a horizontal bed are calculated using an approximation method developed by van Rijn (2003). The method computes the magnitude of the bedload

transport as

$$|S_b| = 0.006\rho_s w_s d_{50}^{(\ell)} M_s^{0.5} M_e^{0.7} \tag{4.33}$$

in which S_b is the bedload transport, M_s is the sediment mobility number due to waves and currents, and M_e is the excess sediment mobility number. The mobility parameters are given by

$$M_s = \frac{U_{eff}^2}{(s-1)gd_{50}} \tag{4.34}$$

$$M_e = \frac{(U_{eff} - U_{cr})^2}{(s-1)gd_{50}} \tag{4.35}$$

$$U_{eff} = \sqrt{U_R^2 + U_{on}^2} \tag{4.36}$$

in which U_{cr} is the critical depth averaged velocity for initiation of motion, U_R is the magnitude of an equivalent depth-averaged velocity computed from the velocity in the bottom computational layer, assuming a logarithmic velocity profile. U_{on} is the near-bed peak orbital velocity in onshore direction, whereas U_{off} (introduced later) is its homonym in offshore direction.

The direction of the bedload transport vector is determined in a rather more complex way. It is composed of two parts: part due to current ($S_{b,c}$) which acts in the direction of the near-bed current, and part due to waves ($S_{b,w}$) which acts in the direction of wave propagation. These components are determined as

$$S_{b,c} = \frac{S_b}{\sqrt{1 + r^2 + 2|r|\cos\varphi}} \tag{4.37}$$

$$S_{b,w} = r|S_{b,c}| \tag{4.38}$$

$$r = \frac{(|U_{on}| - U_{cr})^3}{(|U_R| - U_{cr})^3} \tag{4.39}$$

where φ is the angle between current and wave direction for which van Rijn (2003) suggests a constant value of 90°.

An estimation of the suspended sediment transport due to wave asymmetry effects is also included in the bedload transport vector. This is intended to model the effect of asymmetric wave orbital velocities on the transport of suspended material within about 0.5 m of the bed, which is the bulk of the suspended transport affected by high frequency wave oscillations. This wave-related suspended sediment transport is modelled using an approximation method proposed by van

Rijn (2001)

$$S_{s,w} = \alpha \lambda U_A q_s \tag{4.40}$$

$$U_A = \frac{U_{on}^4 - U_{off}^4}{U_{on}^3 + U_{off}^3} \tag{4.41}$$

$$q_s = 0.007 \rho_s d_{50} M_e \tag{4.42}$$

in which $S_{s,w}$ is the wave-related suspended transport, α is an user-defined tuning parameter, λ is the phase lag coefficient ($= 0.2$), U_A is the velocity asymmetry value, and q_s is the suspended sediment load.

The three separate transport modes are imposed separately. The direction of the bedload due to currents $S_{b,c}$ is assumed to be equal to the direction of the current, whereas the two wave related transport components $S_{b,w}$ and $S_{s,w}$ take on the wave propagation direction. This results in the following transport components:

$$S_{b,c,u} = \frac{u_b}{|U_b|}|S_{b,c}| \qquad S_{b,c,v} = \frac{v_b}{|U_b|}|S_{b,c}| \tag{4.43}$$

$$S_{b,w,u} = S_{b,w} \cos\vartheta \qquad S_{b,w,v} = S_{b,w} \sin\vartheta \tag{4.44}$$

$$S_{s,w,u} = S_{s,w} \cos\vartheta \qquad S_{s,w,v} = S_{s,w} \sin\vartheta \tag{4.45}$$

in which ϑ is the local angle between the direction of wave propagation and the computational grid.

4.2 Energy analysis due to meteorology

The meteorological forcing is an important component to process-based models. Differences in air pressure between two points on the surface produce a gradient in the water level, and wind fields transfer motion to the water surface. The analysis of the amount of energy enables a rough estimation of how much input from this driving force is transferred to the model.

The wave-induced potential energy (PE) in the entire column, from bottom to surface, is equal to the potential energy in the presence of the wave minus the potential energy in the absence of the wave. If the tidal wave is considered as the primary driving force, and the meteorological input is a perturbation of that wave, then the following relation can be applied, averaged over one period per

unit surface area:

$$\mathrm{PE} = \overline{\int_0^{\eta} \rho g z \, \mathrm{d}z} = \overline{\tfrac{1}{2}\rho g \eta^2} \tag{4.46}$$

The definition of kinetic energy (KE) is more straightforward and is calculated directly with the velocity magnitude. The time-averaged kinetic energy is then given by

$$\mathrm{KE} = \overline{\int_{-h}^{\eta} \tfrac{1}{2}\rho U^2 \, \mathrm{d}z} = \overline{\tfrac{1}{2}\rho (h+\eta) U^2} \tag{4.47}$$

Finally, the total energy (TE) in the simulations has been calculated by summing the wave-induced potential energy and the kinetic energy from currents, i.e. $\mathrm{TE} = \mathrm{PE} + \mathrm{KE}$. The estimation of the contribution from meteorological forcing is then estimated by simulating the same period with and without it, and finally by calculating its ratio. In mathematical terms, it can be written as

$$\mathrm{R}_m = 1 - \frac{\mathrm{TE}_t}{\mathrm{TE}_{t+m}} \tag{4.48}$$

where R_m is the energy ratio due to the meteorological component, TE_t is the total energy from the simulation only with tidal forcing and TE_{t+m} is the total energy from the simulation with tidal and meteorological forcing.

4.3 Ensemble simulation

4.3.1 Definition

The term "ensemble forecast" is commonly used in atmospheric sciences in reference to a numerical weather prediction method. The solution to stochastic dynamic equations by approximating them through Monte Carlo Simulation (MCS) methods is known as *ensemble forecasting*. Multiple simulations are conducted to account for two usual sources of uncertainty in forecast models: (1) errors introduced by the use of imperfect initial conditions, amplified by the chaotic nature of the evolution equations of the dynamical system, which is often referred to as sensitive dependence on the initial conditions; and (2) errors introduced because of imperfections in the model formulation, such as the approximate mathematical methods to solve the equations. Ideally, the verified future dynamical system state should fall within the predicted ensemble spread, and the amount of spread should be related to the uncertainty (error) of the forecast.

The ensemble forecasting concept is presented in Figure 4.2. The ensemble forecast procedure begins in principle by defining a finite sample from the

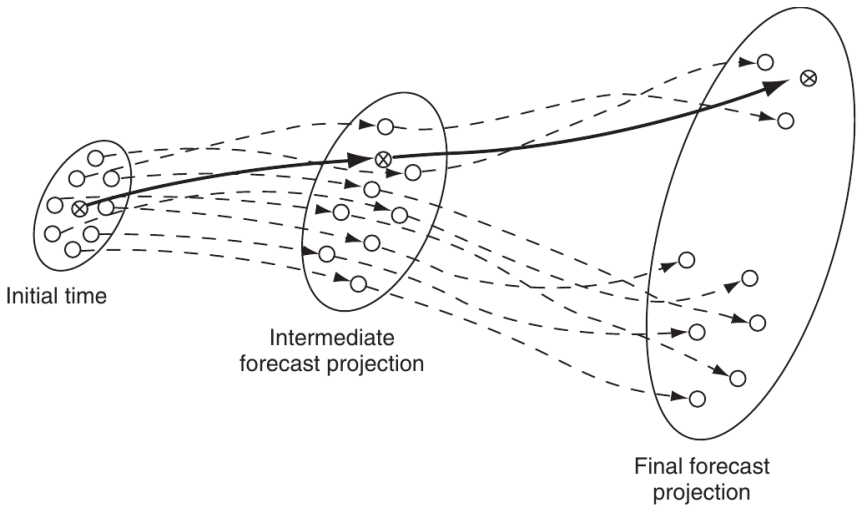

Figure 4.2: Schematic illustration of ensemble forecasting concepts. (Wilks, 2006)

probability distribution that describes the uncertainty of the initial state of the atmosphere. A few members of the point cloud surrounding the mean estimated atmospheric state in phase space are chosen randomly. Together these points are called the ensemble of initial conditions, and each one represents a plausible initial state of the atmosphere consistent with the uncertainties in observation and analysis. Each of the points in the initial ensemble provides the initial conditions for a separate simulation. At the initial time, all the ensemble members are very similar to each other; however, in the final projections the trajectories diverge drastically. The underlying distribution of uncertainty that was fairly small at the initial time has been stretched substantially, as represented by the large ellipse at the time of the final projection. The dispersion of the ensemble members at that time allows the nature of that distribution to be estimated, and is indicative of the uncertainty of the forecast, assuming that the model includes only negligible errors in the representations of the governing physical processes. If only a single forecast started from the best initial condition had been made, this information would not be available.

The concept of ensemble forecasting is applied to morphodynamic simulations in order to deal with similar kinds of uncertainties: (1) errors related to the estimation/calibration of sediment transport parameters; and (2) errors due to imperfections in the model formulations and approximations.

A spatial field such as the bathymetry of coastal areas can be represented by a finite vector

$$\mathbf{x} = \begin{pmatrix} x_1 & x_2 & \dots & x_p \end{pmatrix} \tag{4.49}$$

defined by values of the field at p points on a spatial grid. The vector x is

therefore a finite p-dimensional representation of a continuum field and is a good approximation for spatially smooth fields. An ensemble with n members of a spatial map can be represented by the $(n \times p)$ rectangular data matrix

$$\mathbf{X} = \begin{pmatrix} \mathbf{x_1} \\ \mathbf{x_2} \\ \vdots \\ \mathbf{x_n} \end{pmatrix} = \begin{pmatrix} x_{11} & x_{12} & \dots & x_{1p} \\ x_{21} & x_{22} & \dots & x_{2p} \\ \vdots & \vdots & & \vdots \\ x_{n1} & x_{n2} & \dots & x_{np} \end{pmatrix} \tag{4.50}$$

where the kth row, $\mathbf{x_k}$, is the kth estimation in the ensemble. Typically in meteorological applications, the number of members in the ensemble (n) is of the order of $10^1 - 10^2$, whereas the size of the vectors (p) is of the order of $10^3 - 10^7$ (Stephenson and Doblas-Reyes, 2000).

Therefore, the ensemble mean $(\overline{\mathbf{x}})$ at each grid point is given by

$$\overline{\mathbf{x}} = \frac{1}{n} \sum_{k=1}^{n} \mathbf{x_k} \tag{4.51}$$

and the natural measure of the ensemble spread is given by the ensemble standard deviation $(\mathbf{s})$

$$\mathbf{s}^2 = \frac{1}{n} \sum_{k=1}^{n} (\mathbf{x_k} - \overline{\mathbf{x}})^2 \tag{4.52}$$

4.3.2 Application to morphodynamic models

The uncertainties related to sediment characteristics and its transport have been discussed in Chapter 2. By combining that information with the concepts presented in the last section, the application of ensemble simulations to morphodynamic models can be done.

Schmelter et al. (2011, 2012) presented the application of Bayesian statistics to a simple sediment transport model in order to provide a probabilistic prediction of sediment discharges. They concluded that the Bayesian approach provides a robust way to quantify uncertainty and then propagate it through to subsequent analyses.

Fortunato et al. (2009) considered uncertainties in sediment transport parameters and analysed model results as a morphodynamic ensemble. They proposed the Confidence Index, an index similar to the Brier Skill Score that takes the standard deviation in space into account. They concluded that ensemble simulations can be applied to modelling of long-term evolution of tidal inlets, in order to consider uncertainties related to various error sources.

The concept of ensemble simulations has been applied to morphodynamic

models in a simple way, based on the aforementioned methods. The ensemble of initial conditions in Figure 4.2 is now defined as the initial bathymetry together with sediment transport model parameters that are slightly different from each other. This small difference, however, is considered to produce significant morphodynamic changes in a morphological time scale.

Similarly to Fortunato et al. (2009) and Schmelter et al. (2011, 2012), it has been assumed that the sediment transport model uncertainties can be represented by a small deviation in each parameter value. In order to simulate this deviation, a Gaussian probability distribution is assumed for each sediment transport model parameter that is considered to contribute to the model uncertainty. The mean is assumed to be equal to a previously estimated/calibrated parameter value and the standard deviation represents the parameter uncertainty. The ensemble members can, therefore, be determined by sampling n random values from a probability distribution, which is defined the selected mean and standard deviation.

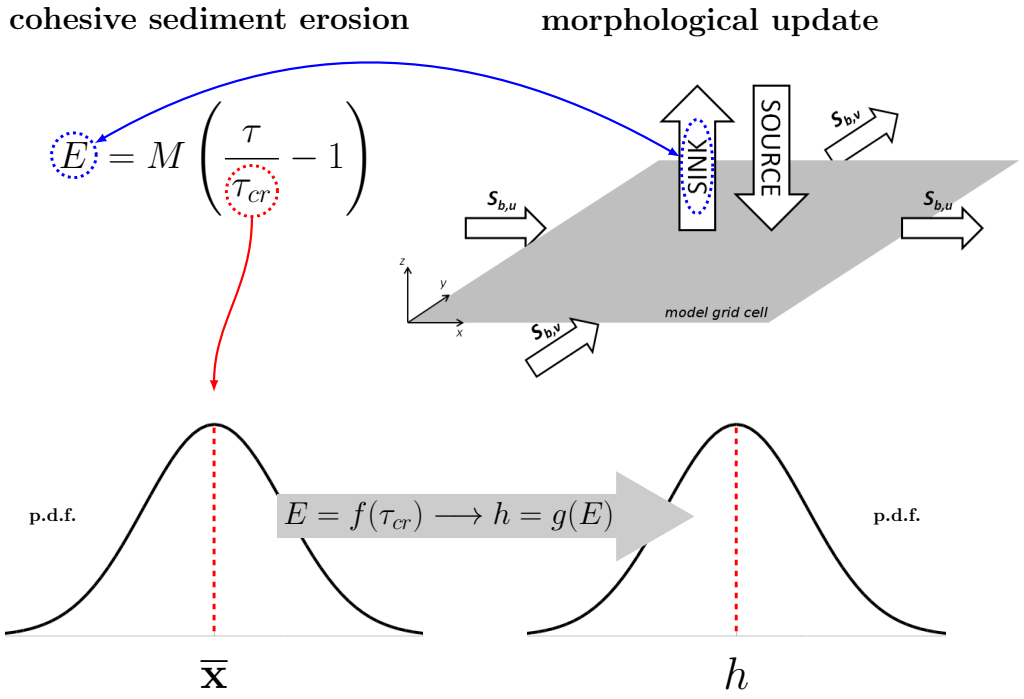

Figure 4.3: Application of the ensemble concept to morphodynamic models.

Figure 4.3 illustrates the concept of a morphodynamic ensemble simulation. In this example, the critical shear stress of cohesive sediment affects the sink term from the seabed, given by equation (4.16) after Partheniades (1965).

The critical shear stress (τ_{cr}) is a constant value that represents the threshold for erosion that takes place in the seabed. In Delft3D it is a model parameter defined for each sediment type. However, such a threshold cannot be precisely

measured, as shown by Barnes and Baldock (2007), Darby and Sear (2008) and Barnes et al. (2009). The last authors even stated that in the surf and swash zone "Eulerian estimates of bed shear stress or transport rates are unlikely to be robust indicators of net sediment transport gradients and morphological change". In order to take this uncertainty into account, the chosen parameter was considered to have a mean value with a certain deviation, represented by a Gaussian distribution. Because the seabed changes depend on the aforementioned sink term, the set of results will also follow a probability distribution.

Not only the critical shear stress has been considered to contribute to model uncertainty, but the sediment settling velocity (w_s) and the median grain size (d_{50}) as well. In the literature these parameters have been studied by Winterwerp et al. (2006), Darby and Sear (2008) and Soulsby et al. (2013). The three aforementioned parameters have been chosen, because they have been identified as possible contributors to the uncertainty in sediment transport calculations and, therefore, in morphodynamic evolution.

The simulation results are then evaluated based on statistics derived from Equations (4.51) and (4.52). For example, the final bathymetry is represented by the ensemble mean ($\overline{\mathbf{x}}$) and its uncertainty is represented by the ensemble spread ($\mathbf{s}$). In the next section, performance indexes from the morphodynamic ensemble are presented.

4.4 Model performance and statistics

The quantitative evaluation of model performance is proposed by van Rijn et al. (2003) on the basis of the Relative Mean Absolute Error (RMAE) and the Brier Skill Score (BSS). According to the authors, the RMAE is preferred above the Relative Mean Square Error (RMSE), because the first one is less susceptible to the presence of outliers. Relative errors can be obtained by scaling the error with the average of the measured value. The relative errors will be relatively large, if the average value is close to zero (such as for a tidal current varying around zero). In this case the RMAE can give very high values that are exceptionally sensitive to small perturbations in the average. Therefore, it is better to non-dimensionalise the errors by the average of the absolute measured values. The RMAE of hydrodynamic quantities is then defined as

$$\mathrm{RMAE} = \frac{\overline{|Y - X|} - \Delta X}{\overline{|X|}} \tag{4.53}$$

where X is the set of measurements (e.g. current velocity, water level, wave height) and Y is the set of computed values by the model. ΔX stands for the

measurement error, being equal to 0.1 m for wave height and 0.05 m s^{-1} for current velocity.

The BSS is commonly used in meteorology for verification of probabilistic forecasts, but only since the beginning of the 2000's it has been applied to morphodynamic modelling. This skill score compares the mean square difference between prediction and observation with the mean square difference between baseline prediction and observation. Perfect agreement gives a score of 1, whereas modelling the baseline condition gives a score of 0. If the model prediction is further away from the final measured condition than the baseline prediction, the score is negative. This makes the BSS very suitable for the prediction of bed evolution, and Sutherland et al. (2004) suggested its use for coastal engineering applications. The BSS of bed level evolution is defined (van Rijn et al., 2003) as

$$\mathrm{BSS} = 1 - \frac{\overline{(|Y - X| - \Delta X)^2}}{\overline{(X_0 - X)^2}} \tag{4.54}$$

where X_0 is set of measurements of the initial bathymetry (reference), X is the set of measurements of final bathymetry and Y is the set of predictions of final bathymetry. ΔX stands for the measurement error of bed level, considered to be 0.1 m.

A limitation of the BSS is that it cannot account for the migration direction of a bar or a channel. It just evaluates whether the computed bed level (at time t) is closer to the measured bed level than the initial bed level. If the computed bar/channel migration is in the wrong direction, but relatively small, this may result in a higher BSS compared to the situation with bar/channel migration in the right direction, but much too large.

The qualification of model performance suggested by van Rijn et al. (2003) is given in Table 4.2.

Table 4.2: Qualification of error ranges of process parameters.

qualification	wave height RMAE	current velocity RMAE	morphology BSS
excellent	< 0.05	< 0.1	1.0 - 0.8
good	0.05 - 0.1	0.1 - 0.3	0.8 - 0.6
reasonable/fair	0.1 - 0.2	0.3 - 0.5	0.6 - 0.3
poor	0.2 - 0.3	0.5 - 0.7	0.3 - 0.0
bad	> 0.3	> 0.7	< 0.0

Confidence and Skill

In order to evaluate the model outcome uncertainty from an ensemble simulation, Fortunato et al. (2009) have come out with an aggregate index to assess the overall uncertainty of the model. Based on the concepts of the Brier Skill Score (Sutherland et al., 2004), an index for measuring the skill of morphodynamic models, a more compact measure of uncertainty is obtained by aggregating the standard deviation σ in space and making it dimensionless. This index, called Confidence Index (CI), is unity when there is no uncertainty, and decreases with increasing uncertainty. When the CI is zero, the uncertainty is of the same order as the depth changes predicted by the model, and this implies that the predictions are useless.

Based on the concept of Fortunato et al. (2009), van der Wegen and Jaffe (2013) defined a homonymous index to assess the level of uncertainty of model results; additionally, they defined the Skill Index (SI) to assess the model skill based on the BSS. First, the ensemble mean ($\overline{\mathbf{x}}_{\boldsymbol{\Delta}}$) and standard deviation ($\mathbf{s}_{\boldsymbol{\Delta}}$) of the modelled bed level changes in a grid cell are defined, analogously to Equations (4.51) and (4.52), as

$$\overline{\mathbf{x}}_{\boldsymbol{\Delta}} = \frac{1}{n}\sum_{k=1}^{n}\Delta h_k \tag{4.55}$$

$$\mathbf{s}_{\boldsymbol{\Delta}}{}^2 = \frac{1}{n}\sum_{k=1}^{n}(\Delta h_k - \overline{\mathbf{x}}_{\boldsymbol{\Delta}})^2 \tag{4.56}$$

in which Δh_k represents the modelled bed level change of a particular ensemble member.

The CI is then given by

$$\mathrm{CI} = 1 - \frac{\mathbf{s}_{\boldsymbol{\Delta}}{}^2}{\overline{\mathbf{x}}_{\boldsymbol{\Delta}}{}^2_{abs}} \tag{4.57}$$

in which $\overline{\mathbf{x}}_{\boldsymbol{\Delta}abs}$ is used to correct for low mean values as a result of both positive and negative realizations:

$$\overline{\mathbf{x}}_{\boldsymbol{\Delta}abs} = \frac{1}{n}\sum_{k=1}^{n}|\Delta h_k| \tag{4.58}$$

The SI differs from the BSS, because it considers a local (grid cell) value, whereas the BSS considers a domain averaged score. It is given by

$$\mathrm{SI} = 1 - \frac{(\overline{\mathbf{x}}_{\boldsymbol{\Delta}} - \Delta h_{meas})^2}{\Delta h_{meas}^2} \tag{4.59}$$

in which Δh_{meas} is the measured bed level change.

An important characteristic of the CI is that it is not affected by the inclusion of an additional inactive area to the domain, for where the bathymetry does not change, $\mathbf{s_\Delta}$ is zero and $\overline{\mathbf{x}}_{\mathbf{\Delta}abs}$ is also zero. As for the SI, the limiting factor in such analysis, as well as in the BSS, is that enough measurements within the model grid area are necessary so that the skill can be calculated in a satisfactory number of grid cells. The BSS is usually presented as an average single value, which assumes that the model performs similarly in space. The SI, on the other hand, is already an index composed by results from several models and should be analysed spatially.

The indexes presented in this section are related to two different concepts: *accuracy* and *precision*. The term *accuracy* describes systematic errors, a measure of statistical bias. It is used to describe the closeness of a measurement to the true value, and may be related to the SI. The term *precision* describes random errors, a measure of statistical variability. It is the closeness of agreement among a set of results, and may be related to the CI.

Chapter 5

Numerical model set-up

The set-up of the numerical model presented in Chapter 4 will be now described. First, model domain, nesting and driving forces are presented. Then, the hydrodynamic model set-up and calibration are described in detail. At last, the sediment transport model set-up and the sensitivity analysis on sediment transport model parameters are presented.

5.1 Model domain

The model area is numerically defined in a staggered grid in Delft3D, as presented in Section 4.1.1. For the study area a curvilinear grid within the Dithmarschen Bight was used, called from now on as the MDPI Model (MDPIM). It has dimensions of about 27 km along the western open boundary, about 33 km on the east-west axis, and ca. 42,000 cells with resolution varying between over 600 m on the boundaries down to almost 30 m near the MDPI, all summing up ca. 1000 km^2.

A first version of the MDPIM was developed and applied by Nguyen et al. (2010) and later improved by Nguyen (2015) to the actual geometry. Figure 5.1 shows the location and geometry of the actual MDPIM grid applied in the present study, represented in coarser resolution for better visualization purpose.

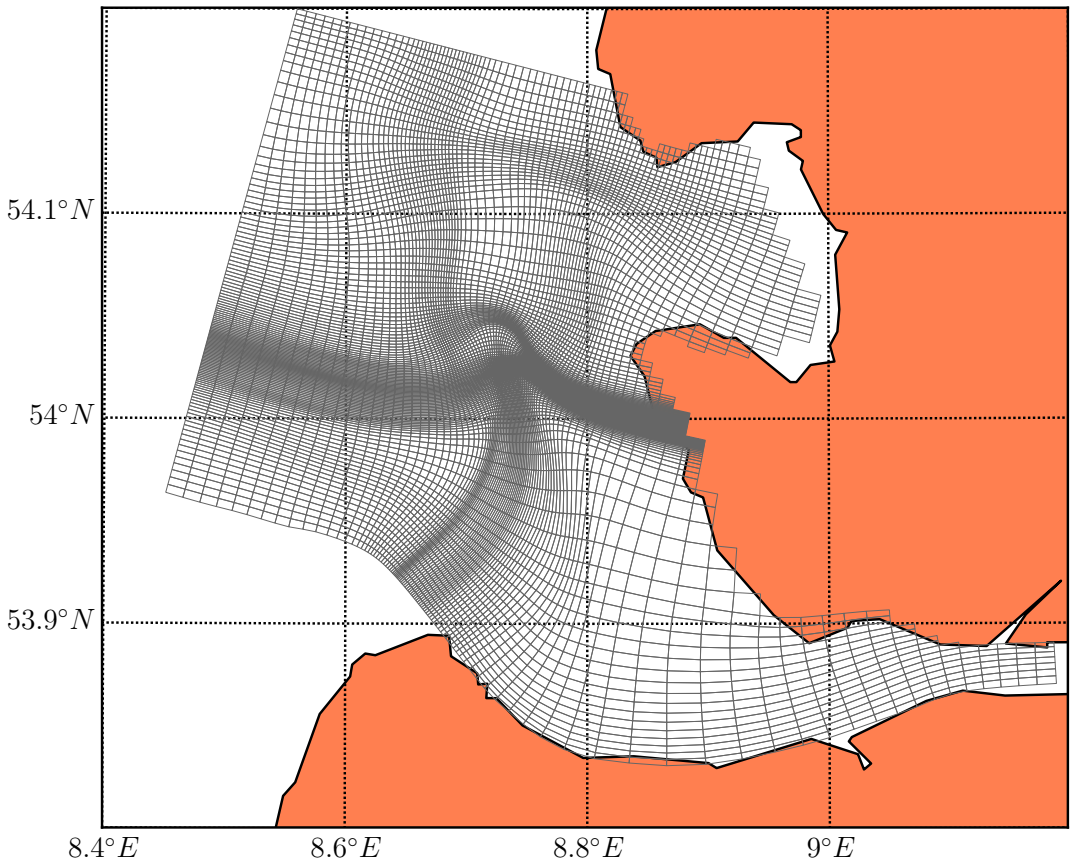

Figure 5.1: The MDPIM grid.

5.2 Model nesting

The MDPIM open boundaries are driven by water level and wave spectrum data. This information can be provided by nesting the model in a larger one from which the information is extracted at the boundary grid points. The larger model is the German Bight Model (GBM) developed by Deltares and later improved within the PROMORPH project (Mayerle and Zielke, 2005). The computational grid covers the whole German Bight area with more than 35,000 cells and its resolution varying between almost 2000 m (offshore) down to about 700 m (onshore) and less than 300 m at river upstream. However, the GBM also requires water level boundary conditions that are not well represented only by tide. That means it must be also nested into a larger model, the Continental Shelf Model (CSM). The CSM was developed by Verboom et al. (1992) and covers the Northwest European Continental Shelf. It contains about 20,000 cells with resolution between 7.7 km and 9.2 km. The full nesting sequence is shown in Figure 5.2.

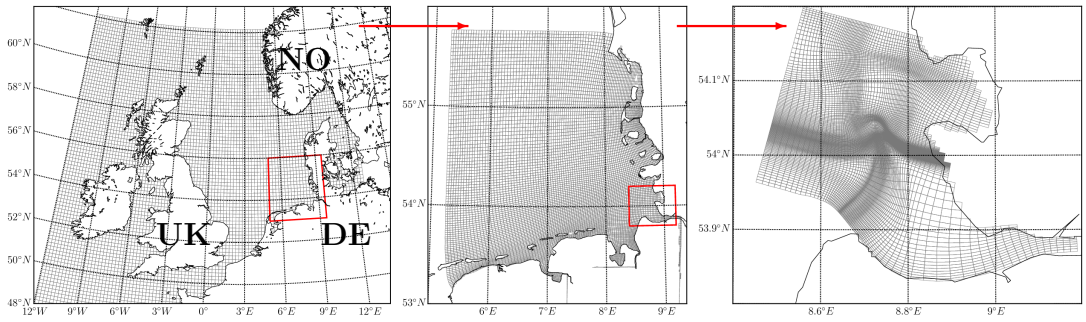

(a) CSM (b) GBM (c) MDPIM

Figure 5.2: Nesting sequence from the CSM to the MDPIM.

5.3 Model driving forces

A hydrodynamic model can be set in motion mainly by three types of forcing: (1) gravitational, (2) pressure and (3) shear stress. The first type refers to tides and river flow discharges; it is the source of potential energy due to gradients in the free water surface. The second type is related to differences in air pressure between two points on the surface, producing a gradient in the water level. The third type refers to the transfer of motion to the water surface by wind fields.

The CSM is only driven by tidal forcing at the open boundaries and meteorological forcing on the free surface. The GBM is driven by water level time series (provided by the CSM) at the open boundaries and by meteorological forcing on the free water surface. Within the GBM domain, all the waves are considered to be generated (by the wind) and then propagated into the Dithmarschen Bight. The MDPIM has three open sea boundaries (N, W, S) where water level and two-dimensional wave spectrum boundary conditions are imposed, and one open boundary at the Elbe river (E) where only with water level boundary conditions (all provided by the GBM).

Tide

In the CSM, the astronomical constituents along the open sea boundaries are represented at each boundary grid point by 12 constituents (M_2, S_2, N_2, K_2, K_1, O_1, Q_1, P_1, MF, MM, M_4 and MS_4) obtained from the Global Model of Ocean Tides (Egbert and Bennet, 1994; Egbert and Erofeeva, 2002; TPXO, 2016).

Meteorological model

In this study data from the DWD's model was used to impose wind and pressure fields on the free surface of all hydrodynamic models. Two models are available from DWD: (1) a global model (GME) with a temporal resolution of 3 h and spatial resolution up to 40 km used for simulation periods earlier than 2008,

and (2) a regional model (COSMO) with a temporal resolution of 1 h and spatial resolution of 0.0625° (ca. 7 km) covering the whole CSM area, from 2008 up to now. For further information on the DWD meteorological models reference is made to Frank et al. (2014) (GME) and Schulz and Schättler (2014) (COSMO).

Table 5.1: Statistical analysis of meteorological data from DWD models.

DWD model	station	air pressure		wind speed		wind direction	
		RMAE	R	RMAE	R	RMAE	R
GME	Helgoland	0.001	0.997	0.182	0.565	0.135	0.741
	Norderney	0.001	0.996	0.315	0.385	0.131	0.802
	Sylt	0.001	0.997	0.192	0.572	0.124	0.786
	mean	0.001	0.997	0.230	0.507	0.130	0.776
COSMO	Helgoland	0.001	0.997	0.161	0.903	0.115	0.779
	Norderney	0.001	0.997	0.278	0.749	0.112	0.823
	Sylt	0.001	0.996	0.174	0.893	0.104	0.832
	mean	0.001	0.996	0.205	0.848	0.111	0.811

The statistical analysis of the data is presented in Table 5.1 for both global and regional models. The GME model has been analysed from 01.01.2000 to 01.06.2014, while the COSMO model from 03.11.2007 to 15.06.2015. The small error and high correlation for air pressure in both models are definitely good indicators of model performance. Air pressure is a much more steady physical quantity in space than wind field. It depends basically on altitude, humidity and temperature, whereas wind depends on air pressure, surface roughness, topography, etc. and as a consequence it is much more difficult to model. Therefore, errors are in the order of 20% for wind speed and 10% for wind direction on average for both models, but correlations finally prove that the regional model performs better. Yet, for the representation of atmospheric processes in space, numerical models are widely used and the best choice available.

5.4 Hydrodynamic model

As described in Section 5.3, the hydrodynamic model is driven by water level and wave spectrum time series at the open boundaries, and by air pressure and wind fields on its free surface. The driving forces on the open boundaries are obtained through the model nesting sequence, whereas the meteorological forcing is imposed directly taken from the meteorological model. Water level information is imposed every 12 minutes at every open boundary grid point, while hourly wave spectrum data is imposed at every 1 km along the model sea boundaries.

5.4.1 Waves

The simulation of waves in Delft3D is done by SWAN and can be coupled to the FLOW module, as described in Section 4.1.2. Several studies have been done in the vicinity of the MDPI previously (Wilkens, 2004; Escobar Sierra, 2007; Etri, 2007; Nguyen et al., 2010; Nguyen, 2015) and all of them have presented good results for wave simulations with SWAN. The wave model grid used for the calculations presents the same geometry as the MDPIM; however, its resolution is decreased by a factor of 3 in order to reduce computational time.

Because the waves generated inside the model grid domain depend on the meteorological forcing, wave accuracy depends directly on the meteorological forcing. That means, the resolution of the meteorological model in space and in time plays a very import role. For simulations up to 2008 the global model has been used, with resolution in space of ca. 40 km and in time of 3 h. For simulations done after that the regional model has been used, with resolution in space of ca. 7 km and in time of 1 h.

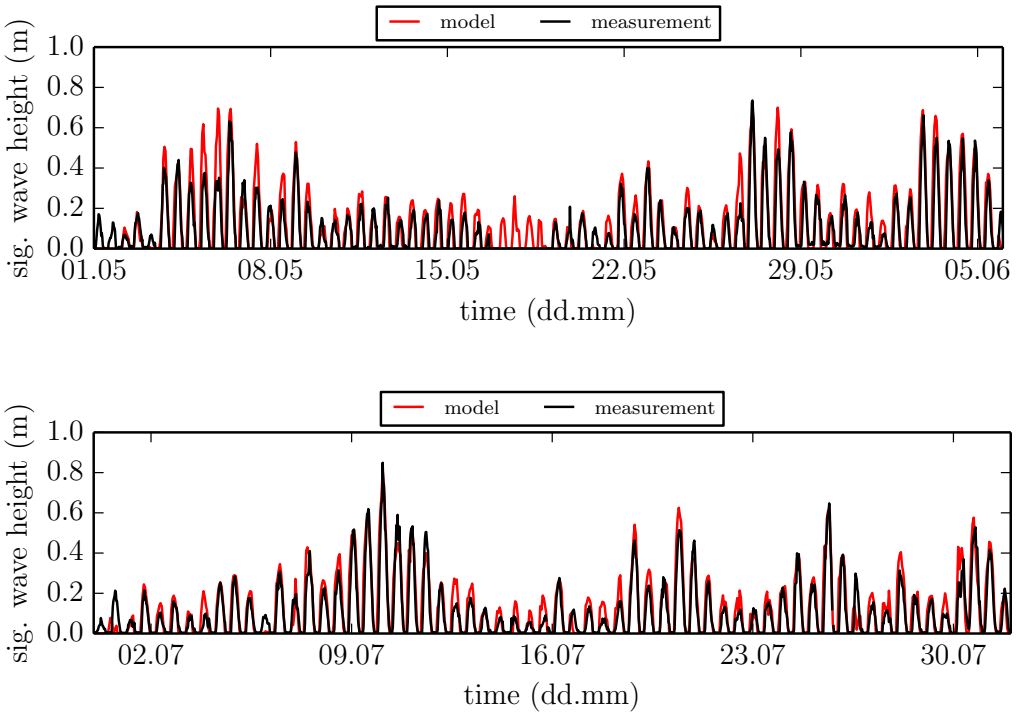

Figure 5.3: Significant wave height in 2009 at location W_1.

Figures 5.3 and 5.4 show the significant wave height at two locations close to the MDPI (see Figure 3.6). It can be seen that the wave model can simulate real conditions in the study area in a good way. The average RMAE and correlation are equal to 0.08 and 0.91 at location W_1, 0.12 and 0.82 at location W_2, respectively. According to Table 4.2, the model is qualified as *good* at W_1 and as *reasonable/fair* at W_2. The apparently lower model performance at location W_2

might be related to the measuring device (directional wave gauge), which possibly got interference from wave breaking and could not properly measure wave heights lower than 0.06 m (when the tidal flat gets dry).

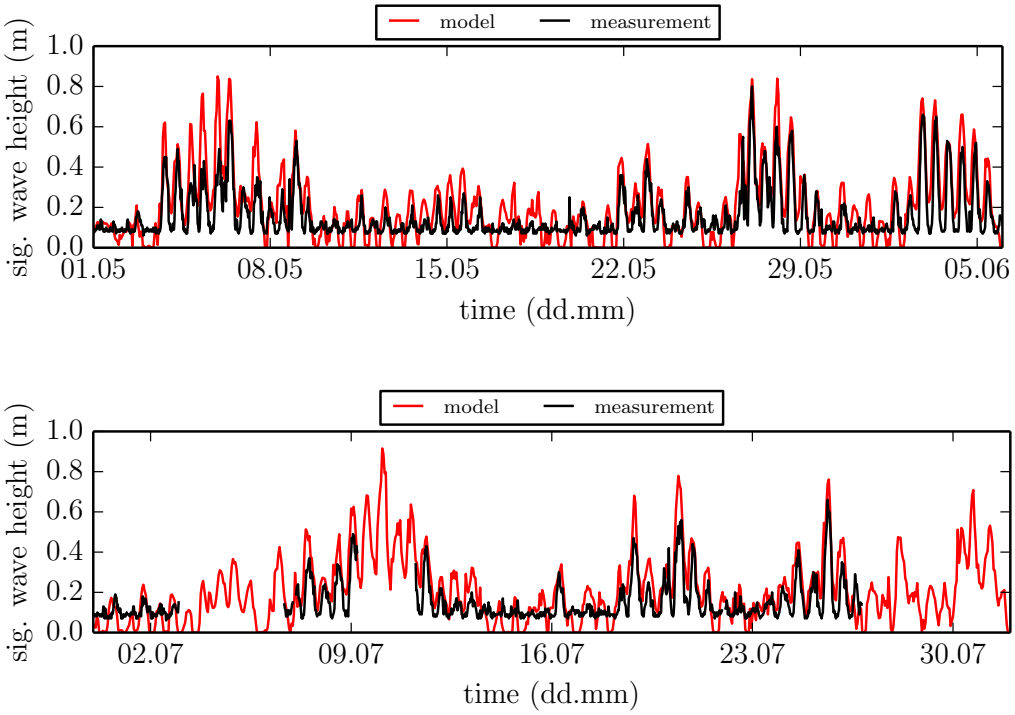

Figure 5.4: Significant wave height in 2009 at location W_2.

5.4.2 Calibration

The hydrodynamic model was calibrated on the basis of sensitivity tests and previous studies. Boundary condition types have been tested and it has been concluded that water level from nested models are the best option. The next step is then to set up the shear stresses on the free surface and on the model bed. On the free surface, the shear stress is transferred from the wind field and scaled by the wind drag coefficient. The model is not very sensitive to changes in this coefficient during normal weather conditions. On the model bed, the bed roughness represents the shear stress from the bottom and is also scaled by the Chézy coefficient. It was found that changes in bed roughness lead to the most significant variations in the hydrodynamic conditions. Thus, the model calibration was achieved by tuning this parameter.

In order to check the tidal forcing imposed on the sea boundaries of the CSM, the amplitude and phase of measurements and model have been compared by means of Fourier analysis of water level time series. Two tidal gauges have been selected, one in the GBM (Helgoland) and another in the MDPIM (Büsum), and

are presented in Figure 5.5. In both locations the tidal amplitude was reasonably well simulated by the model, while the phase was in general overestimated by ca. 10%. Although the MDPIM grid resolution is much higher than the GBM, the bathymetry of the Wadden Sea is very complex, which makes difficult the improvement of the numerical simulation of tidal propagation.

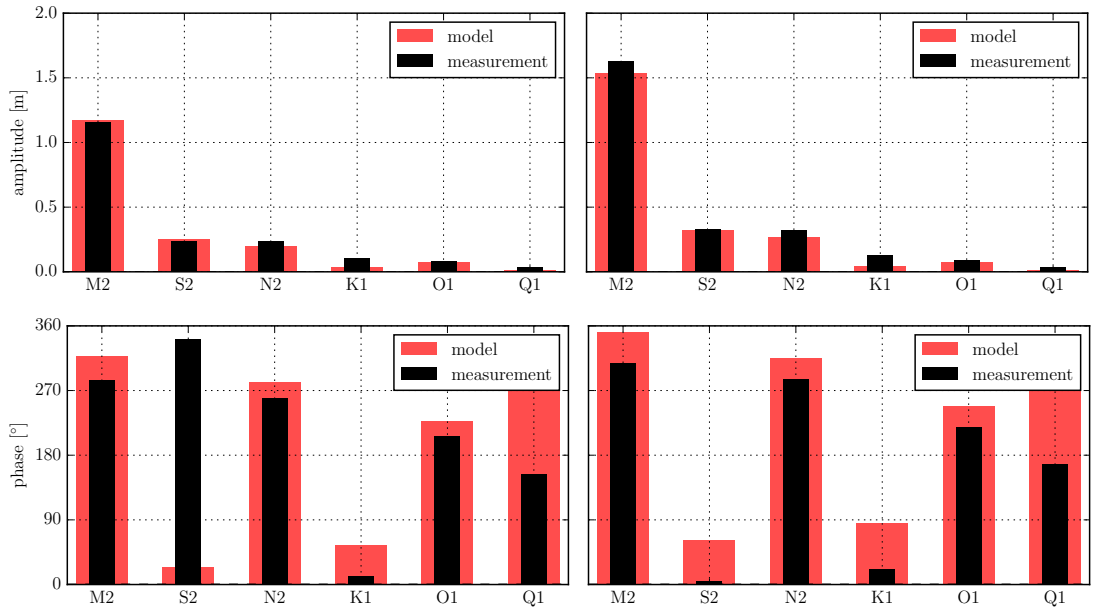

(a) Helgoland (b) Büsum

Figure 5.5: Tide analysis of water level time series: amplitude (top) and phase (bottom).

Because the bed roughness represents the friction effect produced by the bed in the flow, and therefore by the sediment that is found on it, attention should be given to its determination so that the sediment defined afterward matches the local roughness. A further complication is the variation in time of this property, which is not taken into account in Delft3D. The bed roughness has been tested by changing the Chézy roughness coefficient in the model. The range from rough ($C = 50$) to smooth ($C = 80$) uniform conditions, and also a spatially varying roughness condition have been simulated. For the spatially varying roughness calculation, a method adapted from Escobar Sierra (2007) was used. In this method, first the spatially varying median grain size is calculated based on bottom-induced wave currents, and then the roughness is determined according to van Rijn (1993), based on averaged flow conditions.

Results obtained for the median grain size match quite well Escobar's results, in the Piep system area (north of the MDPI). The sediment in the Piep channel system is composed by medium and fine sand, and an embedded layer of a consolidated mud. The coarser material in the channels cannot be predicted by the current method, because bottom-induced wave currents can only affect shal-

lower areas. Finally, the sediment availability in the channels will be modified to mimic the layer of consolidated material (presented in the next section). Figure 5.6 presents (a) the calculated median grain size d_{50} and (b) the Chézy roughness coefficient averaged from two simulated periods (summer and winter).

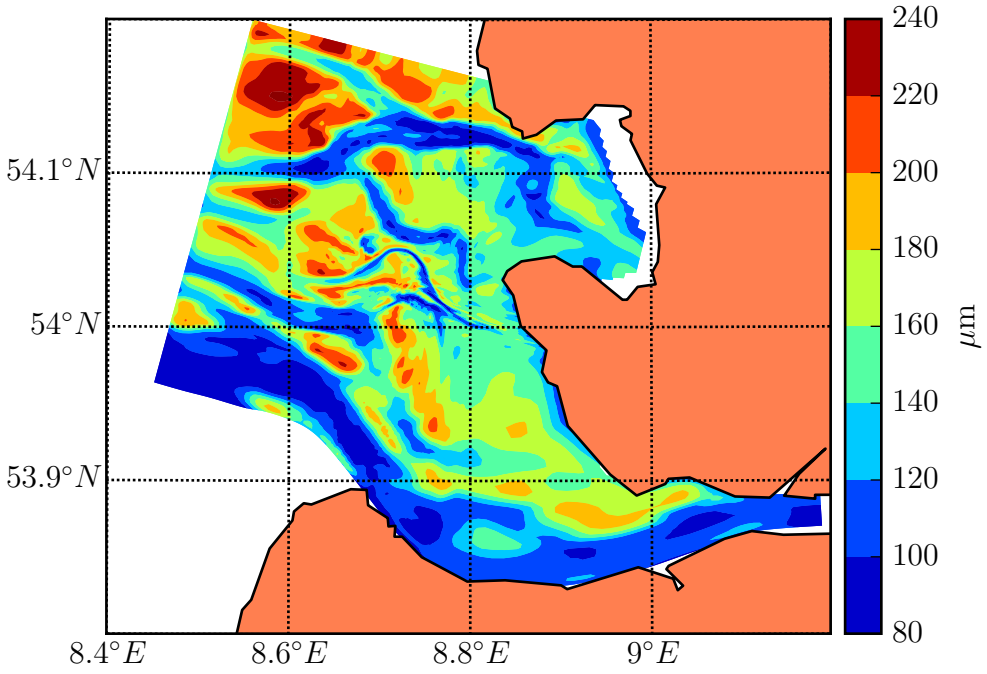

(a) median grain size

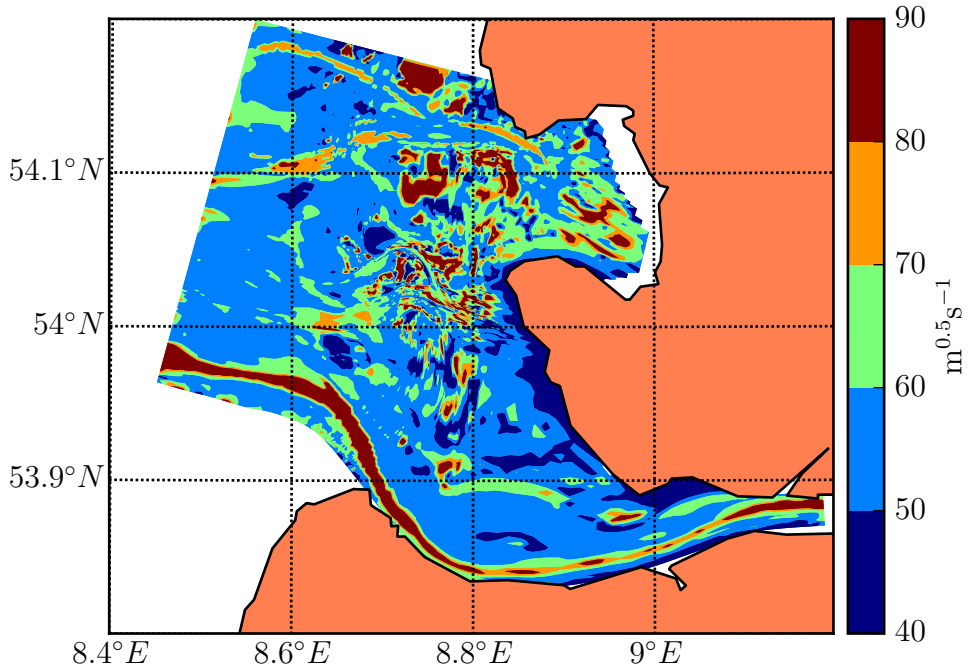

(b) Chézy roughness coefficient

Figure 5.6: Sediment related parameter set-up for the hydrodynamic model calibration.

The model performance was evaluated by means of comparison of water level at stations as well as current velocity along cross-sections. In total, 12 stations of water level and 6 stations of current velocity (u- and v-direction) during four different periods have been compared to model results. Information about the stations and periods are given in Table 5.2.

Table 5.2: Measurement stations used for calibration of the hydrodynamic model.

parameter	station	period
water level	Büsum, Norderpiep, Piep, Süderpiep	01.06.2000 - 07.06.2000
	Büsum, Flackstrom, Mittelplate, Trischen	01.10.2006 - 06.10.2006
	Büsum	18.02.2007 - 21.02.2007
	Flackstrom, Mittelplate, Trischen	15.06.2009 - 02.07.2009
current velocity	Norderpiep, Piep, Süderpiep	01.06.2000 - 07.06.2000
	C_2	18.02.2007 - 21.02.2007
	C_3, C_4	15.06.2009 - 02.07.2009

In Table 5.3 the averaged RMAE from all stations is presented. Although the results from water level show that a model with higher Chézy coefficient (lower roughness) performs better, the v-velocity is not as well represented as in a model with a rougher bed. Results from the u-velocity point out that a uniform value between a higher and a lower roughness performs best. However, the overall average reveals that a more realistic condition with a spatially varying roughness is the best model set-up.

Table 5.3: Average RMAE from simulations with different bed roughness values.

variable	Chézy coefficient (C)							
	50	55	60	65	70	75	80	spatial
water level	0.361	0.337	0.318	0.304	0.292	0.283	0.275	0.318
u-velocity	0.276	0.264	0.258	0.258	0.257	0.268	0.284	0.262
v-velocity	0.315	0.331	0.355	0.402	0.473	0.548	0.623	0.342
overall average	0.317	0.311	0.310	0.321	0.341	0.366	0.394	0.307

The comparison for the simulated periods is presented next. Figure 5.7 shows measured and simulated water level yield from the calibrated set-up (spatial Chézy coefficient), which gave an average RMAE of 0.32. This set-up will be used further as the calibrated model set-up for the hydrodynamic simulations.

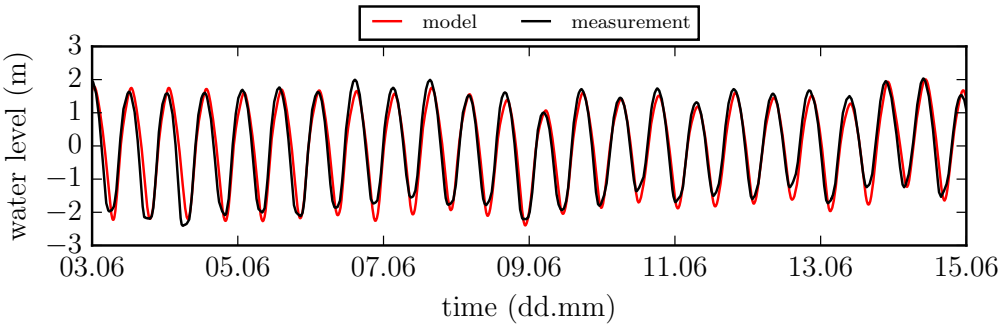

(a) Büsum station on June 2000

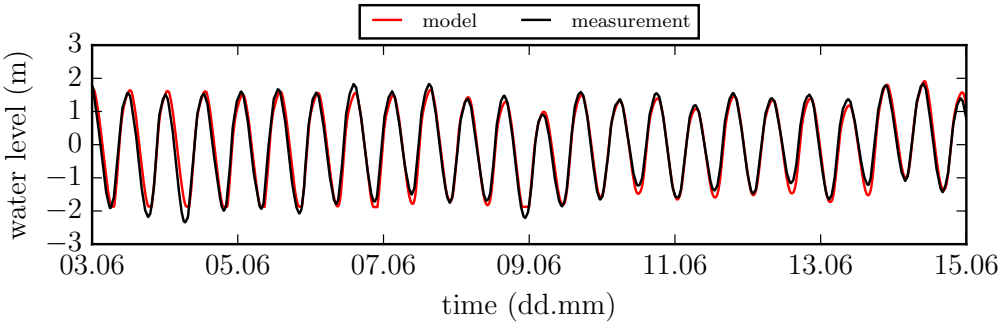

(b) Trischen station on June 2000

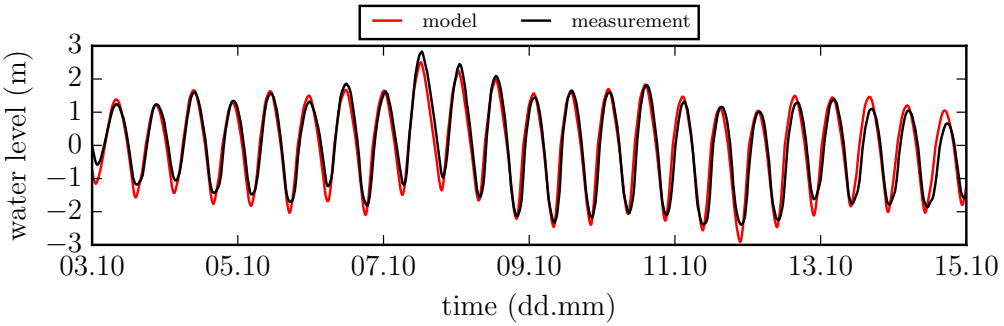

(c) Flackstrom station on October 2006

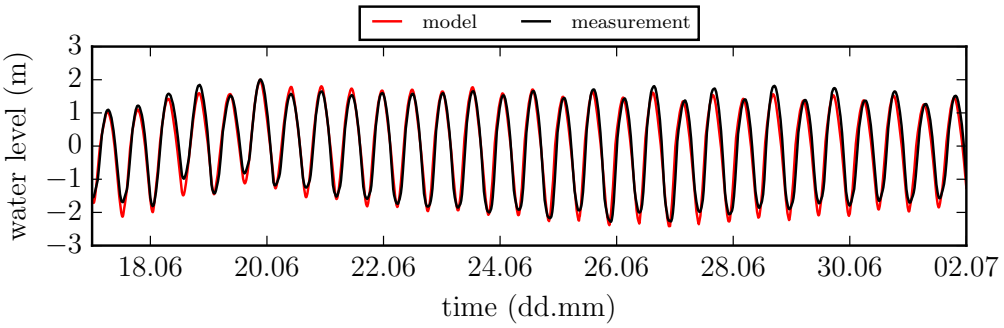

(d) Flackstrom station on June 2009

Figure 5.7: Water level at monitoring stations.

Figures 5.8 to 5.10 show the results of depth-averaged u- and v-current velocity for the periods when ADCP measurements were available in the northern part of the model, at the Piep channel system. Each figure presents a velocity component from model (mo) and measurements (me) at one cross-section in time (for locations see Figure 3.6). Statistical analysis showed that nearby the Piep channel system the RMAE for u-velocity is 0.35 and for v-velocity is 0.41, on average. According to Table 4.2, the model is qualified as *reasonable/fair* at this location.

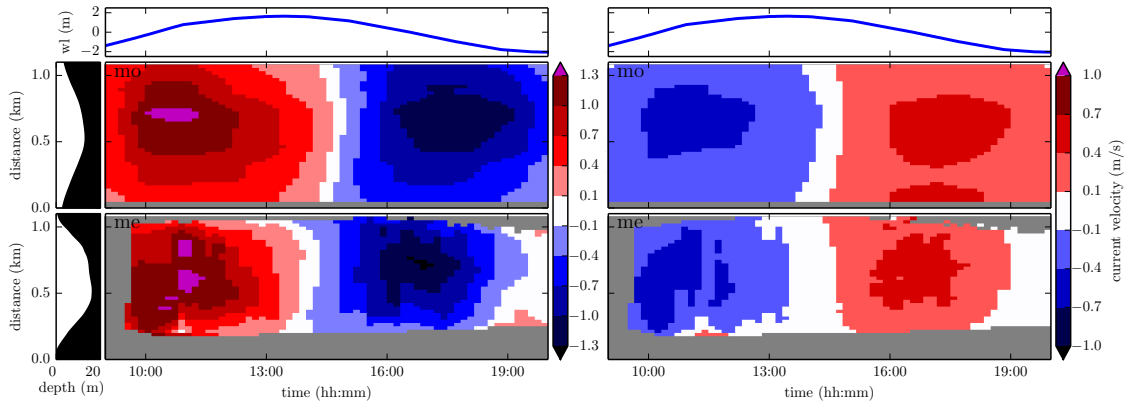

(a) u-velocity (b) v-velocity

Figure 5.8: Current velocity at cross-section Norderpiep on 05.06.2000: model (top) and measurements (bottom).

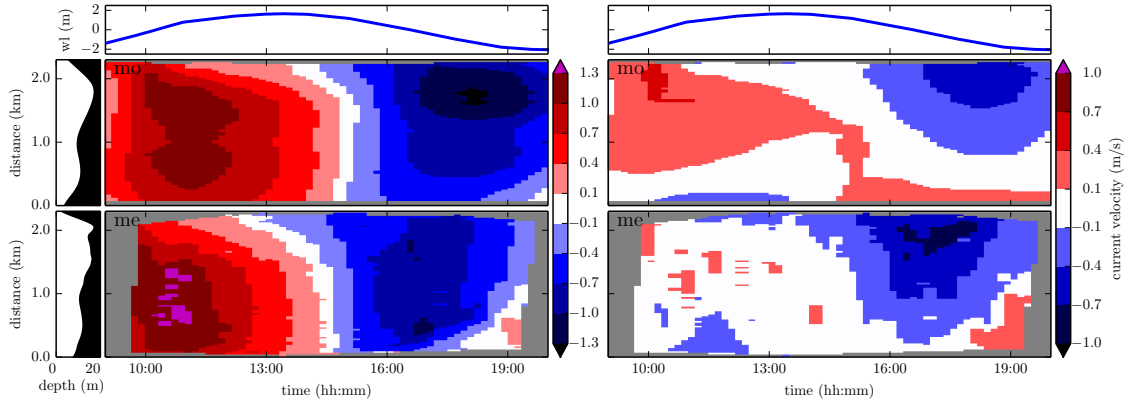

(a) u-velocity (b) v-velocity

Figure 5.9: Current velocity at cross-section Süderpiep on 05.06.2000: model (top) and measurements (bottom).

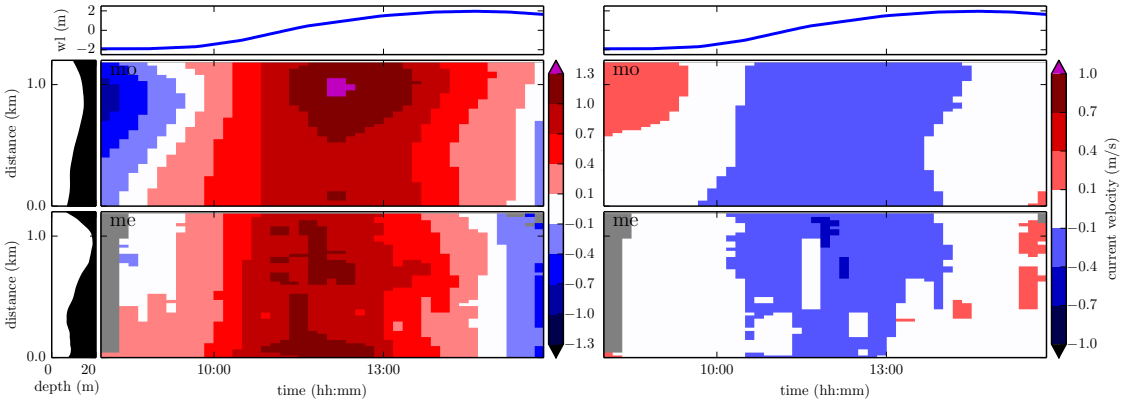

(a) u-velocity (b) v-velocity

Figure 5.10: Current velocity at cross-section Piep on 06.06.2000: model (top) and measurements (bottom).

Figures 5.11 to 5.13 show the results of depth-averaged u and v current velocity modelled (mo) and measured (me) at the cross-sections close to the MDPI (see Figure 3.6). Statistical analysis showed that in the MDPI vicinity the RMAE for u-velocity is 0.27 and for v-velocity is 0.20, on average. Hence, the model is qualified as *good* at this location. The superior performance of the model near the MDPI is already expected, as model grid and bathymetric measurements have a much higher spatial resolution than in the Piep channel system.

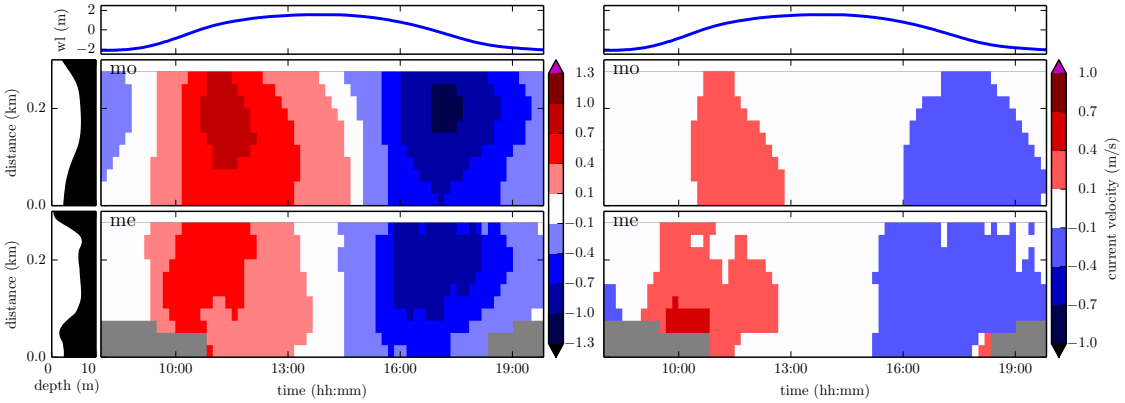

(a) u-velocity (b) v-velocity

Figure 5.11: Current velocity at cross-section C_1 on 20.02.2007: model (top) and measurements (bottom).

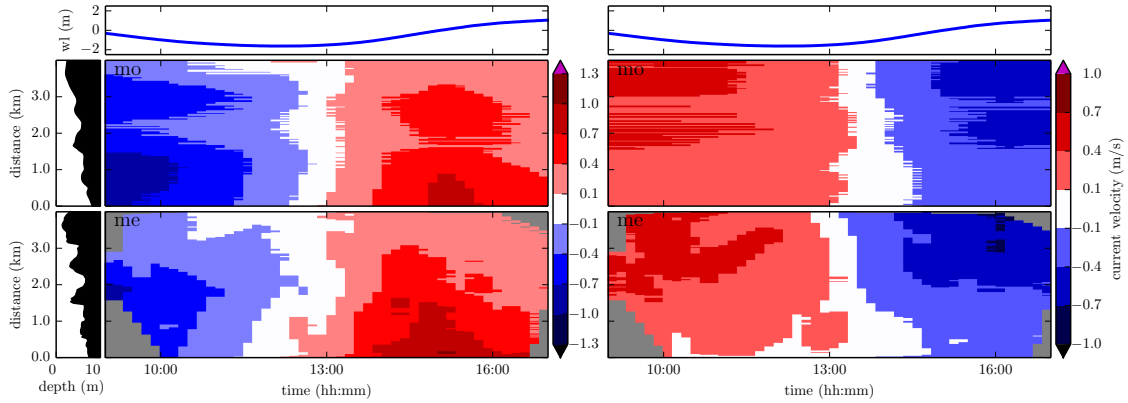

(a) u-velocity (b) v-velocity

Figure 5.12: Current velocity at cross-section C_4 on 17.06.2009: model (top) and measurements (bottom).

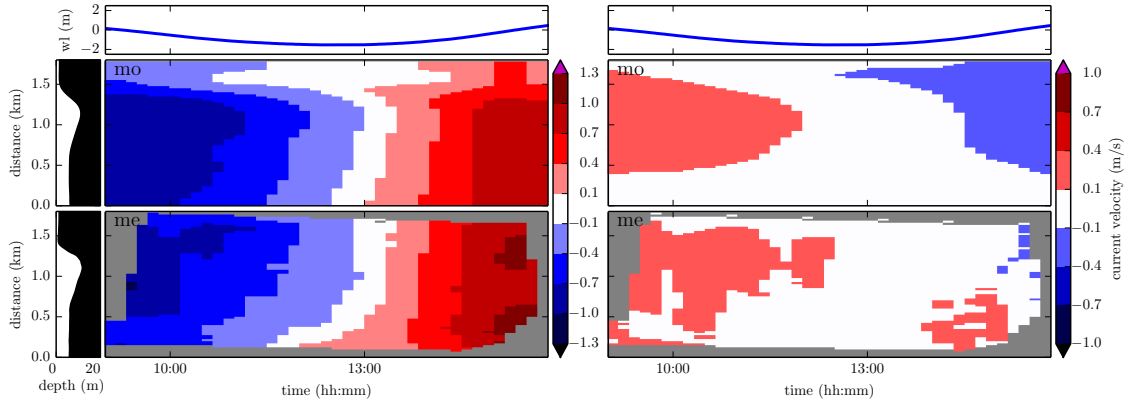

(a) u-velocity (b) v-velocity

Figure 5.13: Current velocity at cross-section C_3 on 01.07.2009: model (top) and measurements (bottom).

5.5 Sediment transport model

Once the hydrodynamic model is calibrated, the calibration of the sediment transport model may be initiated. This is usually done by exhaustively testing ranges of possible values for each model parameter and fine-tuning the most sensitive ones, a method well known as sensitivity analysis. In the Dithmarschen Bight some sensitivity analysis studies of sediment transport modelling are available (Poerbandono, 2003; Escobar Sierra, 2007; Etri, 2007; Nguyen, 2015). Thus, efforts in the present work will only focus on the most import parameters identified. Poerbandono (2003) presented values for the median grain size of the seabed in tidal channels varying from 80 to 230 µm, and showed that mud content from samples is usually greater than 5%. Escobar Sierra (2007) calibrated a sediment transport model for the Piep channel system. He applied four different grain sizes

of non-cohesive fractions (100, 110, 135 and 180 µm) and one additional cohesive fraction. Through model calibration he found values for the critical bed shear stress between 0.65 and 0.9 $\mathrm{N\,m^{-2}}$, and values for the settling velocity between 1.3 and 1.8 $\mathrm{mm\,s^{-1}}$, with regard to the cohesive fraction. Nguyen (2015) carried out an extensive sensitivity study with the MDPIM. She calibrated a sediment transport model with one sand fraction of 200 µm, and one mud fraction with critical bed shear stress of 0.3 $\mathrm{N\,m^{-2}}$ and settling velocity of 0.75 $\mathrm{mm\,s^{-1}}$.

The sediment transport model set-up applied in the present study considers three sediment fractions: two cohesive and one non-cohesive. The second cohesive fraction should simulate the consolidated layer found in the TF channel between 6 m and 8 m NHN, presented in Section 3.4.2. The non-cohesive and the cohesive fractions are based on the results from Nguyen (2015) and further sensitivity tests done by the author. In Table 5.4 the main properties of each fraction are presented. This model set-up has been defined as the *benchmark model*.

Table 5.4: Sediment properties considered in the benchmark model.

property	symbol	unit	cohesive	cohesive (consolidated)	non-cohesive
specific density	ρ_s	$\mathrm{kg\,m^{-3}}$	2650	2650	2650
dry bed density	$\rho_{s,d}$	$\mathrm{kg\,m^{-3}}$	500	500	1600
median grain size	d_{50}	µm	<63	<63	200
critical bed shear stress	τ_{cr}	$\mathrm{N\,m^{-2}}$	0.3	10.0	-
settling velocity	w_s	$\mathrm{mm\,s^{-1}}$	0.75	1.0	-

Before any further explanation, a technical aspect of the Delft3D sediment transport model must be clarified. The sediment fractions and their respective characteristics are defined in one specific file. For some of these characteristics it is possible to define either a uniform value over the domain or a file name in which the parameter is defined in each grid cell, i.e. non-uniform in space.

However, this feature does not work in some situations, e.g. the median grain size can only be non-uniformly specified over the domain if the simulation includes only one sediment fraction. In order to overcome such limitation, the sediment layer thickness is given non-uniformly over the domain. The thickness of each fraction was calculated as the following: (1) an initial mud content of 20% was assumed for the average d_{50}; (2) the remaining sand content was calculated to give the average d_{50}; (3) the ratios were converted to thickness based on the local depth. Finally, the combination of both fractions should represent the median grain size in each grid cell (see Figure 5.6a).

The consolidated sediment layer has been defined in the model in a way that erodible sediment will be only available up to a depth of 7 m NHN. Below that a second type of sediment characterized by consolidated deposit has been defined

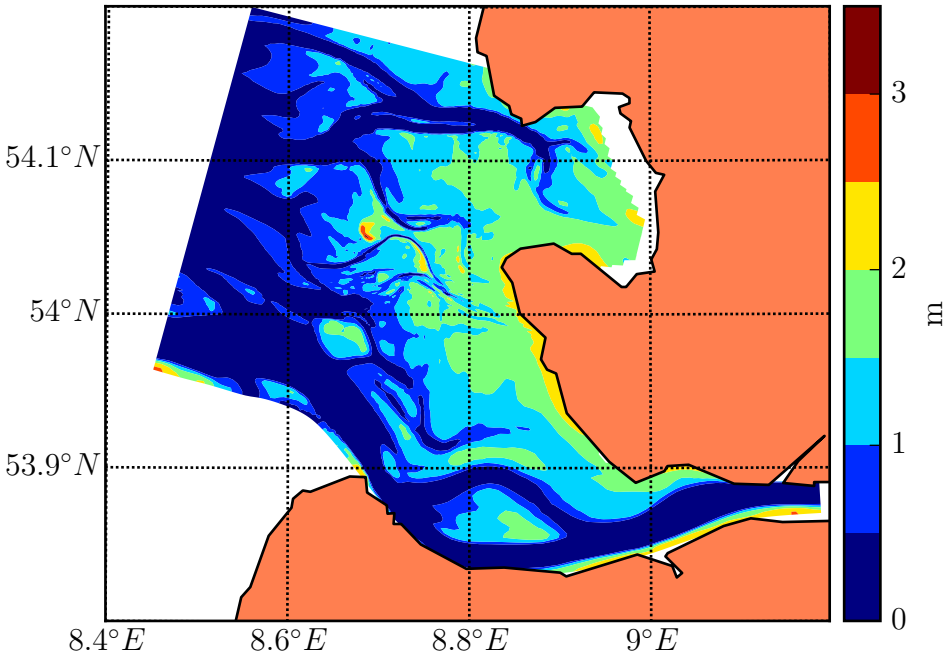

(a) cohesive fraction

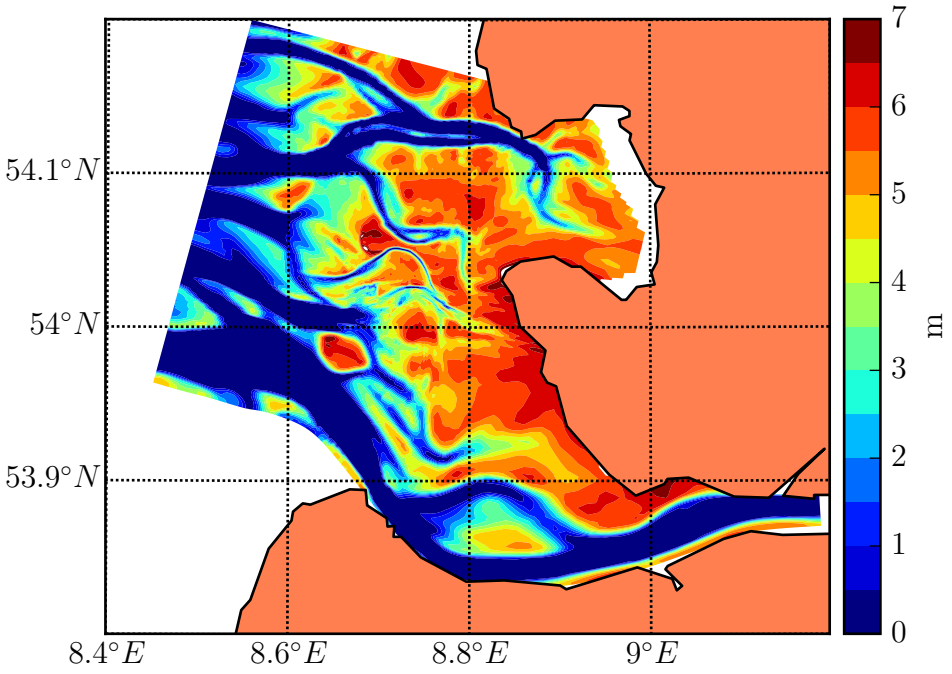

(b) non-cohesive fraction

Figure 5.14: Initial sediment layer thickness over the model domain.

to mimic a consolidated layer by assuming a high critical bed shear stress (τ_{cr} = 10 N m^{-2}). The consolidated layer thickness is assumed as equal to 10 m for the entire model domain. This implies that, where this consolidated layer is reached, very little erosion should take place. The result for the sediment thickness is then presented in Figure 5.14, in which the 0 m-thickness areas show the location

where the consolidated layer has been reached.

The sediment transport parameters have been tested within ranges considered to represent each parameter uncertainty. These variations are based on values found in the literature and on available measurements.

The median grain size uncertainty was based on statistics from samples measured in the MDPI area and on the work of van Vuren (2005). In a simplified case study of the Waal River (Netherlands), she assumed a uniform grain size described by a log-normal probability distribution with a standard deviation equals to half of the mean value. Measurements of median grain size in the current study area presented a deviation of 25% in the tidal channels and of 12% on the tidal flats, with respect to the mean value.

The critical shear stress uncertainty was based on the works of Barnes and Baldock (2007) and Darby and Sear (2008). The first authors measured bed shear stress directly by means of a shear plate and observed deviations up to ca. 25%. Analysis results for the critical bed shear stress indicated deviations of 18% from the mean value with a 90% confidence interval.

The settling velocity uncertainty was based on the works of Winterwerp et al. (2006) and Soulsby et al. (2013). Winterwerp et al. (2006) proposed an heuristic formula for describing settling velocity of cohesive sediment, while Soulsby et al. (2013) presented new formulations for the settling velocity of estuarine sediments with improved performance. In both studies, formulations for describing settling velocitiy in estuaries and coastal areas were tested, and their results showed that deviations may range from 0.40 to 0.69 $\mathrm{mm\,s^{-1}}$.

The sensitivity of each model parameter was initially tested within the ranges given in the literature. However, the concentrations produced in the model turned out to be much more sensitive than expected. Thus, adjustments to the ranges of the parameters were necessary to better fit measured sediment concentrations. Finally, the sediment transport model was tested within the ranges given in Table 5.5 by varying each parameter independently.

Table 5.5: Uncertainty of sediment transport parameters represented by statistical moments.

type	parameter	unit	ens. mean ($\overline{\mathbf{x}}$)	ens. std. dev. ($\mathbf{s}$)
non-cohesive	median grain size (d_{50})	µm	200	30
cohesive	critical shear stress (τ_{cr})	$\mathrm{N\,m^{-2}}$	0.3	0.03
	settling velocity (w_s)	$\mathrm{mm\,s^{-1}}$	0.75	0.3

The deviations considered for each model parameter will be the base for applying the ensemble method to the morphodynamic model, as presented in Section

4.3.2. From the defined mean and standard deviation values, a function following a Gaussian distribution can be defined. Then, n elements can be randomly chosen from this distribution to create a sample with the same original statistical moments, if n is sufficiently large.

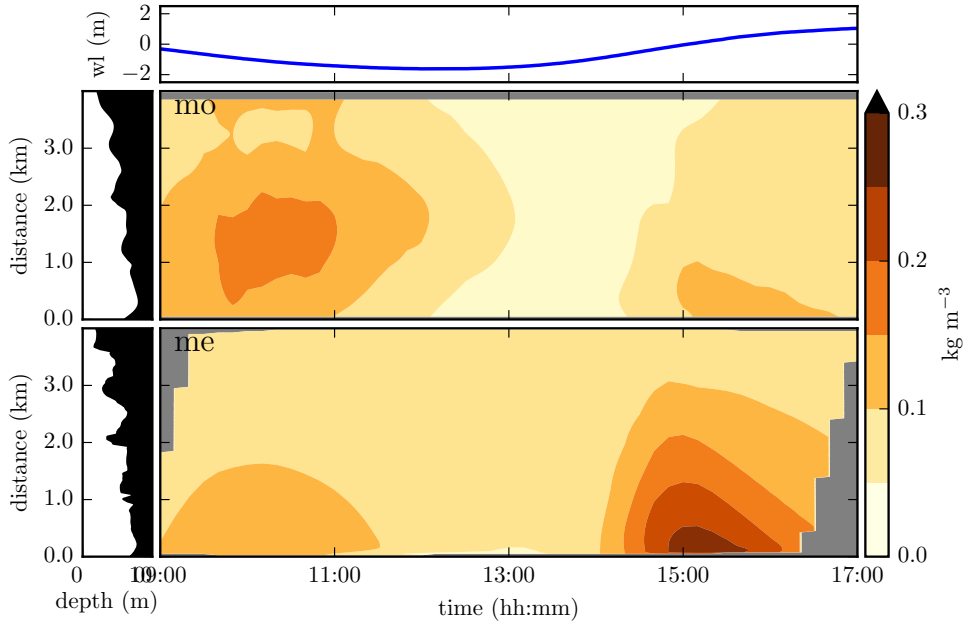

Figure 5.15: SSC along cross-section C_4 on 17-06-2009: model (top) and measurements (bottom).

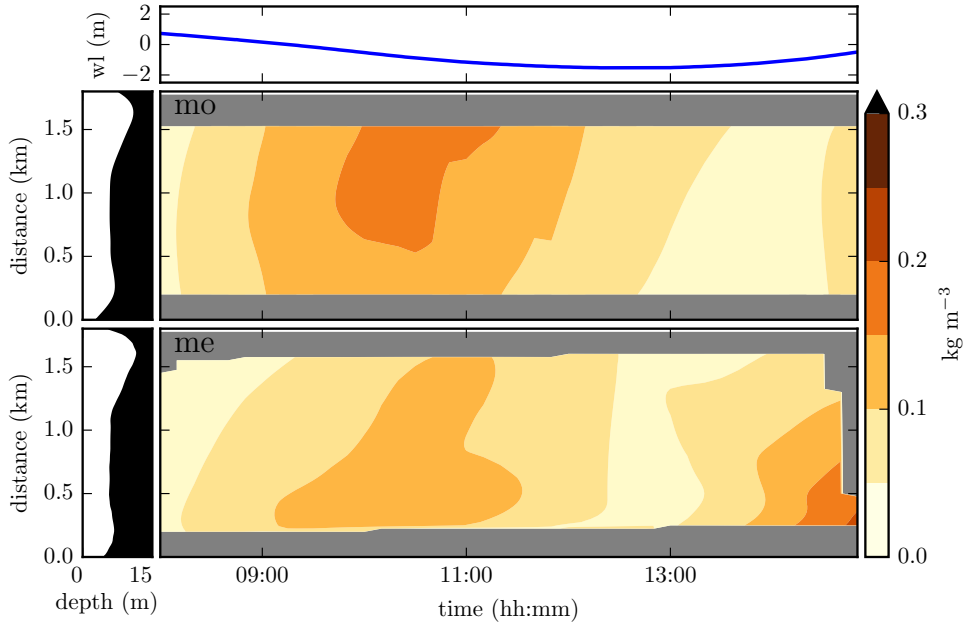

Figure 5.16: SSC along cross-section C_3 on 01-07-2009: model (top) and measurements (bottom).

First, results from the sediment transport model with the mean values ($\overline{\mathbf{x}}$)

have been analysed along cross-sections over time and compared to measurements (Figures 5.15 and 5.16). In cross-section C_4 measurements show that suspended sediment concentrations do not drop below $0.05\,\mathrm{kg\,m^{-3}}$ and in the deeper section they can reach up to $0.3\,\mathrm{kg\,m^{-3}}$ during flood tide. The model produces slightly larger SSC during ebb tide, but the simulated concentrations are in the same range as measurements. In cross-section C_3 measured values are more uniform along the section and simulated values are able to better reproduce the observed pattern during ebb tide.

Each one of the parameters has been varied by a range of $\overline{\mathbf{x}} \pm \mathbf{s}$, as given in Table 5.5. The results can be seen in Figure 5.17 and 5.18 presented as suspended sediment concentrations (SSC) in monitoring points along the respective measured cross-section (rows) for each sediment parameter (columns). The parameter uncertainty is represented by the light red shaded area, i.e. the range calculated from model results forced with the defined parameter value ($\overline{\mathbf{x}}$) plus or minus the assumed uncertainty ($\mathbf{s}$); the red line represents the benchmark model, and the dotted line the measurement.

At cross-sections C_3 and C_4 the model reproduces similar order of magnitude of SSC ranging between 0 and $0.2\,\mathrm{kg\,m^{-3}}$. At the northern part of cross-section C_4 the simulated values still oscillate during ebb and flood tide, while measurements show a rather constant concentration. Meanwhile at the southern part the ebb and flood effects are more significant and more correctly captured in the model. The sediment transport model at this location presents an average RMAE of about 0.4 for SSC at the nine measured stations.

At cross-section C_3 results are more consistent. The length of the cross-section is smaller and its position lies on a tidal channel, which is located east from the southern part of cross-section C_4 (see Figure 3.6), resulting in higher current velocities. The measured SSC at this cross-section shows a clear response during ebb tide, which can be reasonably well reproduced in the model. With respect to errors, calculations show that the average RMAE is also in the range of 0.4 for SSC, similar to the previous one.

The variations in SSC resulting from the uncertainty ranges applied to the sediment transport model are given relative to benchmark results (see Table 5.6). In both cross-sections C_3 and C_4, the uncertainty considered in settling velocity produced the largest relative variations in suspended concentrations (92% and 99%) from the three sediment transport parameters taken into account. The uncertainty in critical shear stress produced ca. 30% variations, whereas the median grain size did not produce significant variations in SSC. This indicates that the settling velocity is the most sensitive parameter to the model, based on suspended concentrations. On the other hand, the influence of the median grain size in SSC

can be neglected.

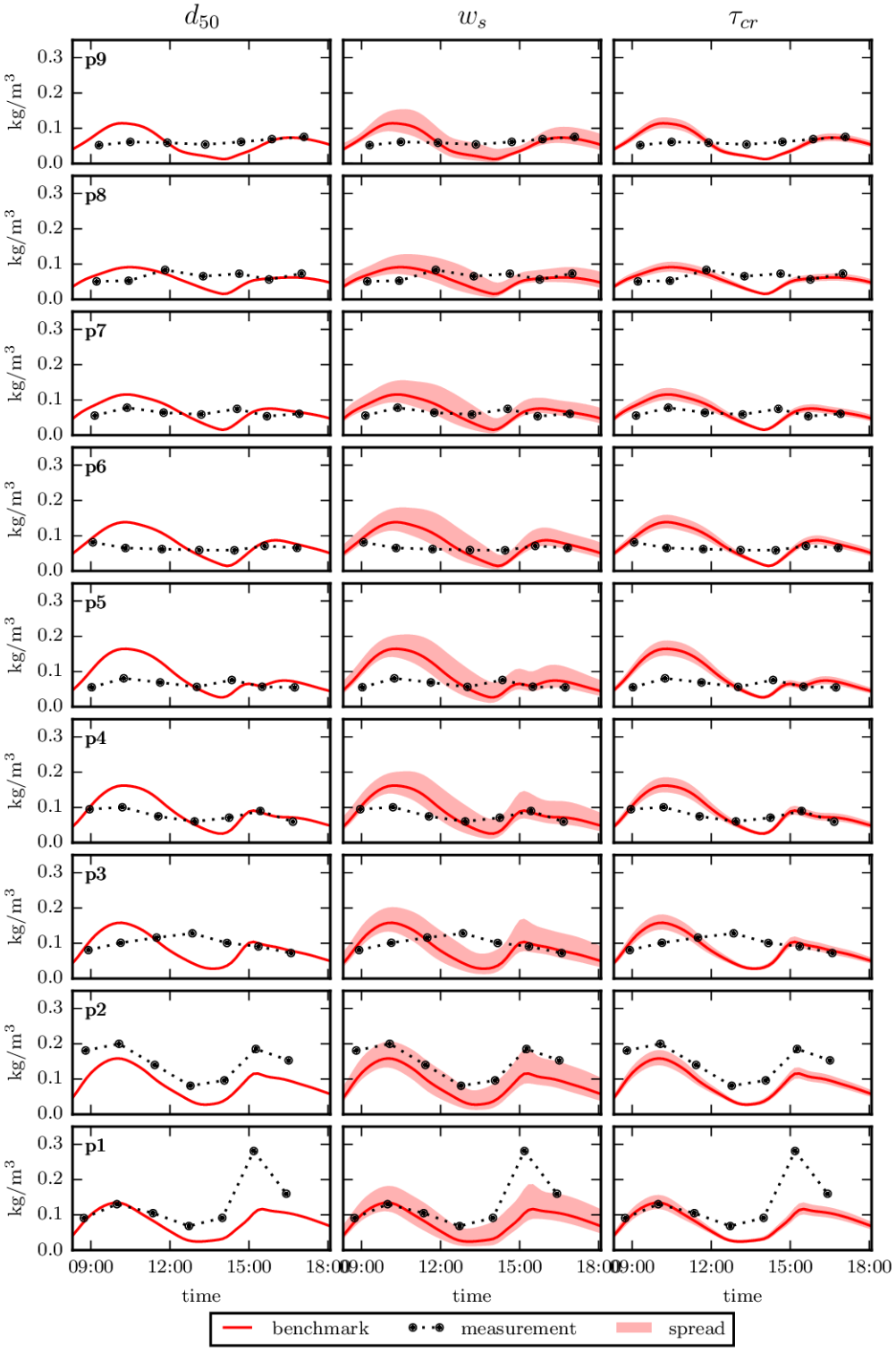

Figure 5.17: SSC uncertainty at cross-section C_4 on 17.06.2009: median grain size (left), settling velocity (centre) and critical shear stress (right).

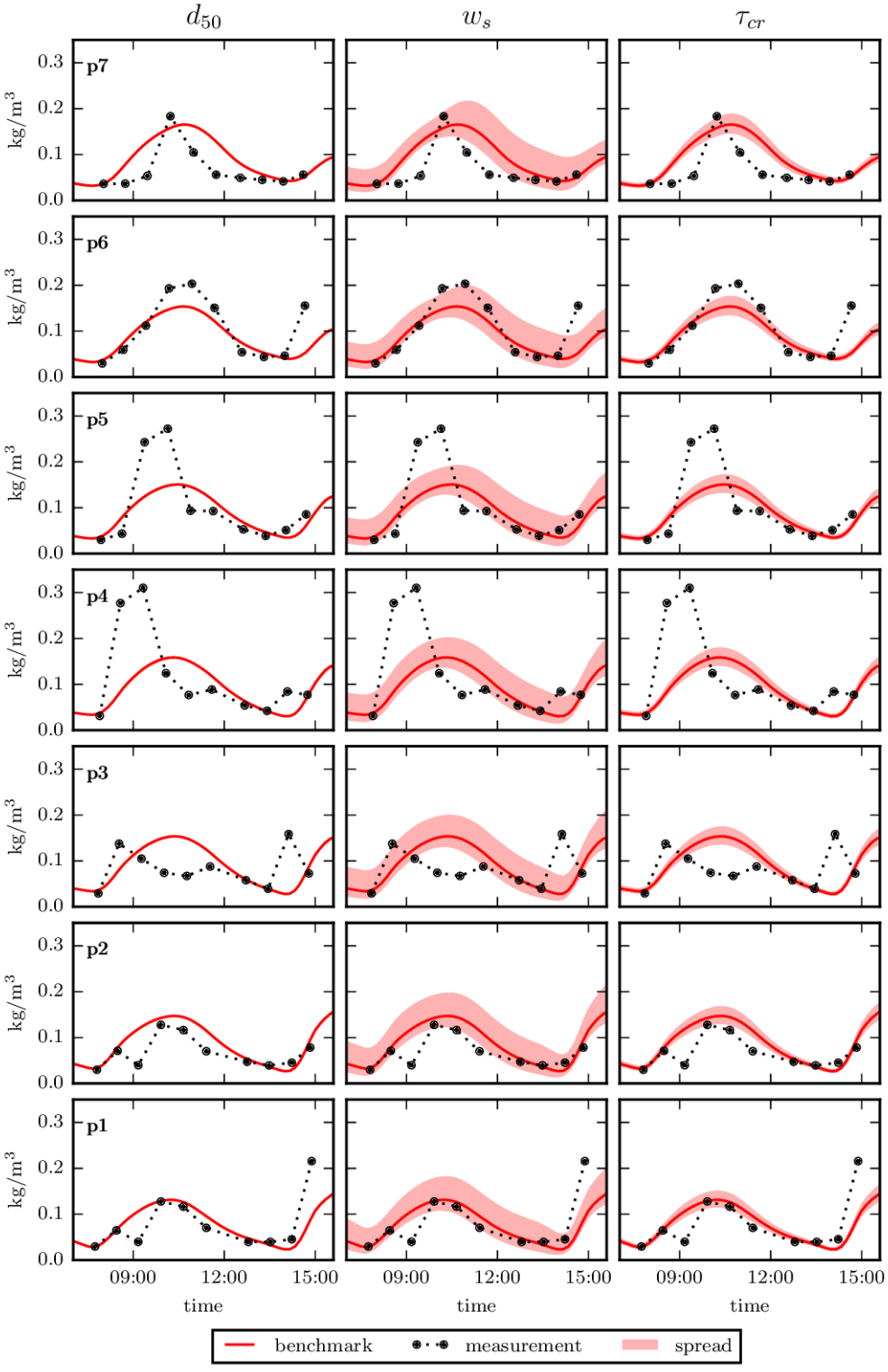

Figure 5.18: SSC uncertainty at cross-section C_3 on 01.07.2009: median grain size (left), settling velocity (centre) and critical shear stress (right).

Table 5.6: Effect of parameter uncertainty on modelled sediment transport relative to benchmark.

type	parameter	cross-section C_3		cross-section C_4	
		SSC	bedload	SSC	bedload
non-cohesive	median grain size (d_{50})	1%	21%	1%	21%
cohesive	critical shear stress (τ_{cr})	30%	-	31%	-
	settling velocity (w_s)	92%	-	99%	-

Sediment transport models like the one applied make use of empirical equations calibrated in laboratory flumes, such as the van Rijn's formula for bedload (see Section 4.1.4), which represent the best results based on the available information and technique. Model results have shown that the SSC uncertainty is more influenced by the settling velocity and critical shear stress than by the median grain size. Because in Delft3D the median grain size parameter is only defined for the non-cohesive fractions, this parameter will produce a reduced effect on the SSC.

Chapter 6

Morphodynamic ensemble simulations

The set-up of a morphodynamic model requires several steps before an actual morphodynamic simulation may take place. As presented so far, the hydrodynamic and the sediment transport models have been calibrated. In this chapter the results of the morphodynamic ensemble simulations together with their analysis will be presented.

The ensemble is composed by a number of model set-ups that slightly differ in the sediment transport model settings based on the uncertainty ranges defined in the last chapter. The deviation in the model set-up is considered to produce significant variations in the morphodynamic model results, according to the ensemble method (see Section 4.3.2).

In the present work an ensemble with 30 members has been applied. This ensemble size is much smaller than usual meteorological ensemble forecasts (commonly larger than 50) or traditional Monte Carlo Simulation applications, but it is considered to be statistically large enough. From sensitivity analysis with sample sizes up to 50 members, it was concluded that results do not change significantly when the sample size is larger than 30. The ensemble members have been defined based on the parameter ranges considered for the sediment transport model. Through the use of a mathematical function to generate normal random values, the 30 members have been created and are presented in Appendix A.

In the following sections results of two ensemble simulations will be presented. Both simulations are about two-year long, so that the initial and final simulated bathymetries match available measured data in time.

6.1 Ensemble 2006 - 2008

6.1.1 Initial conditions

August 2006 is considered to be the first time point, in which high-resolution bathymetric measurements covering the whole tidal flat and its surroundings in the vicinity of the MDPI are available (see Figure 3.8). The next point in time with similar spatial coverage is June 2007, and then the beginning of September 2008.

The model start bathymetry has been reconstructed based on the most up-to-date available measurements up to 01.09.2006 (see Figure 6.1). It means that, for each grid cell the most up to date measurement has been assigned (when available) and finally the whole data set has been interpolated in order to avoid gaps or discontinuities. The ensemble simulation goes from 01.09.2006 to 01.09.2008, so that the morphology is able to present enough development over time, and the start/final bathymetries can be compared to measurements.

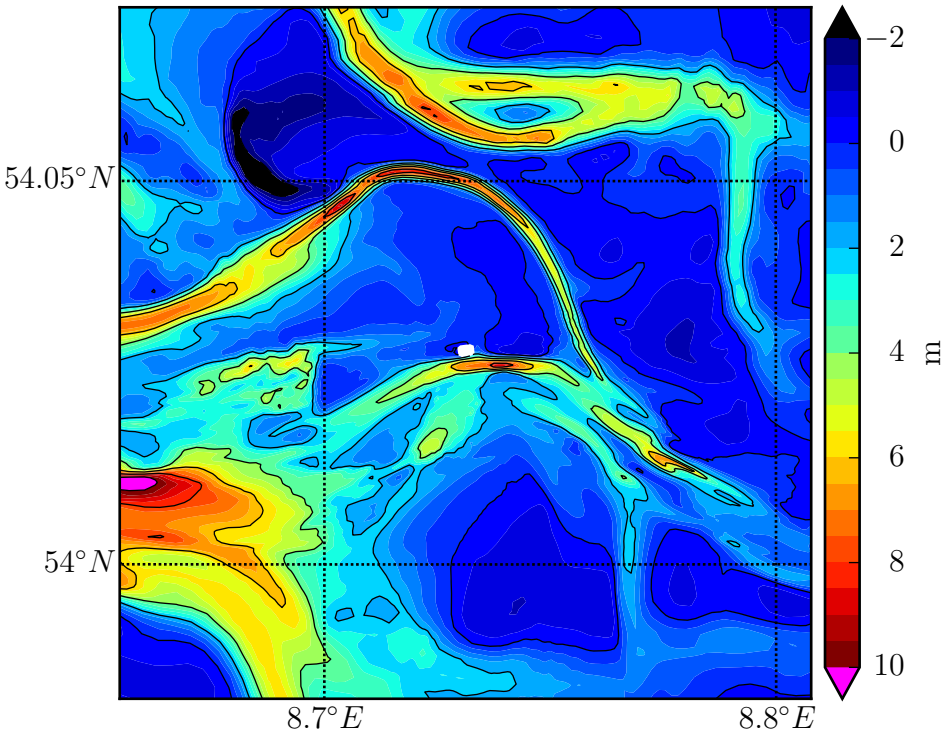

Figure 6.1: Model start bathymetry on 01.09.2006.

According to the modelling procedure described in Section 5.2, water level and wave spectrum information are prescribed at the MDPIM open boundaries. Together with meteorological forcing available from the DWD global model, these are the model driving forces adopted throughout the simulation period.

6.1.2 Meteorology

A short description of the meteorological conditions during the simulation period is given here based on the DWD global model data. The wind rose at the MDPI (Figure 6.2) shows that the predominant wind direction is from SW to NW (total frequency above 40%) with wind magnitudes half of the time between 30 and 50 km h^{-1}.

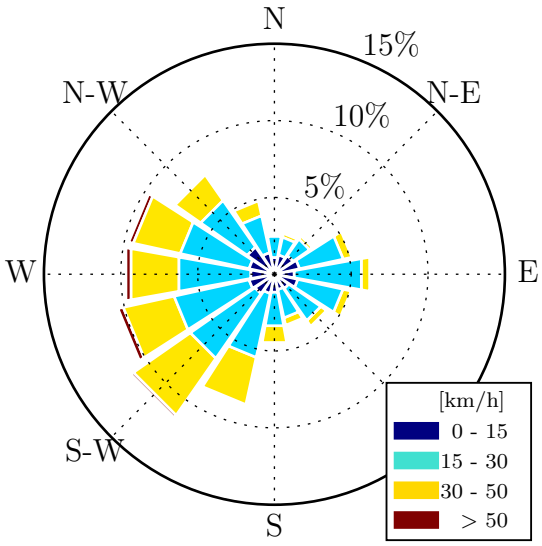

Figure 6.2: Wind rose from DWD meteorological model at the MDPI location from 09.2006 to 09.2008.

Despite the apparent mild conditions represented by the wind rose, the small percentage of wind speeds above 50 km h^{-1} includes large storms that may produce significant changes in morphodynamics along the coast. During the two-year period, several storms have been reported all over Northern Europe. The most important ones are listed in Table 6.1. From the eight severe winter storms identified between 2006 and 2008, five (Britta, Kyrill, Tilo Paula and Emma) directly affected Germany; storms Kyrill and Tilo produced the most severe flooding and damage.

Energy analysis

In order to estimate how much the meteorological forcing affects model results in the study area, the concept presented in Section 4.2 has been applied. The following results present the ratio from the largest 3-day energy integration calculated.

Results obtained from the energy ratio due to meteorological conditions in the simulated period (Figure 6.3) show the contribution from the air pressure and wind field in the study area during storm events. Exposed areas such as tidal

Table 6.1: Severe European winter storms between 2006 and 2008.

name	date	description
Renate	2-8.10.2006	A powerful storm battered the south west coast of France with gusts of 150 $\mathrm{km\,h^{-1}}$.
Britta	29.10-4.11.2006	A storm made its way through the North Sea with gusts reaching 174 $\mathrm{km\,h^{-1}}$ in Denmark and southern Sweden. It caused a surge record in Delfzijl, Netherlands, and a 100-year event in the Kattegat.
Franz	10-13.1.2007	A strong depression north of Scotland brought high winds to most of the United Kingdom with a central pressure of 951 hPa and gusts of 151 $\mathrm{km\,h^{-1}}$.
Hanno	9-16.1.2007	This powerful storm hit south-western Sweden with wind gusts up to 140 $\mathrm{km\,h^{-1}}$.
Kyrill	17-23.1.2007	Regarded as one of the most violent and destructive storms in more than a century. Storm-warnings were given for many countries in Europe. In Germany wind speeds of up to 195 $\mathrm{km\,h^{-1}}$ have been recorded.
Tilo	6-11.11.2007	Gusts as high as 140 $\mathrm{km\,h^{-1}}$ were reported, along with early snow for the Scottish highlands. The combination of strong NW winds, low pressure and high spring tides produced severe flooding in England. The highest surge in the North Sea for 20 years was recorded.
Paula	24-27.1.2008	This strong European windstorm hit Poland, Germany, Austria, Denmark, Norway and Sweden. Gusts reached 165 $\mathrm{km\,h^{-1}}$ in the Alps.
Emma	28.2-7.3.2008	This strong European windstorm hit Germany, Austria, Czech Republic and Poland. Gusts reached 190 $\mathrm{km\,h^{-1}}$ in the Alps.

Source: Thornton et al. (2016).

flats receive an energy input of at least 50% from meteorological sources during storms. During normal conditions, however, there is no significant additional energy contribution meaning that tides are the main driving force.

6.1.3 Results

The results from the ensemble simulation are presented in this section. Because the ensemble is generated from an assumed normal probability distribution, its results are analysed in a probabilistic point of view. Figure 6.4 shows the mean $\overline{\mathbf{x}}$ (top) and the standard deviation $\mathbf{s}$ (bottom) of the ensemble bathymetry at the end of the simulation. Values for $\mathbf{s}$ in terms of bed level variation can exceed

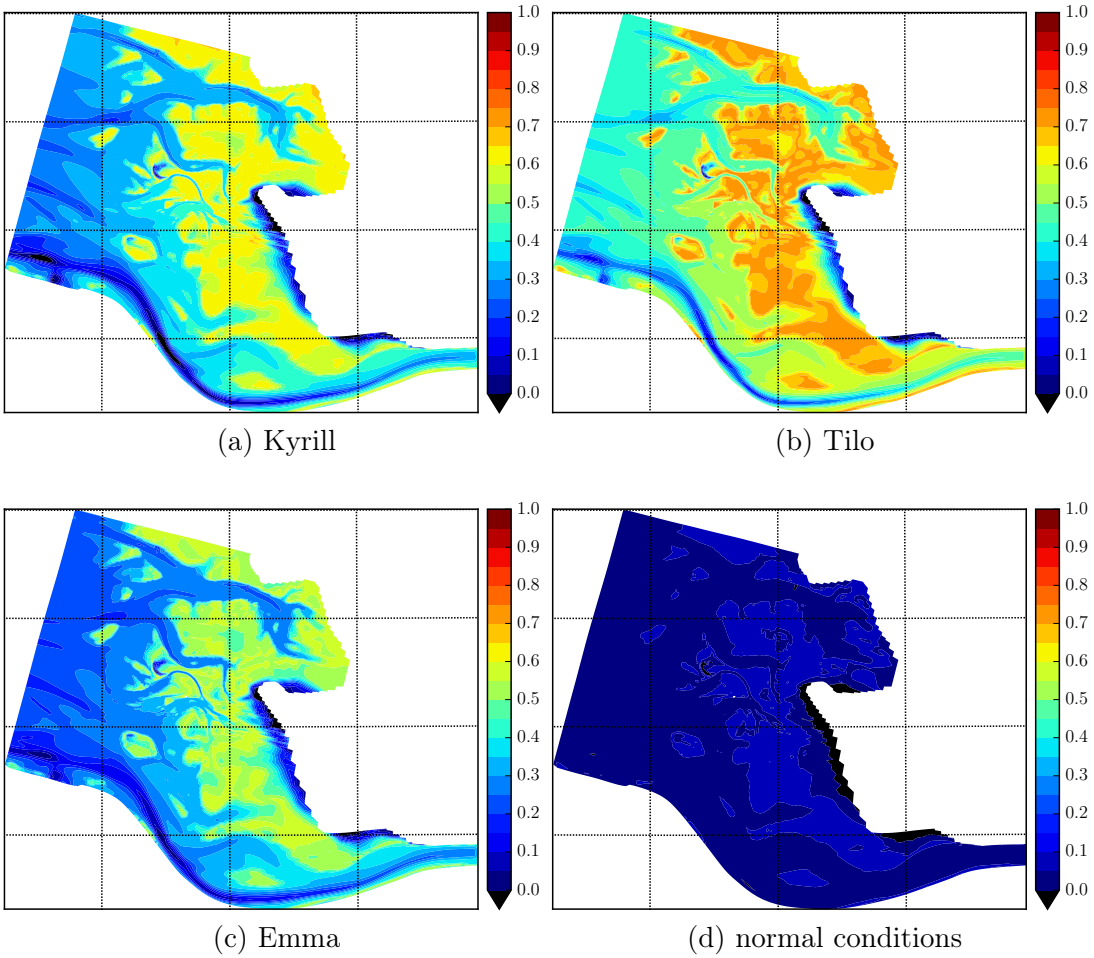

(a) Kyrill (b) Tilo

(c) Emma (d) normal conditions

Figure 6.3: Energy ratio due to the meteorological component from storm events (a, b, c) and normal conditions (d) between 2006 and 2008.

1.5 m at some locations. Generally locations deeper than 2 m (tidal channels) present larger variations.

The comparison of measured and (mean) modelled bathymetries for August 2006, June 2007 and September 2008 is presented in Figure 6.5. The final model bathymetry in 2008 presents a larger tidal flat area above the 0 m-isoline, north-east of the MDPI (figure centre), which is not observed in the measurements (see Figure 6.5c). The TF channel got uniformly deeper and its southern sediment bank (2 m-isoline) increased and merged. These characteristics are not observed in the measurements. However, the model correctly represented the retreat of the NF channel connection to the TF channel, and the beginning of the formation of a tidal channel southern from the TF channel. Also, the advance of the TF channel towards north, next to the MDPI, is in agreement with measurements and will be later discussed in details.

The evaluation of model performance is done by calculating indexes of confidence and skill (Section 4.4). The Confidence Index (CI) indicates where the

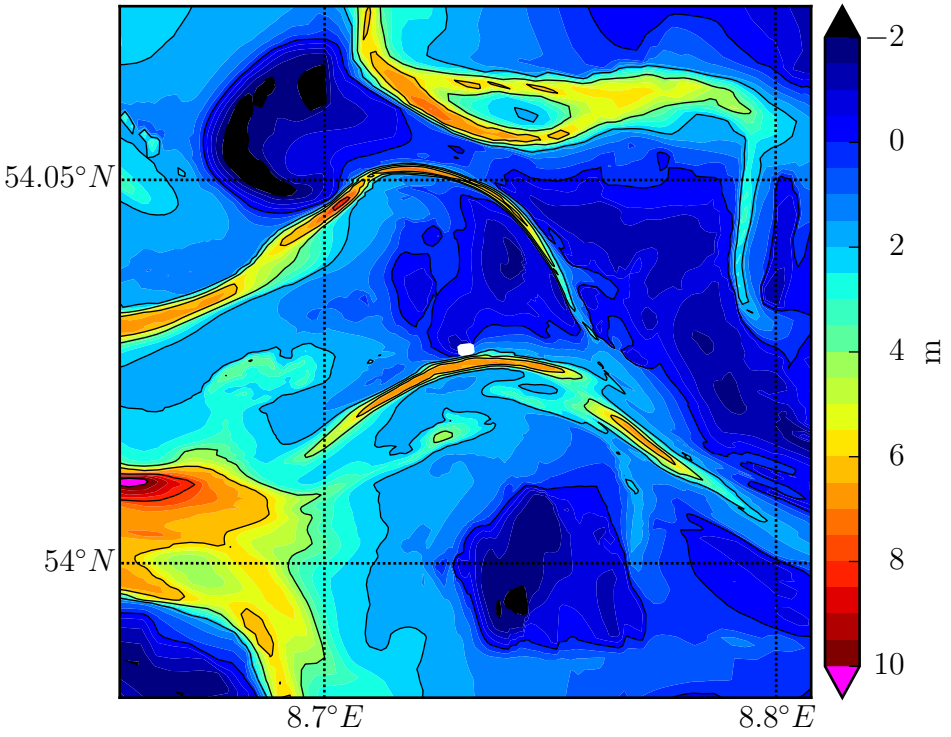

(a) mean

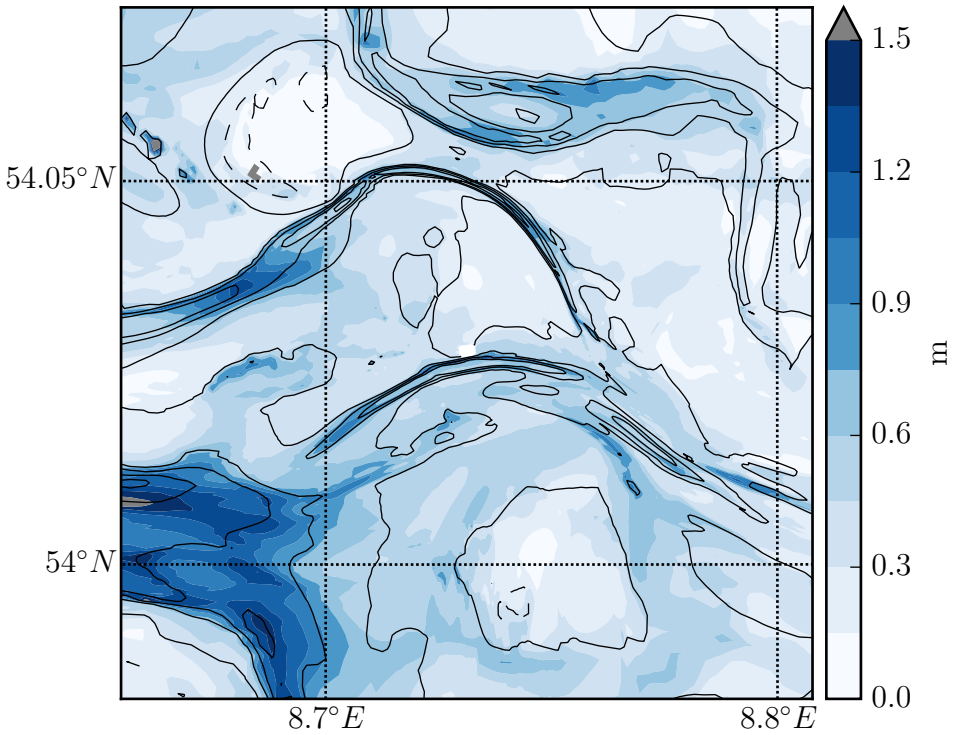

(b) standard deviation

Figure 6.4: Ensemble results for model bathymetry at the end of the simulation (01.09.2008).

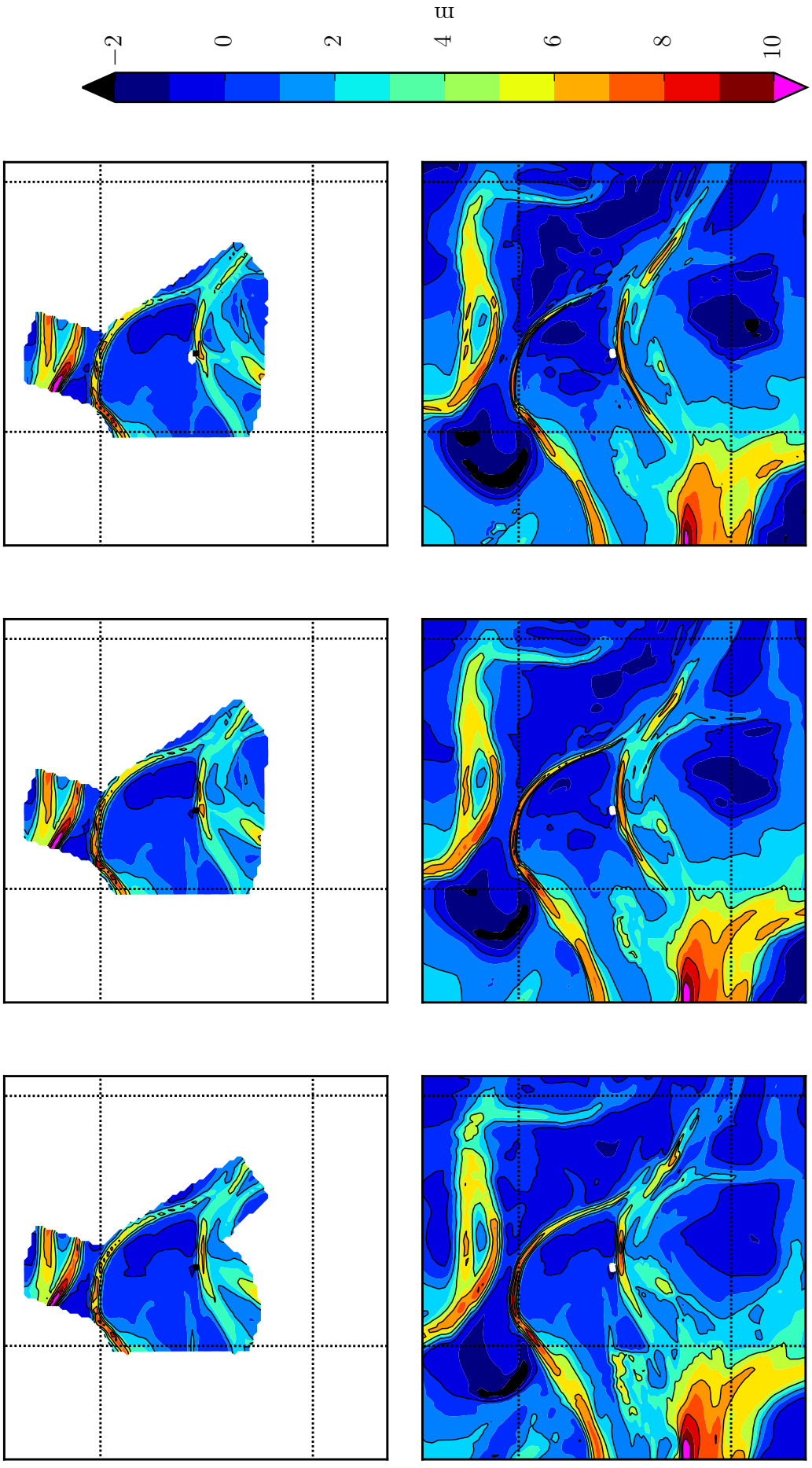

(a) August 2006 (b) June 2007 (c) September 2008

Figure 6.5: Bathymetric evolution during the morphodynamic ensemble period of 2006-2008. Measurements (top) and model (bottom).

ensemble presents a deviation of the bed level changes with respect to their mean. Values equal or smaller than zero indicate the deviation is larger than the mean of the absolute bed level changes. In this case (and these locations) model predictions are not relevant. On the other hand, values larger than zero indicate locations where ensemble results are in best agreement. In Figure 6.6a a positive CI is found mainly in tidal flat areas (above 0 m NHN) and in some parts of the tidal channel.

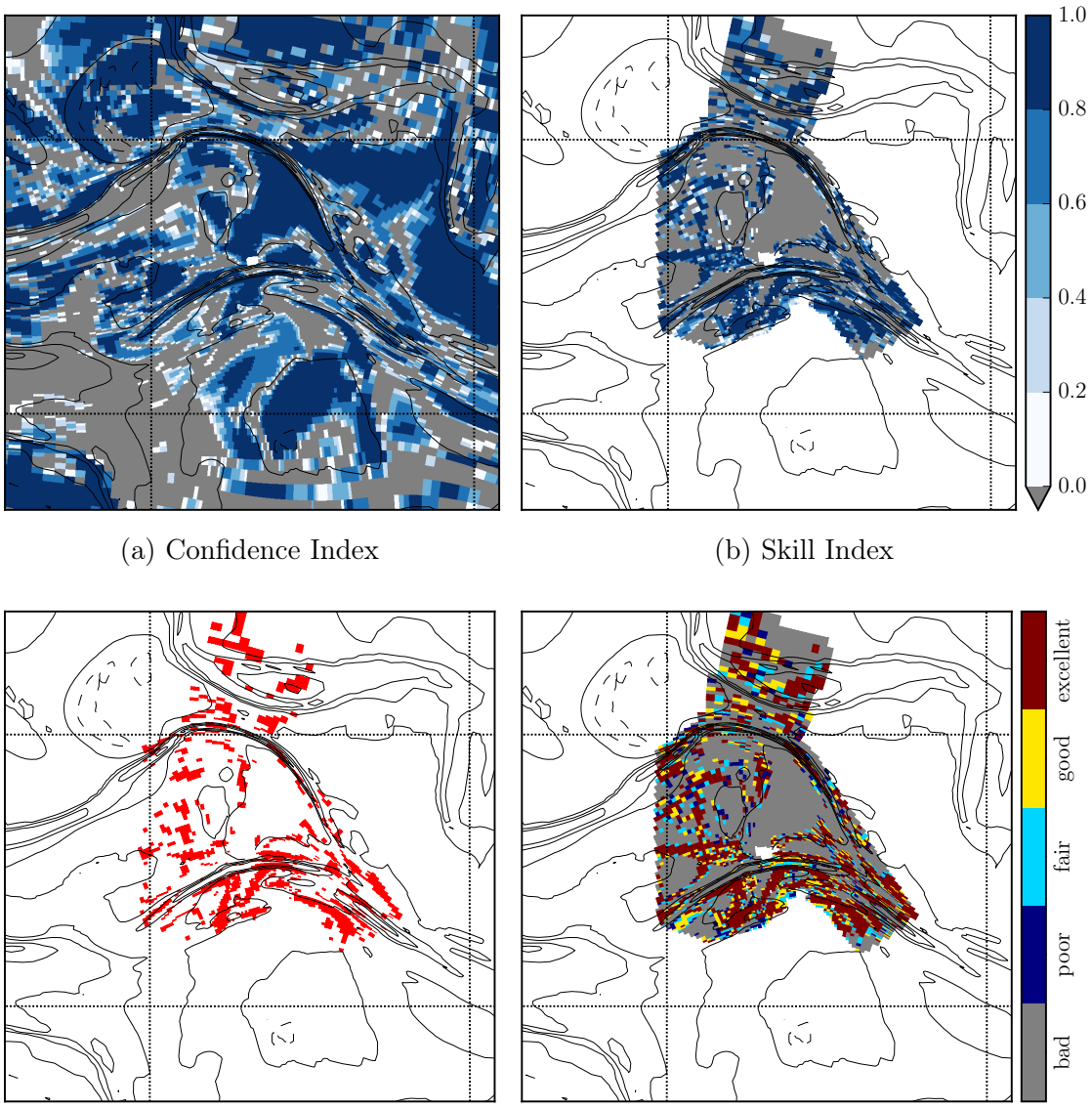

(a) Confidence Index

(b) Skill Index

(c) confidence and skill overlapping

(d) skill qualification

Figure 6.6: Performance of the morphodynamic ensemble simulation 2006-2008.

The Skill Index (SI) indicates the magnitude of bathymetric deviations between measurements and ensemble results. Values equal or smaller than zero indicate poor model skills, whereas values larger than zero represent good agreement with measurements. The TF channel section located eastward from the

MDPI presents positive index, as well as measured locations southwards from it (Figure 6.6b).

The combination of the confidence and the skill results in areas in which both indexes meet the condition for acceptance, here defined when CI > 0 and SI > 0.3 (Figure 6.6c). Only positive Confidence Index values have been taken into account, as previously explained. The Skill Index condition was chosen on the basis of the BSS classification from van Rijn et al. (2003), indicated in Table 4.2. The model skill qualification according to that table is presented in Figure 6.6d.

The analysis of the Confidence Index evolution in time results in Figure 6.7, in which the index is averaged in space. Until the end of 2007 the index average value remains approx. constant around 0.9. Then, it drops below 0.8 and later to ca. 0.7. This change indicates that the deviation of the modelled bed level changes increased relative to their mean. In other words, the members reach a final state that differs significantly from the mean.

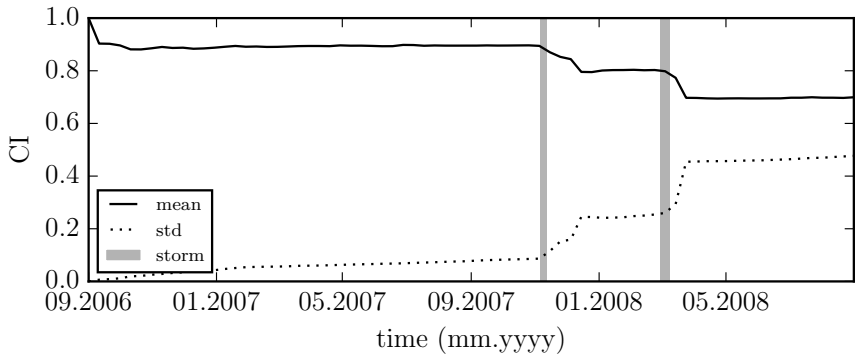

Figure 6.7: Time series of the space-averaged Confidence Index from 2006 to 2008.

The most probable cause for that is the meteorological forcing. During the time period in which a drop in the Confidence Index is observed, a winter storm that exceeds $20\,\mathrm{m\,s^{-1}}$ ($72\,\mathrm{km\,h^{-1}}$) at Helgoland was identified based on hourly measurements available from DWD (2016). Although it is not a very strong storm, especially in the North Sea, according to the Proudman Oceanographic Laboratory Annual Report (POL, 2008), on 9 November 2007 the east coast of the UK experienced the worst storm surge in 50 years. Among the storms listed in Table 6.1, this was clearly the most severe one in terms of surge during the simulated period. DWD measurements recorded that Cyclone Tilo produced significant wave heights up to 9 m (Nordseeboje, German Bight), and water levels up to 5.4 m NHN (Hamburg). The maximum wind gust registered was $146.5\,\mathrm{km\,h^{-1}}$ at Spiekeroog.

The spatial-averaged Skill Index (SI) for the available measurements in time is shown in Figure 6.8. Only positive SI values were taken into account. This

form of the index is similar to the BSS in the sense that it represents the model skill with only one score. Similarly to the analysis presented for the Confidence Index in time, it is also possible to address model skill evolution in time. It shows that the model skill decreases in time (partial result). The overall skill is larger than 0.6, meaning *good* skill according to the classification shown in Table 4.2. However the map shown in Figure 6.6b provides a much better indication of the model performance.

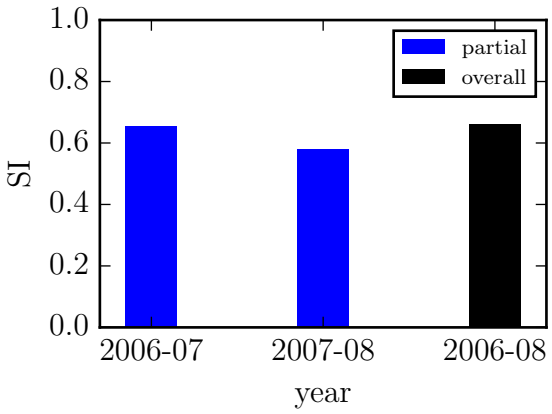

Figure 6.8: Space-averaged Skill Index between 2006 and 2008.

The analysis of results should preferably rely on specific regions in the model where the Skill Index is accepted. If one defines cross-sections located where $SI > 0$, for example as the ones presented in Figure 6.9, then these cross-sections can be evaluated as follows. The red solid lines represent the modelled mean bathymetry from the ensemble (solid) and from the benchmark (dashed), which represents the model set-up with the mean parameter values $\overline{\mathbf{x}}$. The light red shaded areas represent the 68% prediction interval (one standard deviation), assuming a Gaussian distribution for model results.

The Skill Index values (blue bars on the bottom) show locations in which the modelled bed level changes are in agreement with the measured ones. Dark blue colours indicate the skill from the ensemble mean and the light blue colours represent the skill considering the ensemble spread.

Between cross-sections C and H (the east part of the TF channel), model results are able to represent the channel migration towards the north. However, quantitatively the final migration was underestimated by the model. Measurements show a more pronounced migration in the eastern cross-sections than in the western part. This observation is also identified in the model, but in a smaller scale.

The measured and mean simulated migration distance of each cross-section related to the 4 m-isobath, as well as the ensemble standard deviation are presented

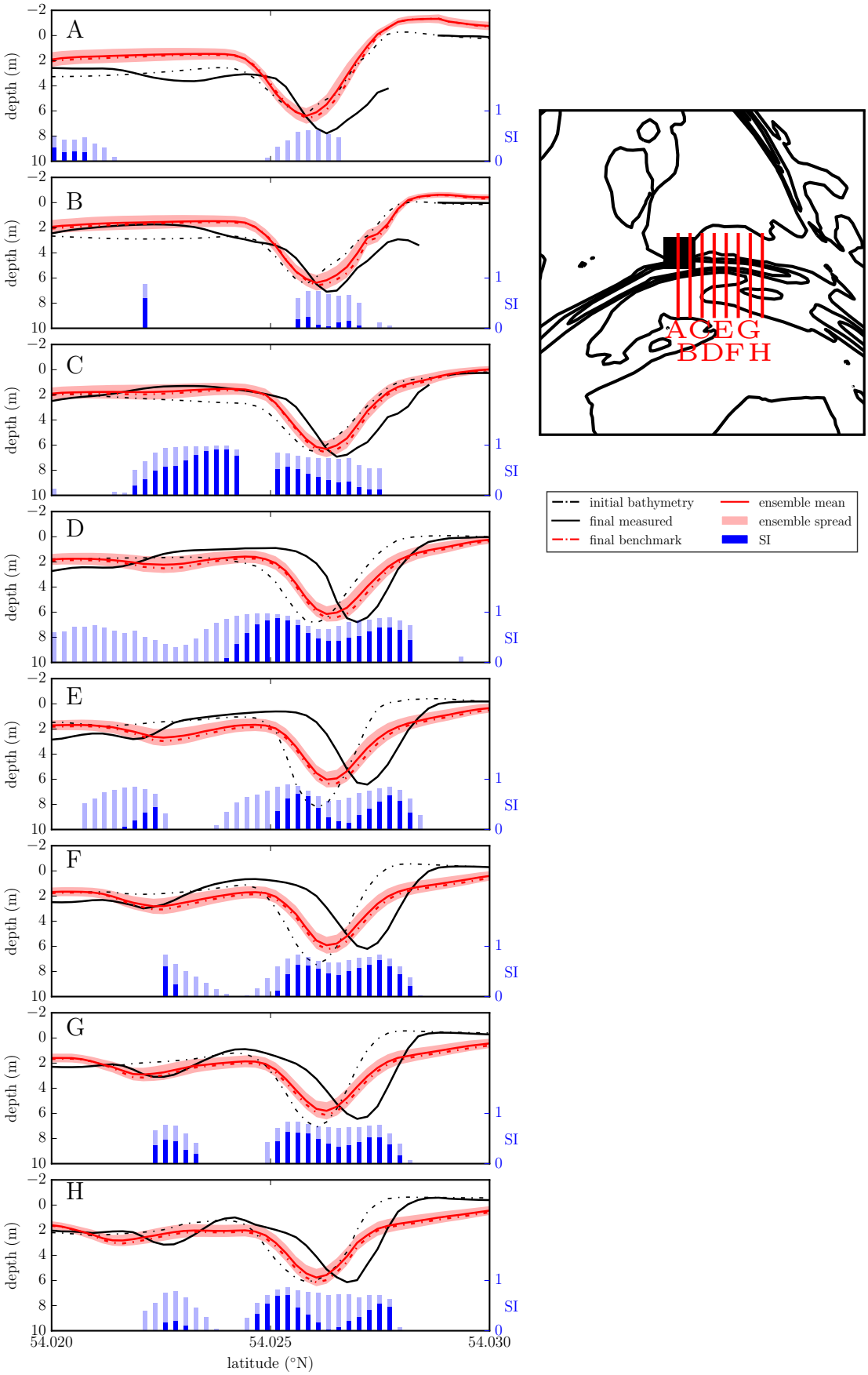

Figure 6.9: Bed level evolution between 09.2006 and 09.2008 at cross-sections A to H (right).

(Table 6.2). Although the model is able to reproduce the migration northwards, the migration is on average ca. three times smaller than observations. Based on the morphodynamic ensemble it is possible to determine the migration probability within one standard deviation, for example. The calculated standard deviation of the tidal channel migration is equal to 11 m. If added to the mean value it represents almost half of the observed migration (43 m), with a 68% confidence interval.

Table 6.2: Cross-section migration distance of the 4 m-isobath.

CS	unit	A	B	C	D	E	F	G	H	mean
observed	m	78	58	76	118	118	118	103	88	95
ens. mean ($\overline{\mathbf{x}}$)	m	18	44	26	41	26	37	36	29	32
ens. std. dev. ($\mathbf{s}$)	m	11	10	15	14	12	8	7	10	11

The analysis of the cross-sections showed that the maximum observed depths reached on average 6.8 m in September 2008. Simulated maximum tidal channel depths reached on average 6.1 m; however, the standard deviation at those locations is equal to 0.7 m. Thus, the maximum observed depth could be reproduced by the model with 68% probability of occurrence, corresponding to the interval of one standard deviation.

In order to determine which of the ensemble members may be responsible for the largest changes in the tidal channel in horizontal (north-south) and vertical directions, the following analysis has been carried out. The migration distance of the 4 m-isoline, as well as the thalweg[1] elevations in the tidal channel have been estimated in the defined cross-sections (see Figure 6.9), and the ensemble members responsible for maximum/minimum values have been identified.

In the vertical direction, the member 19 produced the smallest depths in the channel, which could be explained by the relative high settling velocity ($w_s = 1.140\,\mathrm{mm\,s^{-1}}$) and by the median grain size larger than the mean ($d_{50} = 210\,\mu\mathrm{m}$). With respect to the horizontal direction, the member 29 ($d_{50} = 211\,\mu\mathrm{m}$, $\tau_{cr} = 0.294\,\mathrm{N\,m^{-2}}$, $w_s = 0.442\,\mathrm{mm\,s^{-1}}$) produced the furthest northward migration of the north border of the channel in 4 out of 8 cross-sections. This set-up might lead to higher suspension of cohesive material (lower settling velocity) leaving mainly non-cohesive material in the channel (higher grain size), which seems to improve the migration. The smallest northward migration of the south border of the channel in 7 out of 8 cross-sections was achieved by members presenting higher settling velocity (larger than mean) and lower critical bed shear stress (smaller than mean).

[1] The line of lowest elevation within a valley or watercourse.

6.2 Ensemble 2012 - 2014

6.2.1 Initial conditions

The second simulation starts in June 2012 and ends in March 2014. Instead of covering the whole tidal flat and surroundings nearby the MDPI, measurements during this period are available at the southern region relative to the MDPI. During this period, the TF channel tends to retreat and, simultaneously, a larger channel in the south becomes more important to the local tidal-channel system.

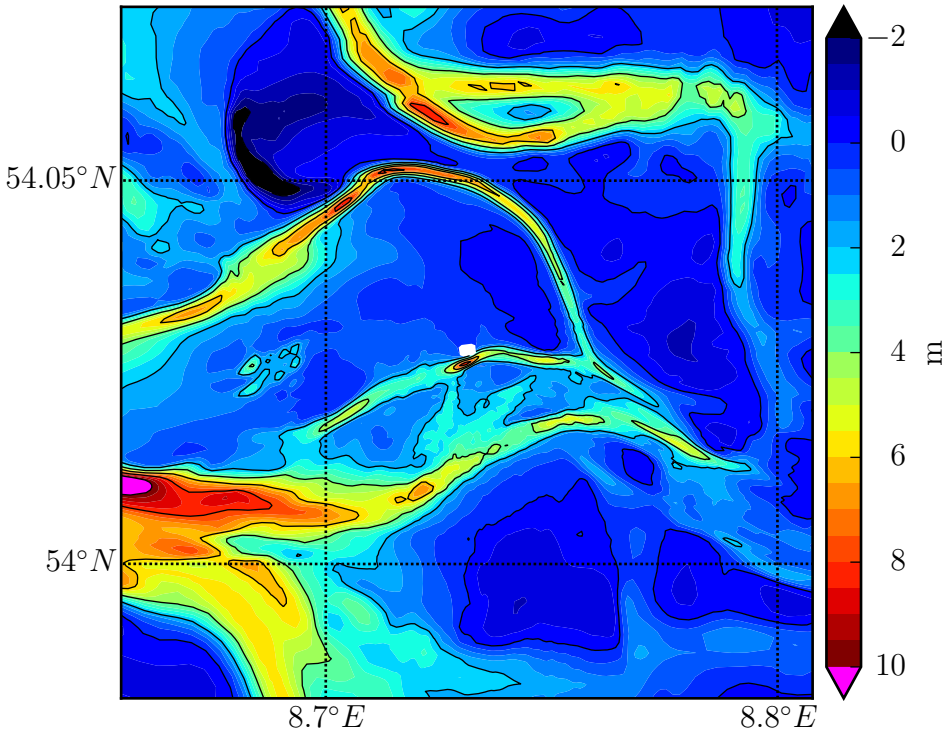

Figure 6.10: Model start bathymetry on 01.06.2012.

The starting bathymetry of the model has been reconstructed based on the most recent available measurements up to 01.06.2012. It means that, for each grid cell the most up to date measurement has been assigned (if available). Finally the whole data set has been interpolated in order to avoid gaps or discontinuities. The second ensemble simulation goes from 01.06.2012 to 01.03.2014, so that the morphology has enough time to develop itself, and the start and final bathymetries can be compared to measurements. The initial model bathymetry is shown in Figure 6.10.

Similarly to the first ensemble simulation, water level and wave spectrum information are prescribed at the MDPIM open boundaries. In addition, the meteorological forcing from the DWD regional model complements the set-up of the driving forces.

6.2.2 Meteorology

Meteorological conditions during the simulation period are provided by the DWD regional model data. The wind rose at the MDPI (Figure 6.11) shows that the predominant wind direction is from SW to SSW (total frequency of ca. 20%). Also, it can be seen that strong winds exceeding 50 km h^{-1} were observed.

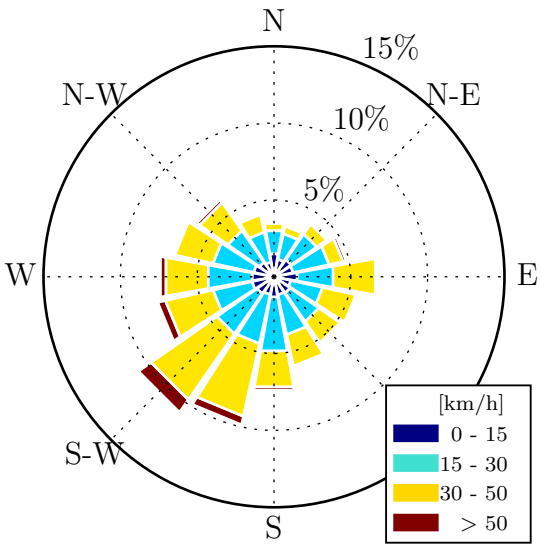

Figure 6.11: Wind rose from DWD meteorological model at the MDPI location from 06.2012 to 03.2014.

The conditions represented by the wind rose now indicate more clearly that storm winds are mainly coming from the SW direction and with a larger probability than in the previous period. During the two-year period, the most important storms reported in Northern Europe are listed in Table 6.3. From the five severe winter storms identified between 2012 and 2014, two of them (Christian and Xaver) produced the most severe flooding and damage in the North Sea.

Energy analysis

In order to estimate how much the meteorological forcing affects model results in the study area, the concept presented in Section 4.2 is applied here.

In Figure 6.12 the results show that storms Jill and Xaver significantly contributed to the energy transferred to the model. The difference between them is that storm Jill (from east) damps down the energy from tides and produces a negative effect on shallow areas (where flood tide is not able to reach anymore), whereas west storms like Xaver add energy to the total budget, as also presented in the previous simulated period.

Table 6.3: Severe European winter storms between 2012 and 2014.

name	date	description
Jill	22-26.3.2013	This polar high-pressure system produced severe snowstorms with strong easterly winds in Northern Europe.
Christian	26-31.10.2013	The storm's intensity was compared to the Great Storm of 1987 and the storm Daria of 1990. It hit northern Europe with gusts of up to 192 $\mathrm{km\,h^{-1}}$ recorded in Denmark.
Nordic storm series	13.11-19.12.2013	A series of storms affected the Nordic Nations during November and December as high pressure over Europe directed westerly flow over the Atlantic.
Xaver	4-11.12.2013	Force 12 winds were forecast over the North Sea on December 5. The system impacted densely populated areas in the UK, Denmark, Sweden, Germany and Poland.
Atlantic winter storms	17.12.2013-20.2.2014	More than 10 storm events have been registered during this period all over in Europe.

Source: Thornton et al. (2016).

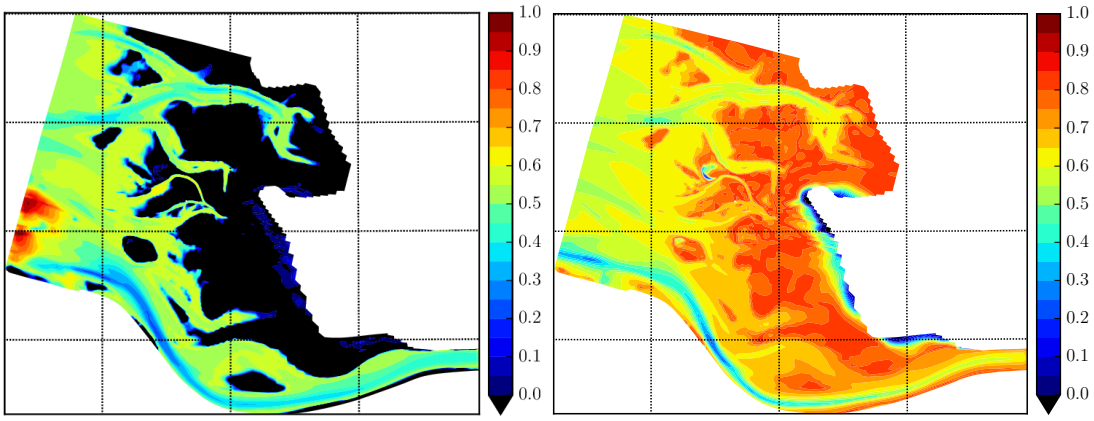

(a) Jill (b) Xaver

Figure 6.12: Energy ratio due to the meteorological component from storm events between 2012 and 2014.

6.2.3 Results

The mean $\overline{\mathbf{x}}$ (top) and the standard deviation $\mathbf{s}$ (bottom) of the ensemble at the end of the simulation are shown in Figure 6.13. Values for the latter in terms of bed level variation can exceed 1.5 m in tidal channels, but generally locations deeper than 2 m already present larger variations. In the vicinity of the MDPI (figure centre) large deviations from the mean are also observed.

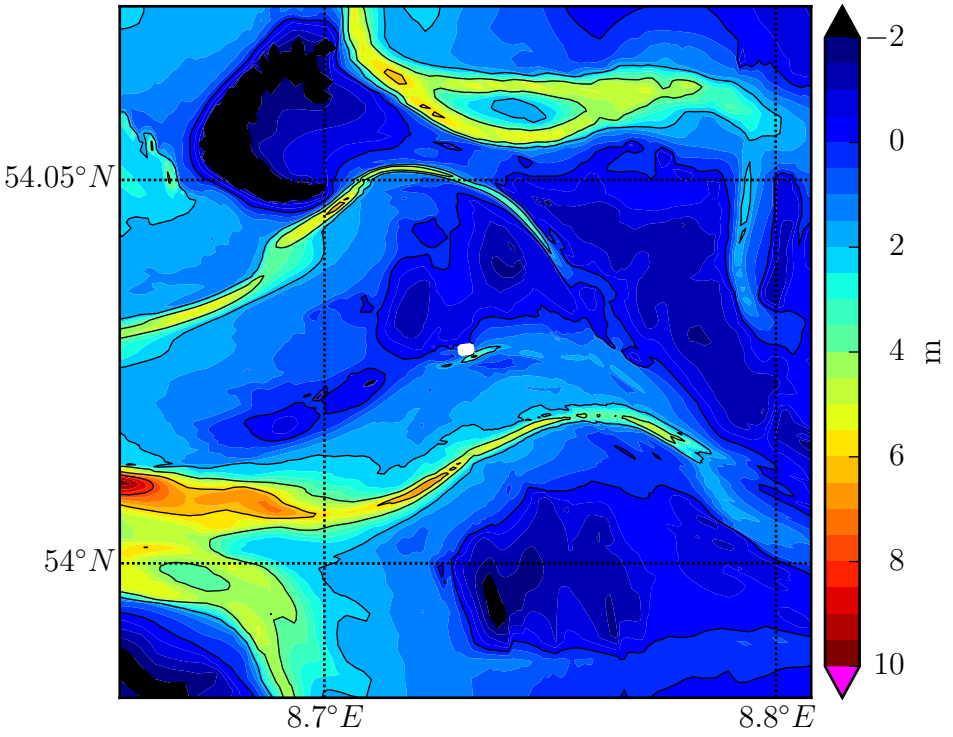

(a) mean

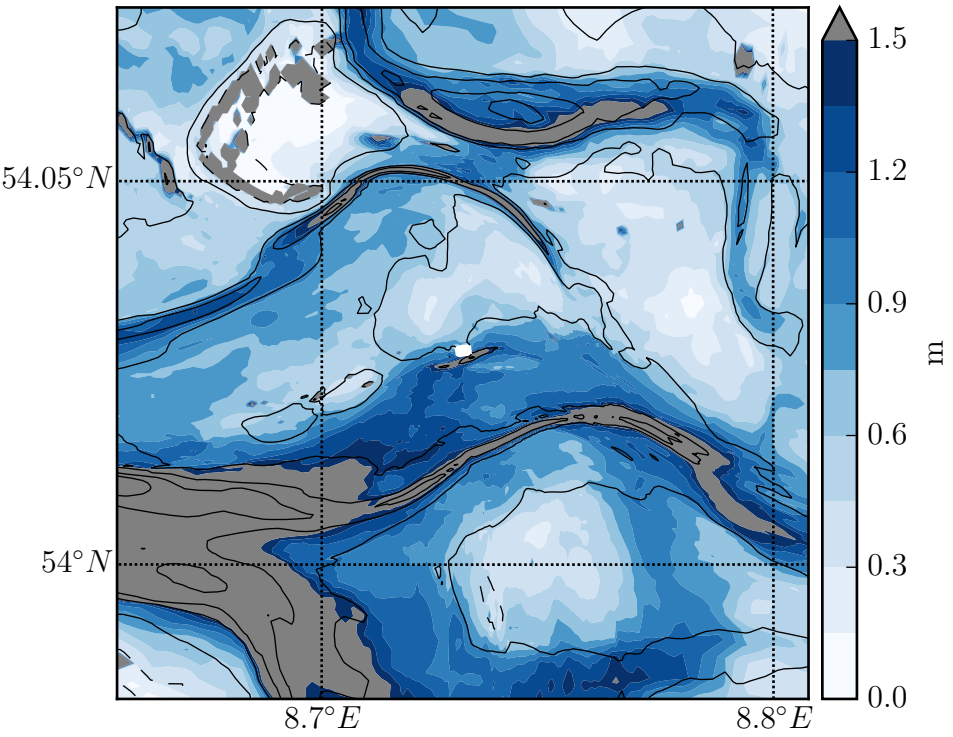

(b) standard deviation

Figure 6.13: Ensemble results of model bathymetry on 01.03.2014.

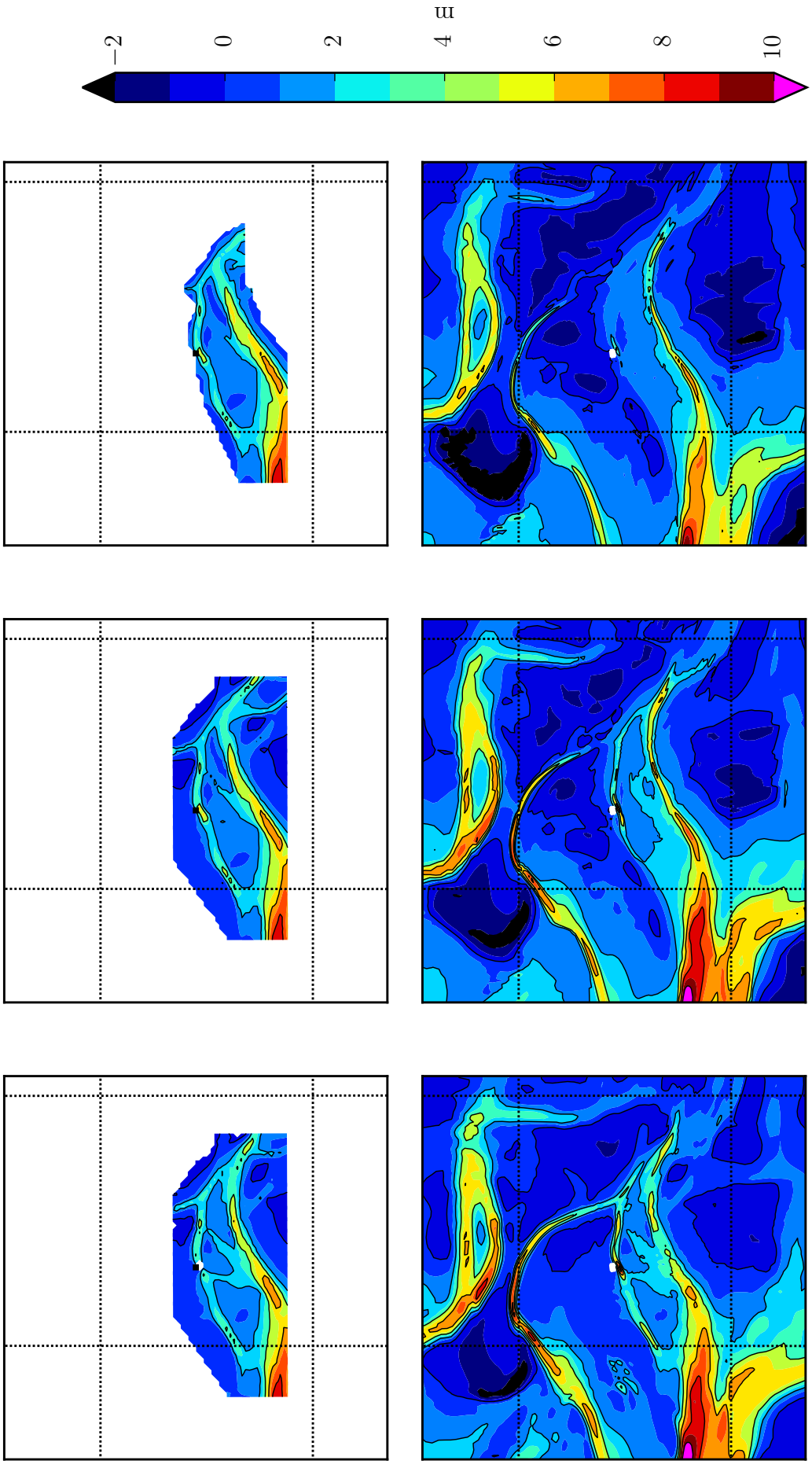

(a) June 2012 (b) June 2013 (c) March 2014

Figure 6.14: Bathymetric evolution during the morphodynamic ensemble period of 2012-2014. Measurements (top) and model (bottom).

The comparison of measured and (mean) modelled bathymetries for June 2012, June 2013 and March 2014 is presented in Figure 6.14. Measurements show that the three areas (sediment banks) above 2 m NHN observed in 2012 tend to merge to form a long structure. As a result the flow is split between the TF and the SC. During this period the NF decreases in width and tends to close its connection to the TF.

Contrary to measurements, model results show a different situation. Although the aforementioned three areas in the model also merge in 2013, the entire area between the TF and the SC presents sedimentation and the TF practically disappears. The NF retreats already during the first simulated year, and in 2014 measurements indicate that its connection to the TF channel is almost closed.

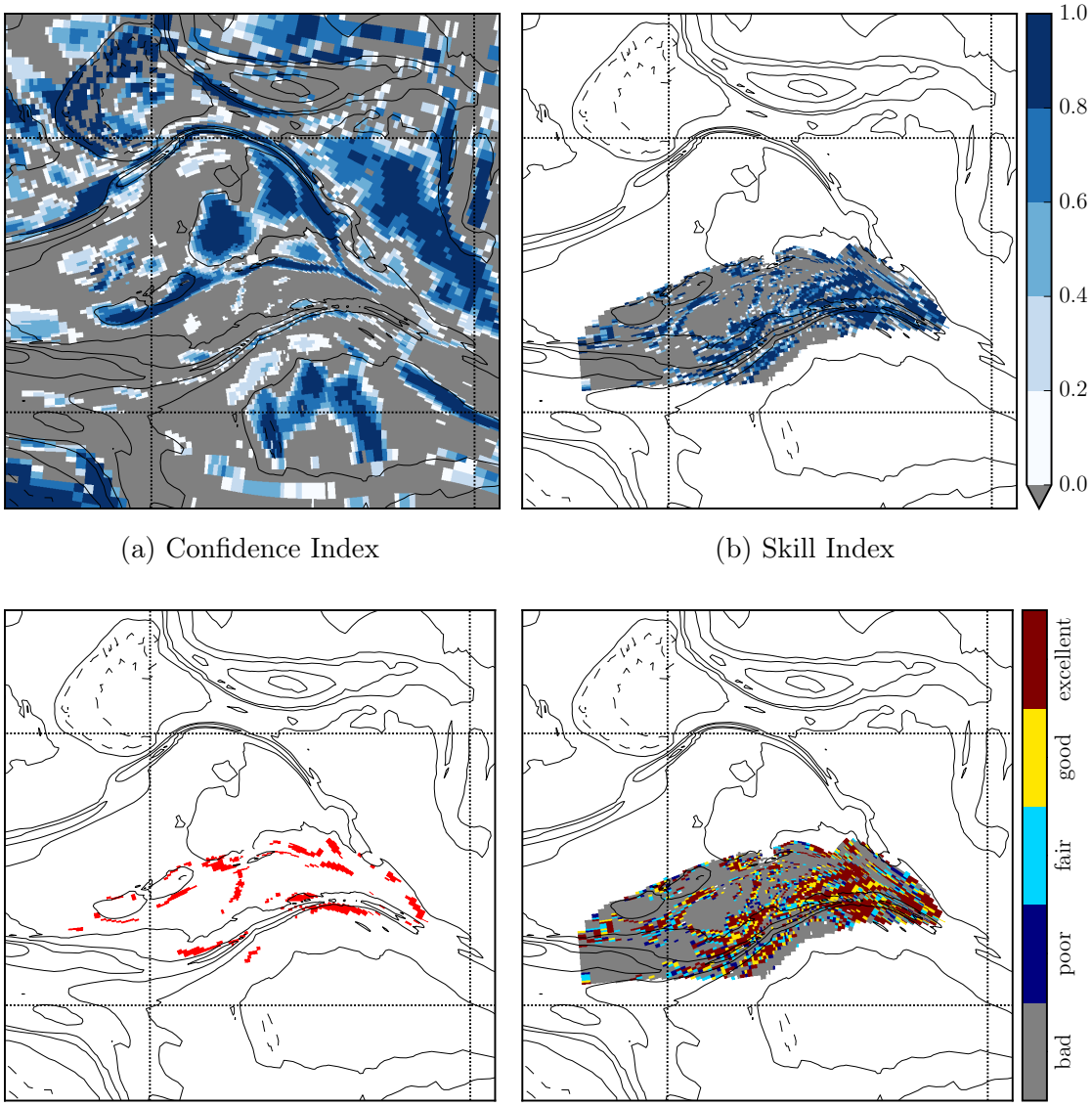

(a) Confidence Index

(b) Skill Index

(c) confidence and skill overlapping

(d) skill qualification

Figure 6.15: Performance of the morphodynamic ensemble simulation 2012-2014.

As previously explained, the evaluation of model performance is done by calculating indexes of confidence and skill. The Confidence Index (CI) indicates where the ensemble presents a small deviation of the bed level changes with respect to their mean. Figure 6.15a shows similar results as in the first simulated period, where positive CI values are found mainly in tidal flat areas (above 0 m NHN).

The Skill Index indicates where and how the ensemble mean of the bed level changes deviates from the measured bed level changes with regard to measurements. Figure 6.15b shows that the model performs better at the tidal channel located south from the TF, which will be referred here as the South Channel (SC).

The combination of the confidence and the skill results in areas in which both indexes meet the condition for acceptance, defined for CI $>$ 0 and SI $>$ 0.3 (Figure 6.15c). The model skill qualification according to Table 4.2 is presented in Figure 6.15d. Because the model performs best in the west part of the SC, a cross-section analysis will be presented later for this region.

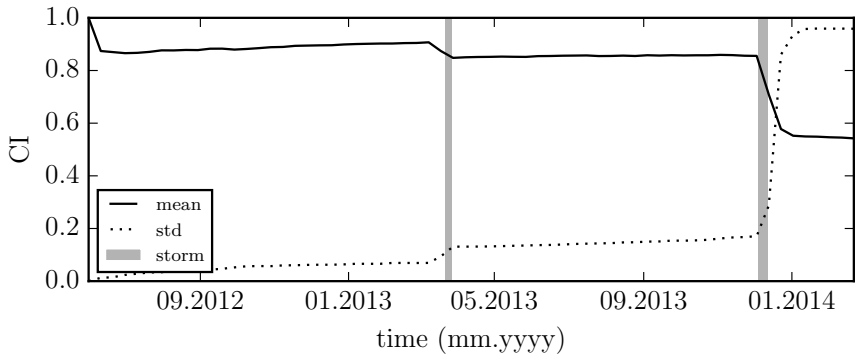

Figure 6.16: Time series of the space-averaged Confidence Index from 2012 to 2014.

With respect to the evolution in time, the Confidence Index (CI) analysis presents two significant drops (Figure 6.16). The storm periods are the same ones represented in the energy levels of Figure 6.12: storm Jill and storm Xaver. The second drop in the CI value is due to storm Xaver, the strongest storm that occurred within the simulation period.

The Skill Index (SI) evolution for the available measurements is shown in Figure 6.17. Only positive SI values were considered. Similarly to the analysis presented for the space-averaged Confidence Index, the model skill time evolution was addressed. Results show that the model skill increases in time (partial result). The overall skill is also larger than 0.6, meaning *good* skill according to Table 4.2.

The analysis of cross-sections where the Skill Index (SI) is considered to be acceptable is presented in Figure 6.18. The cross-sections are located in regions

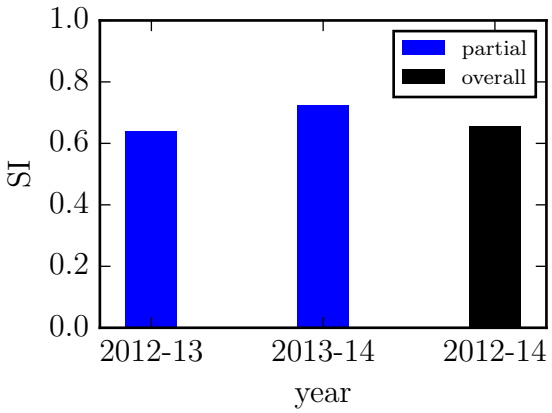

Figure 6.17: Space-averaged Skill Index between 2012 and 2014.

where SI > 0. The red solid lines represent the modelled mean bathymetry from the ensemble (solid) and from the benchmark (dashed), which represents the model set-up with the mean parameter values $\overline{\mathbf{x}}$. The light red shaded areas represent the 68% prediction interval (one standard deviation), assuming a Gaussian distribution for model results. The SI values (blue bars on the bottom) show locations in which the modelled bed level changes are in agreement with the measured ones. Dark blue colours indicate the skill from the ensemble mean and the light blue colours represent the skill considering the ensemble spread.

Similar to the first simulation period, measurements show a more pronounced migration on the eastern cross-sections (G and H) than in the western part (A and B). Although in the model the migration on the east side is not well predicted, the west part of the channel moves towards north.

The measured and mean simulated migration distance of each cross-section, as well as the ensemble standard deviation are presented (Table 6.4). The model was able to reproduce the migration northwards, but the rate of migration is on average ca. one third smaller than the measured one. Also during this simulation period the calculated standard deviation of the tidal channel migration (26 m) plus the mean value corresponds to half of the observed migration (75 m).

Table 6.4: Cross-section migration distance of the 3 m-isobath.

CS	unit	A	B	C	D	E	F	G	H	mean
observed	m	68	43	73	93	121	194	269	347	151
ens. mean ($\overline{\mathbf{x}}$)	m	41	39	54	36	50	57	64	54	49
ens. std. dev. ($\mathbf{s}$)	m	25	21	30	37	45	14	25	14	26

The analysis of the cross-sections showed that the maximum observed depths reached on average 4.7 m in March 2014. Simulated maximum tidal channel depths reached on average 4.0 m, whereas the standard deviation at those loca-

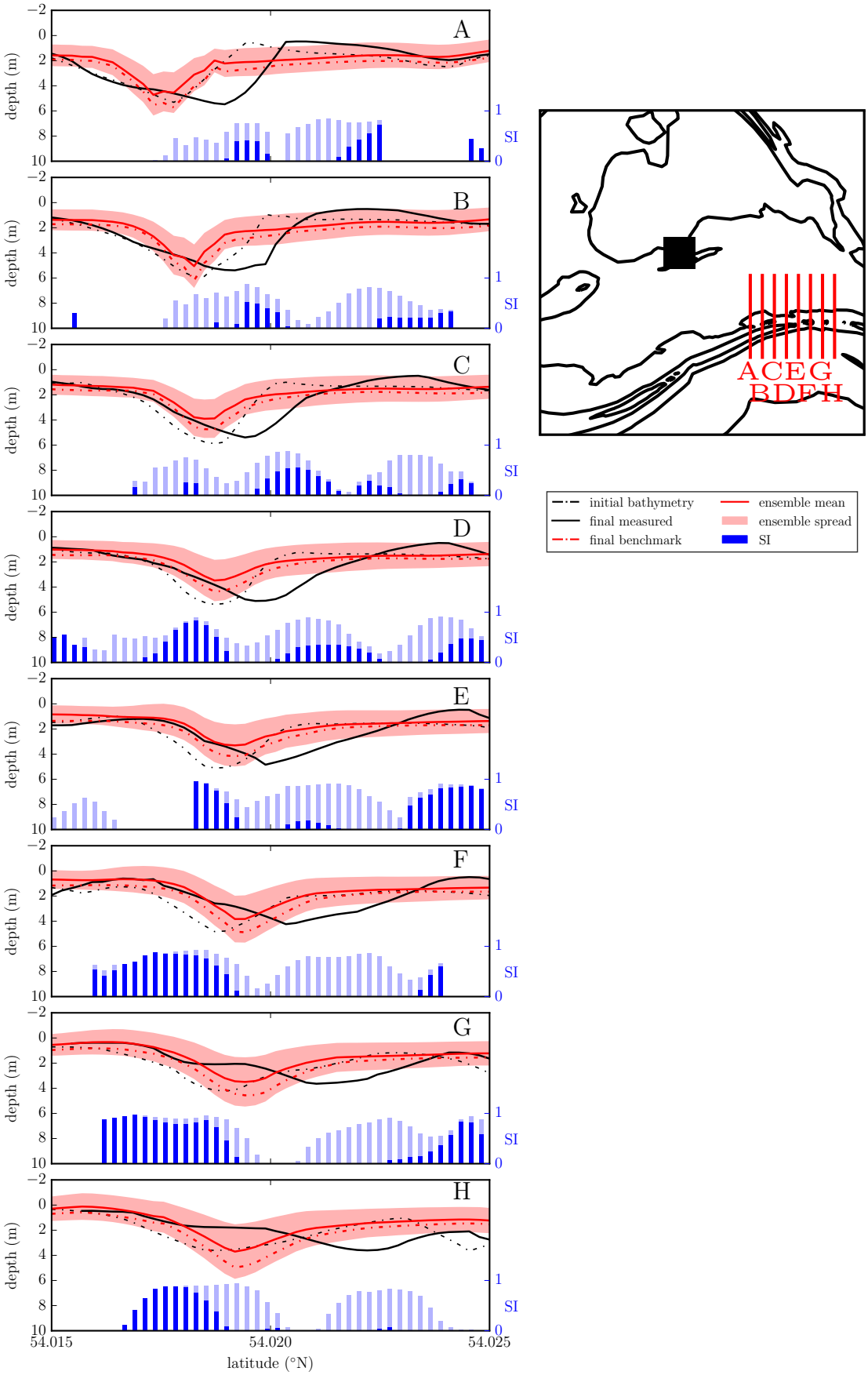

Figure 6.18: Bed level evolution between 06.2012 and 03.2014 at cross-sections A to H (right).

tions is equal to 1.8 m. The rather larger deviation presented in the simulation can be associated with the overall channel depth, much shallower than the TF channel. In this case the consolidated mud layer, found at 7 m NHN, does not limit the vertical erosion in the tidal channel.

The analysis previously presented has also been carried out to determine which of the ensemble members are responsible for the largest changes in the tidal channel in horizontal (north-south) and vertical directions. The migration distance of the 3 m-isoline, as well as the thalweg elevations in the tidal channel have been estimated in the defined cross-sections (see Figure 6.18), and the ensemble members responsible for maximum/minimum values have been identified.

In the vertical direction, results indicate a clear difference in the behaviour of the west (A to D) and east (E to H) cross-sections. On the west side, the member 27 produced the smallest depths in the channel, probably due to the relative large median grain size ($d_{50} = 237\,\mu m$). On the east side, where the channel is flatter, the member 5 is responsible for the smallest depths. In this case the relative high settling velocity ($w_s = 1.660\,mm\,s^{-1}$) favors sedimentation. The largest depths were produced in 5 out of 8 cross-sections by members with values smaller than the mean for the median grain size and for the settling velocity. Smaller grain size and settling velocity favors erosion, which explains larger depths in the channel.

With respect to the horizontal direction, members that produced the greatest and the smallest migrations present values larger than the mean for the median grain size and for the settling velocity. The greatest migrations of the north border in 5 out of 8 cross-sections, and the smallest migrations of the south border of the channel in 6 out of 8 cross-sections northward have been identified. This indicates that the tidal channel widened to the north-south direction, and that less suspension of cohesive material (higher settling velocity) together with larger non-cohesive grains (higher grain size) lead to such situation.

6.3 Discussion

General

The ensemble approach allows the interpretation of model results with an intrinsic probability due to lack of accuracy in model formulations and inputs. As presented in Chapter 5, there is a standard procedure before one is able to produce reliable morphodynamic results; i.e. the process of hydrodynamic model calibration should be followed by the sediment transport model calibration. But even when these steps are successful, the model may be unable to predict morphological changes adequately simply because the number of unknown variables

in the system still remains high.

It was shown that the applied process-based model is able to reproduce reasonably well most physical processes regarding hydrodynamics and suspended sediment transport. Even though hydrodynamic processes take place in a much smaller time scale than morphological changes, storm events are responsible for increasing the "entropy" in coastal environments in a small period of time. The results from the morphodynamic ensemble indicate that storms influence the overall outcome to some extent, because their effect on the ensemble was much more significant than during normal weather conditions.

The morphodynamic ensemble results should be always interpreted as the most probable final state (ensemble mean) for the bathymetry with an intrinsic uncertainty (ensemble deviation). Also, the analysis of confidence based on bed level changes provides information of where and how much the ensemble deviates from its mean; analogously, the analysis of skill provides information on the location and extent of observations. However, it is difficult to draw general conclusions based on the presented model confidence and skill (Figures 6.6 and 6.15), since the performance is quite scattered over the domain. The ensemble results have shown that the model is able to reproduce the tendencies observed in the tidal channels to some extent, based on skill qualification. On the tidal flats the situation is different. Although ensemble simulations produced quite consistent results in those areas (high Confidence Index), the model was not able to reproduce the measured bed level changes satisfactorily (low Skill Index).

With respect to the cross-section analysis, simulated results have shown a consistent tidal channel migration to the north in both ensembles (Figures 6.9 and 6.18). Measurements confirm the same trend, but with a much more pronounced migration. On average the tidal channel migration was underestimated by a factor of 3, and the reason for that might lay on physical processes on the tidal flat that are not well represented in the model. Further discussion is presented later on tidal flat simulation.

The considered model parameters for the morphodynamic ensemble have been chosen on the basis of their effect on sediment concentrations. Thus, modelled concentrations could be directly and easily assessed when compared to measurements. The critical bed shear stress and the settling velocity produced significant variations in SSC, whereas the median grain size affected mainly the bedload.

Sediment transport

Measurements related to suspended sediment concentrations are available only in tidal channels, because the ability to measure those properties on the tidal flats remains one of the greatest challenges in sediment transport research. In fact,

even studies on the calibration of a flow model on the tidal flats are not known to the author. Therefore the sediment transport model has been calibrated based on processes taking place in tidal channels only.

For instance, bedload and suspended load have been verified/calibrated to fit measured concentrations that do not necessarily fit those on the tidal flats. Figure 6.19 shows how the relation between these two modes of sediment transport varies on the tidal flat (blue) and in the tidal channel (red).

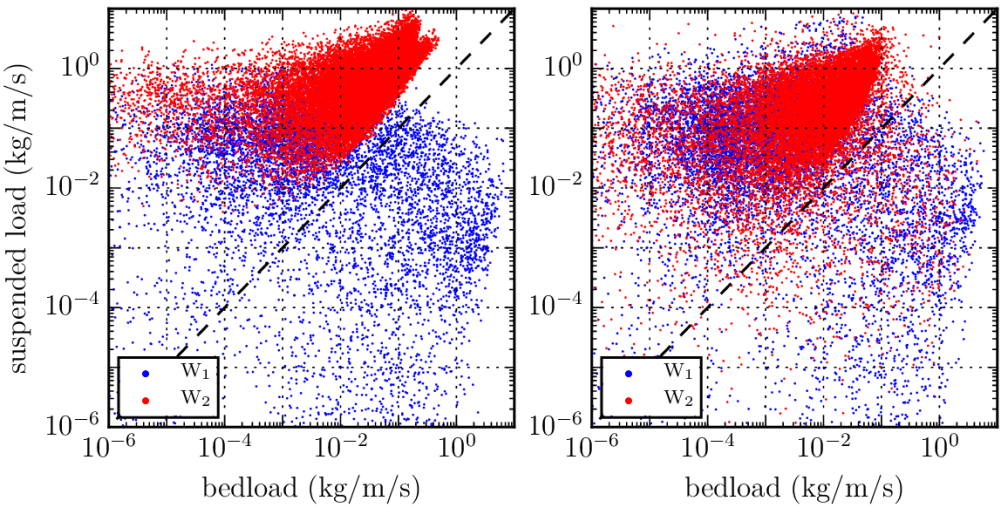

(a) 2006-2008 (b) 2012-2014

Figure 6.19: Relation between modelled bedload and suspended load on tidal flat (blue) and in tidal channel (red).

On the tidal flat bedload appears to be as important as suspended load for sediment transport, whereas in the tidal channel suspended load is dominant. Another difference observed is that during the period 2006-2008 (Figure 6.19a) suspended load is always larger than bedload in the channel, while in 2012-2014 (Figure 6.19b) sometimes bedload is larger. This can be explained by the near-bed orbital velocities, which are depth-dependent and directly affect the bed shear stress due to waves. Because the model has been calibrated in the tidal channels, the relation between modelled bedload and suspended load as shown in Figure 6.19 cannot be completely verified.

By looking at the bed shear stresses from currents and waves (Figure 6.20), it can be concluded that (1) the shear stresses affecting the seabed are mainly produced by currents during normal conditions, and (2) during storms both current- and wave-induced bed shear stresses are enhanced, but the latter is larger (roughly one order of magnitude) on the tidal flats. The grey-shaded area represents the shear stresses below the critical value estimated according to Shields criteria (Equation (4.27)) for sediments with $d_{50} = 200$ µm.

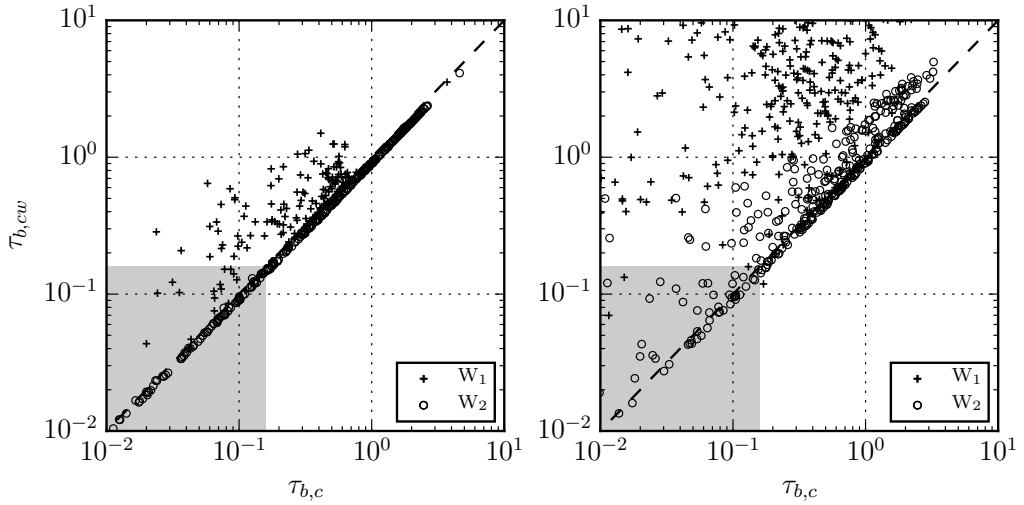

(a) normal conditions (b) storms

Figure 6.20: Relation between modelled bed shear stress from currents ($\tau_{b,c}$) and maximum bed shear stress from currents and waves ($\tau_{b,cw}$) on tidal flat (+) and in tidal channel (∘).

Thus, the higher bedload rate on the tidal flat than in the tidal channel (see Figure 6.19) can be probably explained by the larger exposure to wave action, typical to shallow water areas specially during storms. The excessive sedimentation predicted by the model on the tidal flats - not confirmed by measurements - is an indication that not all processes are properly represented.

Meteorological conditions

Through energy analysis the contribution of meteorological forcing on shallow areas, especially on tidal flats, has been evaluated. Wave-induced potential energy and kinetic energy from currents have been calculated and finally the total sum has been analysed. From those results, it was concluded that during storm events shallow areas receive more than 50% of the total energy introduced in the domain from the meteorological component. During normal weather conditions this relation normally does not exceed 10%, confirming that the study area is tide-dominated.

With regard to the evolution of the space-averaged Confidence Index (CI), analysis indicated that drastic changes in the CI are apparently caused by a severe storm surge. Also during the winter of 2006-2007 strong storms have been observed in the North Sea, but they did not produce significant changes based on CI results. In order to clarify this issue, a second morphodynamic ensemble simulation has been carried out, in which the period started on July 2007. The outcome is shown in Figure 6.21 confirming the same effect from storm Tilo

(left shaded area) followed by storm Emma (right shaded area). It means that initial conditions do not change the outcome, and also that the propagation of errors is probably not responsible for such behaviour. The remaining unanswered question is, why winter storms from 2006-2007 apparently did not affect the model in terms of confidence, although energy levels during storms seem to produce similar effects?

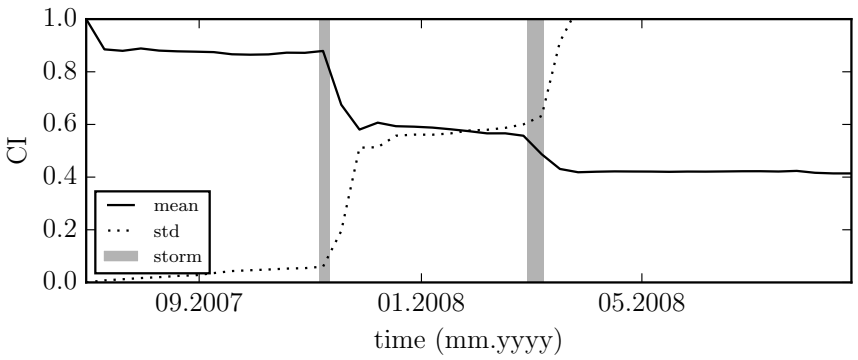

Figure 6.21: Time series of the space-averaged Confidence Index from 2007 to 2008.

In both ensemble simulations a similar behaviour was identified: the averaged index is very sensitive to meteorological forcing, meaning that model performance is affected significantly. However, the conditions that may lead to significant decrease in model confidence could not be fully explained. The example of storm Tilo (November 2007) affected model results significantly in both one- and two-year simulations, whereas storm Kyrill (January 2007) did not. This could be related to a pre-existing mean sea level pressure gradient centred in the German Bight and Southern Baltic Sea that produced larger impacts on inland than on the coast (Fink et al., 2009), but further investigation is required.

Tidal flat simulation

The fact that the model did not perform well on the tidal flats left open questions, and the analysis of model results with respect to the Brier Skill Score led to some answers. The effect of the tide on model results has been estimated by running the benchmark model driven by tide only, and then by comparing to the benchmark model driven by all driving forces. The comparison consisted in calculating the space-averaged BSS of a 1m-layer every 0.5 m from the surface down to the sea bottom. The results of the analysis are shown in Figure 6.22.

In Figure 6.22a small differences between the benchmark and the tide simulation are found below ca. 3 m. Above that, the simulation only with tide presents a quasi-constant BSS, while the benchmark presents an increasing BSS from the surface down to ca. 2 m. This result can be explained by wind-generated waves

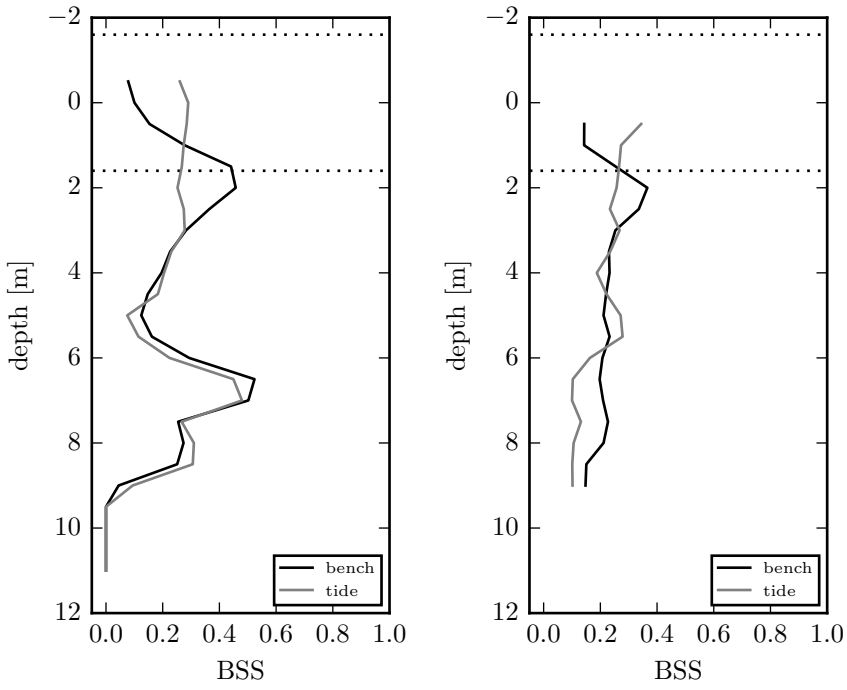

(a) 2006-2008 (b) 2012-2014

Figure 6.22: Space-averaged BSS from surface (0 m NHN) to sea bottom (12 m NHN).

acting within the tidal range (black dotted lines). This is further complicated by the process of drying/flooding. The effect of the wave-enhanced bed shear stress combined with the drying/flooding process seems to produce bad skill, but the skill improves as one moves away (deeper) from the influence of waves. The maximum BSS value is reached around 2 m.

In Figure 6.22b a similar relation between the benchmark and the tide-driven model is observed above ca. 3 m. The maximum BSS value also occurs around 2 m. While between 3 m and 6 m results do not differ much, below 6 m the benchmark performs better. This might be related to the size of the measured tidal flats from both simulated periods (see Figures 3.8 and 3.9). Measurements from the first period cover a wider tidal flat (where the MDPI is located) and its surroundings, including the TF and NF channels. Measurements from the second period cover only smaller tidal flats and neighbour tidal channels. Changes on the flats in the first case have a relatively limited effect on deeper areas, whereas in the second case waves affect tidal flats in the same proportion as they affect deeper areas.

Some aspects from model performance on the tidal flats are considered to be critical. First, sediment transport and morphodynamic models are not able to represent all the relevant processes taking place on the tidal flats correctly, because the empirical equations do not fully describe them and proper measuring techniques are not available (e.g. bedload). Second, the process of drying/flooding

grid cells in the model might not be able to capture the correct effect on sediment transport. Third, waves are known to play an important role in shallow waters, where the orbital velocities increase significantly the bottom shear stress, but their actual effect on sediment might not be well represented. And fourth, extreme weather events are directly related to sediment transport along coasts, but little is known about their real impact to morphodynamic evolution.

Final remarks

The application of the morphodynamic ensemble technique in the presented study is based on two initial assumptions: (1) the uncertainty of the sediment transport model parameters can be described by a Gaussian distribution, and (2) the model results, which are functions of those parameters, also follow a Gaussian distribution. These assumptions imply that the achieved model results for bathymetry range within a mean value ($\overline{\mathbf{x}}$) plus or minus the standard deviation ($\mathbf{s}$) with a corresponding defined probability. While assumption (1) is a common representation of model errors as prior distributions (Schmelter et al., 2011, 2012), assumption (2) is not. This means that the combination of different sets of parameters relevant to sediment transport could result in different morphological evolution, which may not be necessarily described by the distribution assumed for those parameters. Yet, the standard deviation is calculated for each grid point and accounts for the ensemble accuracy in space.

Nguyen (2015) performed similar morphodynamic simulations in the study area. She used a different method which did not account for the uncertainties of sediment transport parameters, but based on input reduction techniques to save on computational time. This method produced slightly better results with regard to the migration of the tidal channel than the benchmark simulation (here presented) achieved. However, the time period selected for the accelerated simulation was characterized by enhanced energy conditions so that morphodynamics get stronger. Moreover, the method discards storm events due to their low temporary representativeness. Therefore, simulation results of both studies are not comparable.

Accelerated morphodynamic simulations over larger time periods are frequently used and make more sense. In a recent study Dam et al. (2016) have successfully applied a process-based model to simulate 110 years of morphological evolution in the Dutch coast. They applied a reduced model driven only by tidal forcing to simulate non-cohesive sediment, and modelled morphological evolution with an acceleration factor of 24.75. Their results show very good agreement with measured bathymetric evolution. The reason for that is probably due to the characteristic of the study area: a confined estuary, composed mainly by non-

cohesive sediment, where tide is the main driving force.

The results from the application of the ensemble method to morphodynamic simulations point out that the range of variations produced by sediment transport and morphodynamic models cannot sufficiently cover all the physical processes taking place in a tidal channel system. Furthermore, two main situations have been identified which the model is not able to simulate satisfactorily: (1) processes related to sediment transport taking place on tidal flats (e.g. suspended load, bedload, wave stirring, drying/flooding); and, (2) morphological changes produced by storm events.

Chapter 7

Conclusions and recommendations

7.1 Conclusions

The governing processes responsible for the morphodynamic migration of tidal channels by means of a process-based numerical model were investigated. In order to take model uncertainty into account a probabilistic approach was used to clarify the variability in sediment transport model parameters. The probabilistic approach was applied to the morphodynamic model and the results were statistically evaluated.

Two kinds of uncertainties were addressed: (a) errors related to the estimation/calibration of sediment transport parameters, and (b) errors due to imperfections in the model formulations and approximations. Based on statistical analysis, confidence and skill indexes, model performance was assessed. The analysis of performance showed that the model can simulate morphological evolution better in the tidal channels than on the tidal flats. The cross-section analysis showed that the model produces a consistent tidal channel migration to the north in agreement with observations, even though the migration was underestimated (in one third).

According to Confidence Index results on the tidal flats a high confidence is attributed to morphological evolution, which means that the ensemble produces similar results (low deviation) and it is not affected by the sediment parameter uncertainty considered. According to Skill Index results deep areas such as tidal channels present higher skill than shallow areas. The combination of the Confidence and Skill Indexes indicated that the predictive ability of the model is lower on the tidal flats during both simulated periods. Even though high confidence was indicated by the CI, skill in those areas was relatively low.

With respect to the sensitivity of sediment parameters, the effect of the variation of critical shear stress, settling velocity and median grain size on suspended

load and bedload was evaluated. The attributed uncertainty due to critical shear stress resulted in ca. three times the SSC variation, relative to the benchmark value. The considered uncertainty due to sediment settling velocity resulted in more than two times the SSC variation. The uncertainty due to median grain size resulted in a not significant SSC variation, but in a bedload variation ca. one third larger. It is concluded that uncertainties regarding sediment characteristics should not be neglected neither in sediment transport nor in morphodynamic modelling. Thus, model performance analysis that take uncertainties into account is recommended.

Extreme weather events definitely play an important role in morphological evolution in a very short-term timescale (hours to days). In longer timescales these effects are usually not very clear and require exhaustive investigation. According to energy analysis, severe storm events are responsible for more than half of the total energy in the domain. Furthermore, the analysis of model confidence over time revealed that storm events decrease the confidence of model results and have a significant relevance on morphodynamic results for the selected study area and timescale. The decrease in model confidence is an indication that the simulation of storm effects is not correctly represented and, therefore, need further improvement.

With regard to tidal flats, simulations produced excessive sedimentation in some regions where small variation was observed. The possible reasons related to low model performance on tidal flats are:

- The sediment transport and morphodynamic models are not able to represent all the relevant processes taking place on the tidal flats correctly, because the empirical equations do not fully describe them and proper measuring techniques are not available.

- The process of drying/flooding grid cells in the model might not be able to capture the correct effect on sediment transport.

- Waves are known to play an important role in shallow waters, where the orbital velocities increase significantly the bottom shear stress. However, their actual effect on sediment might not be well represented.

- Although extreme weather events are directly related to sediment transport along coasts, little is known about their real impact to morphodynamic evolution.

In summary, the results achieved underline the recent difficulties to reproduce the complexity of sediment transport processes in the Wadden Sea through

numerical modelling. Although the observed migration direction of the Trischenflinge tidal channel could be correctly simulated by the model nearby the MDPI, the rate of migration was underestimated. Compared to traditional deterministic modelling, the ensemble method applied to a morphodynamic model may provide more detailed information on how reliable the model results are with regard to uncertainty ranges from the sediment transport parameters. Morphodynamic ensemble results pointed out that the physical processes taking place in the tidal channel system investigated cannot be entirely described by the range of variations simulated by the sediment transport and morphodynamic models. Finally, it was identified that the simulation of processes taking place on tidal flats related to sediment transport, and morphological changes produced by storm events are current deficiencies in morphodynamic modelling that demand improvements. Therefore, further development of measuring techniques with respect to sediment transport on the tidal flats is needed. Also, new mathematical relations for better describing sediment dynamics under storm conditions should be investigated.

7.2 Recommendations

Sediment transport on the tidal flats

According to the evaluation done, the simulation of morphodynamic evolution on tidal flats proved to be less successful than in tidal channels. One of the main reasons is the lack of understanding and measurements of key processes of sediment dynamics. Also, the drying and flooding of tidal flats together with wave-stirring-induced sediment suspension seems to be poorly represented in the model and data for calibration of such processes are not available. Therefore, a more detailed investigation related to sediment transport processes on the tidal flats and more appropriate measuring techniques are needed.

Sediment transport under storm conditions

Simulation results point out that meteorological forcing of storms plays an important role on morphodynamics. The current study did not focus on determining to which extent and specific conditions it might affect sediment transport. Thus, the investigation of improved mathematical relations for suspended and bedload sediment transport under storm conditions is required.

Input and model reduction methods

The morphodynamic ensemble method makes use of the Monte Carlo Simulation approach. This means that the larger the number of simulations, the

more reliable the results are. If both the morphodynamic ensemble and the input reduction methods are combined, a larger number of simulations could be completed with the same computational power. Of course, the question lies in which and how inputs can be reduced. Hence, the combination of the morphodynamic ensemble and the input/model reduction methods is an interesting research topic.

Bayesian morphodynamic model

The morphodynamic ensemble method was inspired by Bayesian statistics. However, this approach has been mainly applied to one-dimensional sediment transport models. The reason for that is the computation of the posterior distribution of Bayesian models, whose analytic solution is impractical. An alternative is to apply a Markov Chain Monte Carlo method and approximate the posterior distribution. Therefore, an investigation on Bayesian statistics applied to simplified morphodynamic models would be also an interesting research topic.

Morphodynamics of unconfined coastal areas

The current study has focused on the German Wadden Sea, a tidal flat region only bounded by land on the east and the south. This means that the study area is subjected to the effect of wind and waves coming from north to west. Several examples of morphodynamic simulation of confined regions, e.g. tidal inlets and tidal basins, can be found in the literature. In those cases, usually the main driving force is the tide and simulated processes can be simplified significantly. Further work on the morphodynamics taking place on unconfined coastal areas subjected to the influence of various driving forces is needed.

Bibliography

Apel, J. R. (1987). *Principles of Ocean Physics*. International Geophysics. Elsevier Science.

Barnes, M. P. and Baldock, T. E. (2007). Direct bed shear stress measurements in laboratory swash. In *Journal of Coastal Research*, volume 50, pages 641–645. Coastal Education and Research Foundation.

Barnes, M. P., O'Donoghue, T., Alsina, J. M., and Baldock, T. E. (2009). Direct bed shear stress measurements in bore-driven swash. *Coastal Engineering*, 56(8):853–867.

Beets, D. J. and van der Spek, A. J. (2000). The Holocene evolution of the barrier and back-barrier basins of Belgium and the Netherlands as a function of late Weichselian morphology, relative sea-level rise and sediment supply. *Geologie en Mijnbouw*, 79(1):3–16.

Bosboom, J. and Reniers, A. J. H. M. (2014). Scale-selective validation of morphodynamic models. *Coastal Engineering*.

Bosboom, J., Reniers, A. J. H. M., and Luijendijk, A. P. (2014). On the perception of morphodynamic model skill. *Coastal Engineering*, 94(0):112–125.

CERC (1984). *Shore protection manual*. Dept. of the Army, Waterways Experiment Station, Corps of Engineers, Coastal Engineering Research Center.

Chang, C., Yang, J., and Tung, Y. (1993). Sensitivity and uncertainty analysis of a sediment transport model: a global approach. *Stochastic Hydrology and Hydraulics*, 7(4):299–314.

Cleveringa, J. and Oost, A. P. (1999). The fractal geometry of tidal-channel systems in the Dutch Wadden Sea. *Geologie en Mijnbouw*, 78(1):21–30.

Dalrymple, R. W., Zaitlin, B. A., and Boyd, R. (1992). Estuarine facies models: conceptual basis and stratigraphic implications: perspective. *Journal of Sedimentary Research*, 62(6).

Dam, G., Wegen, M., Labeur, R. J., and Roelvink, D. (2016). Modeling centuries of estuarine morphodynamics in the Western Scheldt estuary. *Geophysical Research Letters*, 43(8):3839–3847.

Darby, S. and Sear, D. (2008). *River Restoration: Managing the Uncertainty in Restoring Physical Habitat*. Wiley.

Dastgheib, A. (2012). *Long-term process-based morphological modeling of large tidal basins*. PhD thesis, Delft University of Technology.

de Vriend, H. J., Capobianco, M., Chester, T., de Swart, H. E., Latteux, B., and Stive, M. J. F. (1993). Approaches to long-term modelling of coastal morphology: a review. *Coastal Engineering*, 21:225–269.

de Vriend, H. J. and Ribbernik, J. S. (1996). *Mathematical modeling of meso-tidal barrier island coasts – Part II: Process-based simulation models*. Advances In Coastal And Ocean Engineering. World Scientific.

Deltares (2014a). *Delft3D-FLOW User Manual: simulation of multi-dimensional hydrodynamic flows and transport phenomena, including sediments*. Deltares.

Deltares (2014b). *Delft3D-WAVE User Manual: simulation of short-crested waves with SWAN*. Deltares.

Deltares (2016). *Deltares Open Source Platform*. Deltares. http://oss.deltares.nl/.

DWD (2016). *DWD Climate Data Center ftp-server*. Deutscher Wetterdienst. ftp://ftp-cdc.dwd.de/pub/CDC/.

Egbert, G. D. and Bennet, A. F. (1994). TOPEX/POSEIDON tides estimated using a global inverse model. *Journal of Geophysical Research*, 99(C12):24,821–24,852.

Egbert, G. D. and Erofeeva, S. Y. (2002). Efficient inverse modeling of barotropic ocean tides. *Journal of Atmospheric and Oceanic Technology*, 19(2):183–204.

Escobar Sierra, C. A. (2007). *Modelling of sediment dynamics in the Dithmarschen Bight, German North Sea Coast*. PhD thesis, Christian-Albrechts-Universität zu Kiel.

Etri, T. (2007). *Effects os storms on short and medium-term morphodynamics of a tide-dominated coastal region*. PhD thesis, Christian-Albrechts-Universität zu Kiel.

Fettweis, M. (2008). Uncertainty of excess density and settling velocity of mud flocs derived from in situ measurements. *Estuarine, Coastal and Shelf Science*, 78(2):426–436.

Fink, A. H., Brücher, T., Ermert, V., Krüger, A., and Pinto, J. G. (2009). The european storm kyrill in january 2007: synoptic evolution, meteorological impacts and some considerations with respect to climate change. *Natural Hazards and Earth System Science*, 9(2):405–423.

Fortunato, A. B., Bertin, X., and Oliveira, A. (2009). Space and time variability of uncertainty in morphodynamic simulations. *Coastal Engineering*, 56(8):886–894.

Frank, H., Liermann, D., Majewski, D., and Ritter, B. (2014). *Kurze Beschreibung des Globalmodells GME (20 km/L60) und seiner Datenbanken auf dem Datenserver des DWD*. Deutscher Wetterdienst.

Fredsøe, J. and Deigaard, R. (1992). *Mechanics of Coastal Sediment Transport*. Advanced series on ocean engineering. World Scientific.

Hallermeier, R. J. (1981). A profile zonation for seasonal sand beaches from wave climate. *Coastal Engineering*, 4:253–271.

Hamamori, A. (1962). A theoretical investigation on the fluctuations of bedload transport. Technical Report R4, Delft Hydraulics Laboratory.

Hayes, M. O. (1979). Barrier island morphology as a function of tidal and wave regime. In Leatherman, S. P., editor, *Barrier islands: from the Gulf of St. Lawrence to the Gulf of Mexico*, chapter 1. Academic Press.

Hjulström, F. (1935). Studies of the Morphological Activity of Rivers as Illustrated by the River Fyris. Bulletin of the Geological Society 25, University of Uppsala.

Holthuijsen, L. H. (2007). *Waves in Oceanic and Coastal Waters*. Cambridge University Press.

Holthuijsen, L. H., Booij, N., and Ris, R. C. (1993). A spectral wave model for the coastal zone. In *Second International Symposium on Ocean Wave Measurement and Analysis*, pages 630–641.

Kaja, G. (2011). http://www.kaja-images.de/.

Kamphuis, J. W. (2000). *Introduction to Coastal Engineering and Management*. Advanced series on ocean engineering. World Scientific.

Latteux, B. (1987). Transport modeling of particulate matter – methodology of long-term simulation of bed evolution. Scientific report HE-42/87.25, Laboratoire National d'Hydraulique.

Le Hir, P., Roberts, W., Cazaillet, O., Christie, M., Bassoullet, P., and Bacher, C. (2000). Characterization of intertidal flat hydrodynamics. *Continental Shelf Research*, 20(12):1433–1459.

Lesser, G. R. (2009). *An approach to medium-term coastal morphological modelling*. PhD thesis, Delft University of Technology.

Lesser, G. R., Roelvink, J. A., van Kester, J. A. T. M., and Stelling, G. S. (2004). Development and validation of a three-dimensional morphological model. *Coastal engineering*, 51(8):883–915.

Maurer, M., Kelamener, Y., and Bechteler, W. (1997). The effects of inaccurate input parameters on deposition of suspended sediment. *International Journal of Sediment Research*, 3(12):191–198.

Mayerle, R., Pramono, G., and Escobar Sierra, C. A. (2005). *Dimension and Roughness Distribution of Bed Forms in Tidal Channels in the German Bight*, volume 69, pages 229–251. Kuratorium für Forschung im Küsteningenieurwesen.

Mayerle, R., Runte, K., Etri, T., and Nguyen, D. (2010). Prognosen zur morphologischen Entwicklung im Bereich der Bohr- und Förderinsel Mittelplate sowie zur morphologischen Auswirkung der Bohr- und Förderinsel. Technical report, Forschungs- und Technologiezentrum Westküste der Universität Kiel.

Mayerle, R. and Zielke, W. (2005). *PROMORPH - PRedictions Of medium-scale MORPHodynamics: project overview and executive summary*, volume 69, pages 1–23. Kuratorium für Forschung im Küsteningenieurwesen.

NASA (2010). *Visible Earth: a catalog of NASA images and animations of our home planet*. National Aeronautics and Space Administration. http://visibleearth.nasa.gov/.

Neto, N. E. A. (2004). *Long- to Short-term Morphodynamic Evolution of the Tidal Channels and Flats of the Dithmarschen Bight, German North Sea*. PhD thesis, Christian-Albrechts-Universität zu Kiel.

Nguyen, D. (2015). *Medium-term morphodynamics of the Mittelplate area, German North Sea coast*. PhD thesis, Christian-Albrechts-Universität zu Kiel.

Nguyen, D., Etri, T., Runte, K. H., and Mayerle, R. (2010). Morphodynamic modeling of the medium-term migration of a tidal channel using process-based model. In *Proceedings of Coastal Engineering*, volume 32.

Palmer, T., Branković, v., Molteni, F., and Tibaldi, S. (1990). Extended-range predictions with ECMWF models: Interannual variability in operational model integrations. *Quarterly Journal of the Royal Meteorological Society*, 116(494):799–834.

Partheniades, E. (1965). Erosion and Deposition of Cohesive Soils. *Journal of the Hydraulics Division*, 91:105–139.

Pinto, L., Fortunato, A. B., and Freire, P. (2006). Sensitivity analysis of non-cohesive sediment transport formulae. *Continental Shelf Research*, 26(15):1826–1839.

Poerbandono (2003). *Sediment transport measurements and modelling in the Meldorf Bight tidal channels, German North Sea Coast*. PhD thesis, Christian-Albrechts-Universität zu Kiel.

POL (2008). POL Annual Report 2007-08. Technical report, Proudman Oceanographic Laboratory.

Pramono, G. H. (2005). *The study of bedforms and equivalent roughness sizes in the Central Dithmarschen Bight*. PhD thesis, Christian-Albrechts-Universität zu Kiel.

Reeve, D. and Fleming, C. (1997). A statistical-dynamical method for predicting long term coastal evolution. *Coastal Engineering*, 30(3):259–280.

Reynolds, O. (1887). On certain laws relating to the regime of rivers and estuaries and on the possibility of experiments on a small scale. Technical report, British Association for the Advancement of Science.

Reynolds, O. (1889). On model estuaries I: on the action of waves and currents. Technical report, British Association for the Advancement of Science.

Reynolds, O. (1890). On model estuaries II: on the action of waves and currents. Technical report, British Association for the Advancement of Science.

Reynolds, O. (1891). On model estuaries III: on the action of waves and currents. Technical report, British Association for the Advancement of Science.

Richardson, J. F. and Zaki, W. N. (1954). Sedimentation and fluidization: Part I. *Transactions of the Institution of Chemical Engineers*, 32:35–53.

Roelvink, J. A. (2006). Coastal morphodynamic evolution techniques. *Coastal Engineering*, 53:277–287.

Schmelter, M. L., Erwin, S. O., and Wilcock, P. R. (2012). Accounting for uncertainty in cumulative sediment transport using Bayesian statistics. *Geomorphology*, 175:1–13.

Schmelter, M. L., Hooten, M. B., and Stevens, D. K. (2011). Bayesian sediment transport model for unisize bed load. *Water Resources Research*, 47(11).

Schulz, J. P. and Schättler, U. (2014). *Kurze Beschreibung des Lokal-Modells Europa COSMO-EU (LME) und seiner Datenbanken auf dem Datenserver des DWD*. Deutscher Wetterdienst.

Scialabba, N. (1998). *Integrated coastal area management and agriculture, forestry and fisheries: FAO guidelines*. FAO Guidelines. Food and Agriculture Organization of the United Nations.

Shields, A. (1936). *Anwendung der Ähnlichkeitsmechanik und der Turbulenzforschung auf die Geschiebebewegung*. PhD thesis, Technische Hochschule Berlin.

Soulsby, R. L., Manning, A. J., Spearman, J., and Whitehouse, R. J. S. (2013). Settling velocity and mass settling flux of flocculated estuarine sediments. *Marine Geology*, 339:1–12.

Stephenson, D. B. and Doblas-Reyes, F. J. (2000). Statistical methods for interpreting Monte Carlo ensemble forecasts. *Tellus A*, 52(3).

Sutherland, J., Peet, A. H., and Soulsby, R. L. (2004). Evaluating the performance of morphological models. *Coastal engineering*, 51(8):917–939.

Thornton, H., Roberts, J., Stephenson, D., Dawkins, L., Youngman, B., Shaffrey, L., Champion, A., Hodges, K., and Stringer, M. (2016). *Extreme Wind Storms Catalogue*. Met Office, University of Reading and University of Exeter. http://www.europeanwindstorms.org/.

Toro, F., Mayerle, R., Poerbandono, and Wilkens, J. (2005). *Patterns of Hydrodynamics in a Tide-Dominated Coastal Area in the South-Eastern German Bight*, volume 69, pages 25–62. Kuratorium für Forschung im Küsteningenieurwesen.

TPXO (2016). *OSU Tidal Data Inversion*. Oregon State University. http://volkov.oce.orst.edu/tides/.

Turowski, J. M. (2010). Probability distributions of bed load transport rates: A new derivation and comparison with field data. *Water Resources Research*, 46(8).

UNESCO (1981). Background papers and supporting data on the International Equation of State of Seawater, 1980. Unesco technical papers in marine science 38, UNESCO.

van der Klis, H. (2003). *Uncertainty analysis applied to numerical models of river bed morphology*. PhD thesis, TU Delft, Delft University of Technology.

van der Wegen, M. (2010). *Modeling morphodynamic evolution in alluvial estuaries*. PhD thesis, Delft University of Technology.

van der Wegen, M., Dastgheib, A., Jaffe, B. E., and Roelvink, D. (2010). Bed composition generation for morphodynamic modeling: case study of San Pablo Bay in California, USA. *Ocean Dynamics*, 61:173–186.

van der Wegen, M. and Jaffe, B. E. (2013). Towards a probabilistic assessment of process-based, morphodynamic models. *Coastal Engineering*, 75:52–63.

van Rijn, L. C. (1990). *Principles of fluid flow and surface waves in rivers, estuaries, seas and oceans*. Aqua Publications.

van Rijn, L. C. (1993). *Principles of sediment transport in rivers, estuaries and coastal seas*. Aqua Publications.

van Rijn, L. C. (1998). *Principles of coastal morphology*. Aqua Publications.

van Rijn, L. C. (1998). The effect of sediment composition on cross-shore bed profiles. *Coastal Engineering Proceedings*, 1(26).

van Rijn, L. C. (2001). General view on sand transport by currents and waves: data analysis and engineering modelling for uniform and graded sand (TRANSPOR 2000 and CROSMOR 2000 models). Technical Report Z2899.20 / Z2099.30 / Z2824.30, WL | Delft Hydraulics.

van Rijn, L. C. (2003). Sand transport by currents and waves; general approximation formulae. In *Proceedings of Coastal Sediments*, volume 3.

van Rijn, L. C. (2007). Unified View of Sediment Transport by Currents and Waves I: Initiation of Motion, Bed Roughness, and Bed-Load Transport. *Journal of Hydraulic Engineering*, 133(6):649–667.

van Rijn, L. C., Roelvink, J. A., and Horst, W. T. (2000). Approximation formulae for sand transport by currents and waves and implementation in DELFT-MOR. Technical Report Z3054.40, WL | Delft Hydraulics.

van Rijn, L. C., Walstra, D. J. R., Grasmeijer, B., Sutherland, J., Pan, S., and Sierra, J. P. (2003). The predictability of cross-shore bed evolution of sandy beaches at the time scale of storms and seasons using process-based profile models. *Coastal Engineering*, 47(3):295–327.

van Vuren, B. G. (2005). *Stochastic modelling of river morphodynamics*. PhD thesis, TU Delft, Delft University of Technology.

Verboom, G. K., De Ronde, J. G., and van Dijk, R. P. (1992). A fine grid tidal flow and storm surge model of the North Sea. *Continental Shelf Research*, 12(2):213–233.

Wilkens, J. (2004). *Medium scale morphodynamics of the Central Dithmarschen Bight*. PhD thesis, Christian-Albrechts-Universität zu Kiel.

Wilks, D. S. (2006). *Statistical Methods in the Atmospheric Sciences*. International Geophysics. Elsevier Science.

Winterwerp, J. C., Manning, A. J., Martens, C., De Mulder, T., and Vanlede, J. (2006). A heuristic formula for turbulence-induced flocculation of cohesive sediment. *Estuarine, Coastal and Shelf Science*, 68(1):195–207.

Woodroffe, C. D. (2002). *Coasts: form, process and evolution*. Cambridge University Press.

Wren, D. G., Barkdoll, B. D., Kuhnle, R. A., and Derrow, R. W. (2000). Field techniques for suspended-sediment measurement. *Journal of Hydraulic Engineering*, 126(2):97–104.

Yen, B. C. (1986). *Stochastic and risk analysis in hydraulic engineering*. Distributed by Water Resources Publications.

Zanke, U. (1982). *Grundlagen der Sedimentbewegung*. Hochschultext. Springer Berlin Heidelberg.

Zielke, W. (1999). *Numerische Modelle von Flüssen, Seen und Küstengewässern*. DVWK-Schriften. Wirtschafts- und Verlag-Ges. Gas und Wasser.

Appendix A

Table A.1: Normally distributed parameters generated for the morphodynamic ensembles.

member	D_{50} [µm]	τ_{cr} [$\mathrm{N\,m^{-2}}$]	w_s [$\mathrm{mm\,s^{-1}}$]
1	212	0.271	0.911
2	147	0.304	0.564
3	228	0.270	0.345
4	235	0.350	0.710
5	200	0.327	1.660
6	218	0.302	1.030
7	182	0.299	0.872
8	265	0.283	0.857
9	249	0.334	0.417
10	219	0.389	0.425
11	235	0.262	0.466
12	168	0.288	0.655
13	193	0.322	0.613
14	214	0.279	1.240
15	158	0.319	0.779
16	165	0.234	0.795
17	189	0.310	0.369
18	165	0.261	1.010
19	210	0.261	1.140
20	212	0.295	0.436
21	193	0.319	0.394
22	179	0.286	0.687
23	215	0.311	0.721
24	158	0.318	0.943
25	191	0.279	0.704
26	178	0.286	0.559
27	237	0.299	0.518
28	204	0.290	1.060
29	211	0.294	0.442
30	157	0.331	0.835
$\overline{\mathbf{x}}$	200	0.299	0.739
$\mathbf{s}$	30	0.031	0.302

Declaration

I hereby declare that apart from the supervisor's guidance the content and design of the essay is all my own work. The thesis has been submitted neither partially nor wholly as part of a doctoral degree to another examining body, and it has neither been published nor submitted for publication. I also assure that the thesis has been prepared subject to the Rules of Good Scientific Practice of the German Research Foundation.

Kiel, 21st of July 2017

Guilherme Luiz Dalledonne